Micromechanical Actuators for Insect Flight Mechanics

by

Hui Zhou

B.S. Tsinghua University, 2002
M.S. Tsinghua University, 2004

Submitted to the Department of Materials Science and Engineering
in Partial Fulfillment of the Requirement for the Degree of
Master of Science in Materials Science and Engineering

at the

Massachusetts Institute of Technology

June 2008

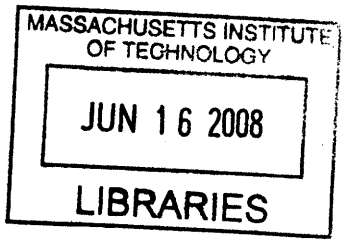

ARCHIVES

Signature of Author _____
Department of Materials Science and Engineering
May 23, 2008

Certified by _____
Martin A. Schmidt
Professor of Electrical Engineering and Computer Science
Thesis Supervisor

Certified by _____
Harry L. Tuller
Professor of Ceramics and Electronic Materials
Thesis Reader

Accepted by _____
Samuel M. Allen
POSCO Professor of Physical Metallurgy
Chair, Departmental Committee on Graduate Students

Micromechanical Actuators for Insect Flight Mechanics

by

Hui Zhou

Submitted to the Department of Materials Science and Engineering
on May 23, 2008 in Partial Fulfillment of the Requirement for the Degree of
Master of Science in Materials Science and Engineering

Abstract

This project aims to develop MEMS actuators to aid in the study of insect flight mechanics. Specifically, we are developing actuators that can stimulate the antennae of the crepuscular hawk moth Manduca Sexta. The possible mechanosensory function of antennae as airflow sensors has been suggested, and recent discoveries of our collaborators reveal that mechanosensory input from the antennae of flying moths serves a similar role to that of the hind wings of two-winged insects, detecting Coriolis forces and thereby mediating flight stability during maneuvers. Early evidence suggests that mechanical stimulus of the antennae may enable flight control. In addition, the crepuscular hawk moth Manduca Sexta has a wide wingspan (~110 mm) and is capable of carrying at least one quarter of its own weight. Thus, studying the flight of Manduca Sexta by attachment of microsystems seems plausible. The goal of our project is to design and fabricate micromechanical actuators, which will be mounted onto the moth antennae. Our collaborators will study the flight control mechanism by mechanical stimulation.

Our first step was to fabricate "dummy" silicon rings for our biologist collaborators for implant experiment. A series of mounting kits were developed, and due to the nature of the moth antennae, ring-beam-ring construction was finally designed and fabricated, like a "shackle", to meet the mounting requirements. Next, we integrated actuators onto the mounting kit. Piezoelectric film/sheet, piezoelectric-bender and piezoelectric-stack were considered as the actuators. Live testing was also taken while the moth was resting or flapping its wings. The moth apparently responds to the mechanical stimulus under both circumstances, by swinging its wings and abdomen. Actuation amplifier was also modeled and tested, which might be used for future mechanical stimulators.

Thesis Supervisor: Martin A. Schmidt
Title: Professor of Electrical Engineering and Computer Science

Thesis Reader: Harry L. Tuller
Title: Professor of Ceramics and Electronic Materials

Acknowledgements

There are many people I would like to thank for their help and support during my thesis preparation. First of all, I would like to express my deepest gratitude and respect to my advisor, Professor Martin A. Schmidt. Marty is so considerate, without him, I would not be able to conduct research and continue my study in the field of MEMS. Marty is so knowledgeable, and I have learnt a lot from his insight and critical thinking. I feel very lucky to be his student.

Help from our collaborators is very important for me to accomplish the thesis. In particular, Professor Joel Voldman, leading the entire cyborg moth project; Professor Thomas Daniel at University of Washington, hosting our brainstorming visiting and providing the moths and facilities for my experiments; Armin Hinterwirth, Dr. Zane Aldworth, and Dr. Ty Hedrick of Tom's group, helping me to do the live testing.

Professor Harry L. Tuller is very kind to be my thesis reader. I was his TA and took his class before, and benefit a lot from his explicit guidance and distinct teaching.

Deflection testing was done with the laser vibrometer in Professor Brian Wardle's laboratory. Miso Kim helped me with the testing.

Schmidt group members – Dr. Hanqing Li, Dr. Valerie Leblanc, Dr. Jianglong Chen, Kerry Cheung, Vikas Sharma, and Eric Lam – gave me much help and support.

The staff, faculty, and students of the Microsystems Technology Laboratories were very helpful, especially Donal Jamieson, Dave Terry, Bernard Alamariu, Kurt Broderick, and Dennis Ward.

Last but not least, I would like to thank my family and friends who have supported me. My parents and sister have been a tremendous source of encouragement through my life. Finally, I would like to thank my wife Haiying for her infinite love, untiring support and encouragement. Her happiness is the very motivation behind my hard working.

Table of Contents

List of Figures

List of Tables

Chapter 1 Introduction

Controllable flying machines have many important applications, such as seeking out targets and collecting intelligence in an unobtrusive manner without exposing personnel to danger. The current approaches to achieve this capability include man-made flying vehicles and trained biological flying animals.

Man-made flying vehicles can be well controlled and have large payload capacity, which make it a choice of controllable flying machines, however, severe power constraints drastically limit their flight time. Flying insects are arguably the most efficient flying machines which can fly days to weeks, but they are difficult to train.

With the development in insect neurobiology and the evolution of Microelectro-mechanical Systems (MEMS), a third approach is now possible for achieving this mission capability. MEMS, which are small, light, low-power, and have a diverse set of electrical, mechanical, chemical, optical, etc. capabilities, are the ideal man-made system for instrumenting an insect. Such a hybrid insect-MEMS system (HIMS) would combine the best qualities of the biology (energy storage) and MEMS (precise control) and lead to a very promising controllable flying machine. Among the flying insects, we focus on the tobacco hornworm moth Manduca sexta because its sensory and motor control systems have been well investigated and it has a relatively large payload capacity.

The overall control mechanism of HIMS is to input a sensory signal to a control algorithm to elicit a control output signal that will then affect insect flight. Our approach is to stimulate the external sensory organs of the moth (the antennae) and study its corresponding response in order to find ways to "drive" the moth following our order. The signal input MEMS device is thus named the Mechanical Gyroscope Stimulator (MGS).

To actuate the antennae, we first designed and fabricated the mounting kits as

the bases of the MGS to be attached onto the moth head (Chapter 3). A series of designs were made and fabricated, from the simple rings, 2-D & 3-D structures, to the final version which is named "antennal shackle". Piezoelectric actuators were then integrated into the shackle (Chapter 4). Finite element modeling was presented and live testing was performed (Chapter 6). Displacement amplification methods are also discussed in Chapter 5.

Chapter 2 Background

2.1 Biological Background

Among all the flying insects, we focus on the tobacco hornworm moth Manduca sexta because its sensory and motor control systems are reasonably well understood and it has a relative large payload capacity. Manduca sexta is a crepuscular hawk moth which flies under poorly lit conditions. Weighing approximately 2.6g with a wingspan of approximately 110mm, it ranks among the largest and fastest of flying insects, capable of moving at speeds in excess of 5m/s with wing beat frequencies of about 25Hz. They have been recorded carrying payloads of up to 0.7grams.

The possible mechanosensory function of antennae as airflow sensors has been suggested [1]. It is recently discovered that the moth's antennae experience strong Coriolis forces during aerial maneuvers, and mechanosensors at the bases of the antennae are necessary for its flight [2]. Mechanically stimulating one or both antennae provides an approach that is possible to bias the moth flight and ultimately achieve a controllable flying vehicle based on this theory.

Figure 2-1 Life cycle of the crepuscular hawk moth, Manduca sexta (courtesy of John G. Hildebrand, University of Arizona).

The life cycle of Manduca sexta lasts about 30~50 days (Figure 2-1). In most areas, wild Manduca sexta have about two generations per year and three or four generations per year in Florida. However, our collaborators at the University of Washington and at University of Arizona routinely culture the moths in laboratory conditions, providing year-round access to all life stages of the animal. The adult life span is at least one week, which make them ideal candidate for insect flight mechanism study and for our stimulation testing.

2.2 Micro-actuators

An actuator is a device that converts energy from one form to mechanical form. The most common actuation methods include electrostatic, thermal, piezoelectric, and magnetic actuations [3-5].

(1) Electrostatic Actuation

The electrical actuation relies on the coulombic attraction/repulsion between charged bodies. The electrostatic-drive micromotor was one of the earliest MEMS actuators [6]. The motor (Figure 2-2) consists of a rotor that is attached to the

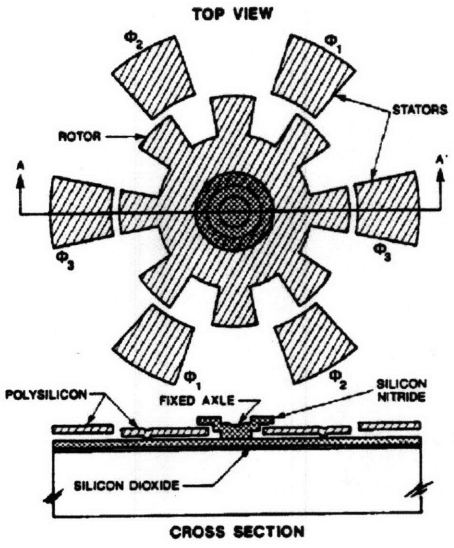

Figure 2-2 An electrostatic micromotor [6].

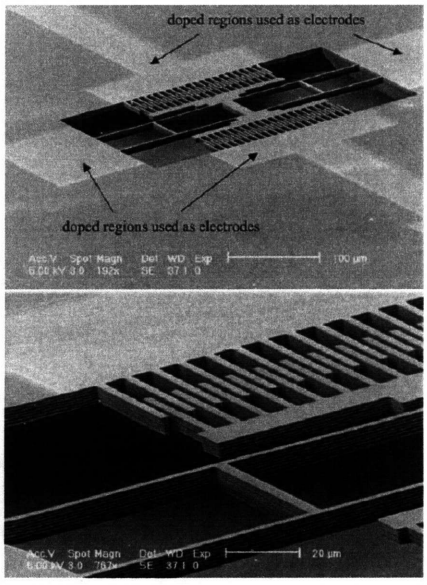

Figure 2-3 A comb-drive electrostatic actuator [12].

substrate with a hub, and a set of fixed stators, on the periphery. When the stator electrodes are biased, an electrostatic attractive force will align the rotor tooth with the biased stator, and multi-phase bias signals lead to continuous rotation. Other rotary actuators include wobble micromotors [7, 8] and static-induction micromotors [9, 10].

Another type of electrostatic actuators are linear micromotors. Parallel plates of the capacitor(s) are allowed to move laterally and parallel to each other. By applying voltage pulses, the rotor move forward and backward. A typical linear electrostatic micromotor is called comb-drive device, which uses interdigitated finger capacitors as shown in Figure 2-3 [11, 12].

(2) Thermal Actuation

Actuation can also be achieved by applying or removing heat. Heat is generated by different means including using electromagnetic waves (e.g. light), ohmic heating, or convection heating. The resistive heating is the most popular method used in thermal actuators. Cooling can be obtained by dissipation and active thermoelectric cooling.

The thermal bimetallic effect is a very commonly used method for thermal actuation. The thermal bimorph consists of two materials joined together as a single element. Due to the difference of thermal expansion coefficients of the two materials, the bimorph deforms [13]. Compared to electrostatic actuation, thermal bimorph actuation can achieve relative large movement but need much more power to operate, and its response speed is quite slow. Thermal actuation can also be achieved with a single material with bent-beam structures (Figure 2-4) [14-16].

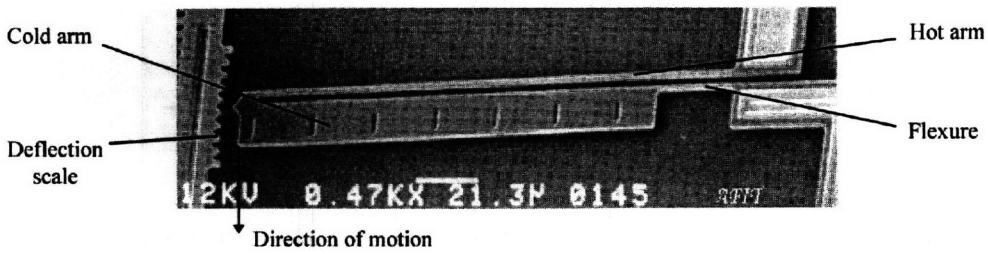

Figure 2-4 A lateral thermal actuator [16].

An application of thermal actuation is the inkjet printhead (Figure 2-5). It consists of a micromachined fluid chamber with an opening. A voltage pulse produces a vapor bubble to squeeze the liquid ink and eject an ink droplet [17, 18].

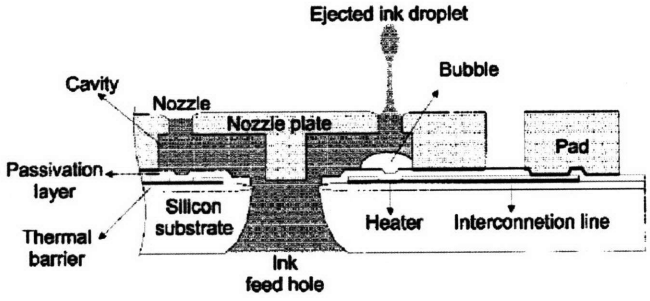

Figure 2-5 Schematic cross-section view of the inkjet printhead [18].

(3) Magnetic Actuation

Magnetic actuation is one of the most widely used actuation methods in our everyday appliances. The underlying principles and device geometry of the magnetic macro-actuators and those of the magnetic micro-actuators are the same. Magnetic micro-actuators also involve permanent magnets and electromagnetic coils, and can be categorized according to the magnetic sources types: a permanent magnet, an integrated electromagnetic coil, or an external solenoid. The deposition of magnetic materials and their patterning and subsequent processing should be compatible with the integrated circuit fabrication processes. A typical fabrication method of a three dimensional microcoil is illustrated in Figure 2-6, and some microcoils are shown in Figure 2-7 and Figure 2-8.

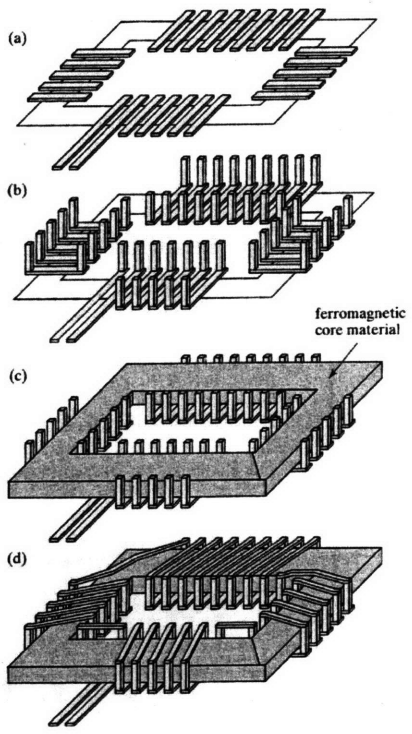

Figure 2-6 Fabrication of a microcoil [3].

Examples of magnetic micro-actuators include magnetic motor [21], flap magnetic actuator [22], electromagnetic optical scanning mirror [23, 24], and bistable electrical switch [25].

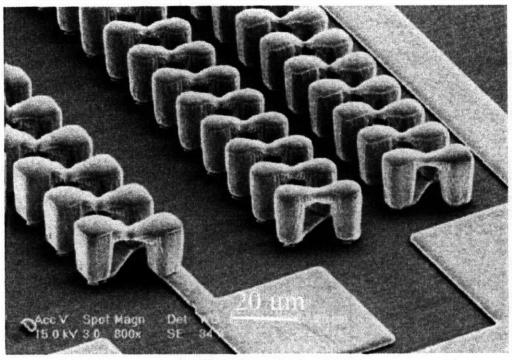

Figure 2-7 Microcoils [19].

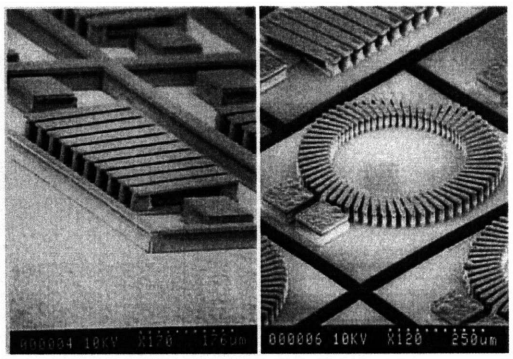

Figure 2-8 Helical and toroid coils [20].

(4) Piezoelectric Actuation

Piezoelectric materials couple mechanical deformation and electrical polarization. They experience mechanical deformation upon application of an electric field, and become electrically polarized under mechanical loads. Piezoelectric materials include single crystals (quartz, lithium niobate), ceramics (lead zirconate titanate, barium titanate), and polymers (polyvinylidene fluoride). Among all the piezoelectric materials, the lead zirconate titanate – $Pb(Zr_x,Ti_{1-x})O_3$ or PZT – ceramics attract much attention due to their very high piezoelectric coupling coefficients and high frequency applications. Polymers and ceramics can easily be deposited over silicon and patterned. Deposition methods include vacuum evaporation, reactive sputtering, metal-organic chemical vapor deposition, rf-magnetron sputtering, sol-gel deposition, and laser ablation techniques.

Piezoelectric actuators are already commonly available in the market, such as a stack translator from Physik Instrumente (PI) GmbH & Co. KG and bimorph actuators from Piezo System, Inc. Other piezoelectric actuators include inchworm linear micromotors [26, 27] and rotational micromotors [28, 29]. Inchworms are developed to achieve ultraprecision positioning which is essential for optical

alignment, miniature robots, microbiological cell manipulation, and precision machining. An inchworm motor is shown in Figure 2-9. The inchworm has two piezoelectric actuators for clamping and a third actuator for creating longitudinal extension, the motor's displacement. Each of the inchworm's actuators can be operated independently. The inchworm produces step motion, which originates from the clamp and release of the two clamping actuators [26].

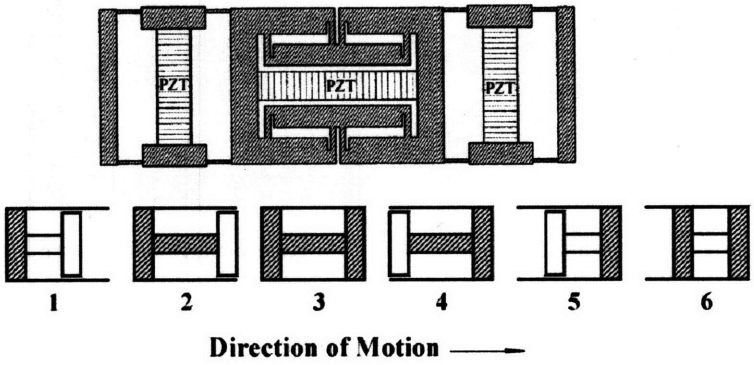

Figure 2-9 Inchworm motor and motor actuation sequence [26].

By transforming the vibration of the stator transducer to rotation motion through the frictional force, an ultrasonic rotational piezoelectric micromotor was made [29]. The polarization of PZT was normal to the surface. The fundamental bending vibration of the stator transducer was generated and transformed to rotational motion as shown in Figure 2-10.

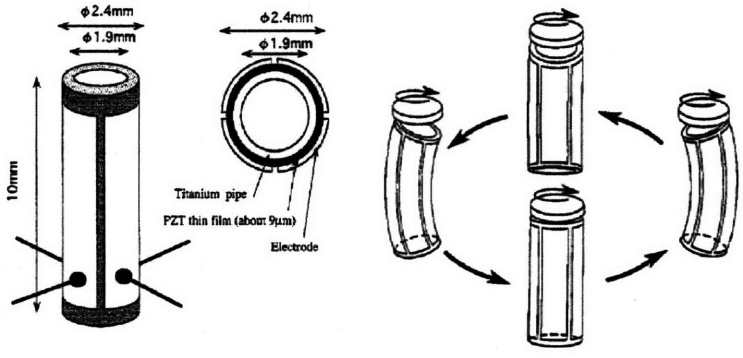

Figure 2-10 An ultrasonic micromotor [29].

Chapter 3 Antennal Mounting Kits

3.1 Motivation

It was recently discovered that the moths' antennae have mechanosensors at their bases, which are necessary for their flight. Mechanically stimulating one or both antennae might bias the moth flight. The goal of this work is to enable study of the relationship between the antennal vibration and the moth's flight behavior. Ultimately, we hope to control the moth's flight via stimulating its antennae.

To study the flight mechanism of the moth while it's flying freely, one can mount an actuator onto the moth body and locally stimulate the antennae. Manduca sexta moth is among the largest and strongest insects in the world, and it turns out to be a good candidate for this study. Its relative "big" head (Figure 3-1) provides us a large platform for mounting the device. In this chapter, we describe the evolution of the mounting kits as the bases for the actuators, or "stimulators". All the mounting kits in this chapter were made of silicon with IC compatible facilities. Once the appropriate mounting kit was decided, the actuating components were integrated into it, as discussed in the following chapters.

Figure 3-1 The head of Manduca sexta moth (courtesy of Armin Hinterwirth, University of Washington, Seattle).

The thickest part of the antenna of Manduca sexta moth is around 1mm in diameter for the male and around 0.5mm for the female. All the devices shown below were designed for male moths.

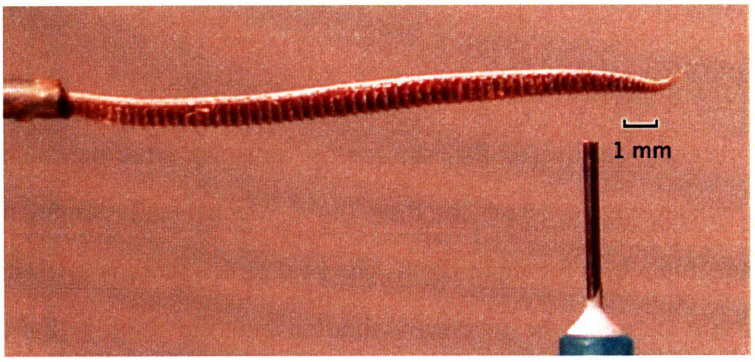

Figure 3-2 An antenna from a male moth (courtesy of Cam Myhrvold, University of Washington, Seattle).

3.2 Antennal Rings

The structures of the antennal rings are simple but expandable, which makes them the first design of the mounting kits. The ring thickness is that of the silicon wafer, which is approximately 0.68 mm (Figure 3-3).

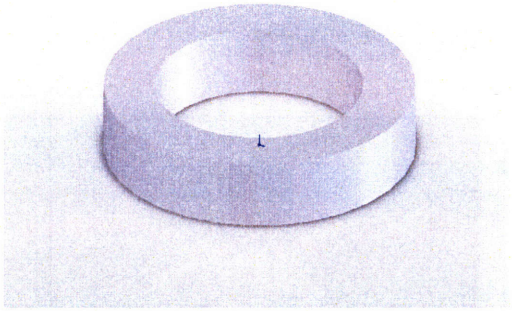

Figure 3-3 Ring structure.

Along with the simple ring design, there are two other designs shown in Figure 3-4. One can mount the actuating components onto the fingers or directly build the actuators as the fingers (Figure 3-5). By alternatively actuating different parts, we can tune the antennal vibration, with the moth's reaction helping us to learn its antennal function during flight.

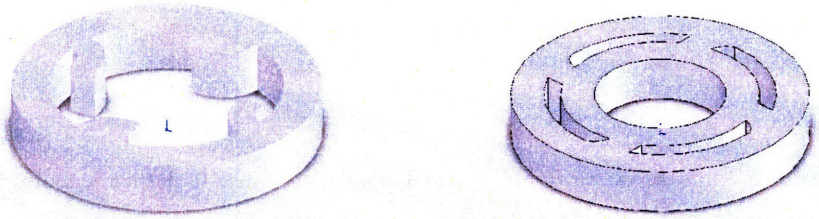

Figure 3-4 Two more ring structures.

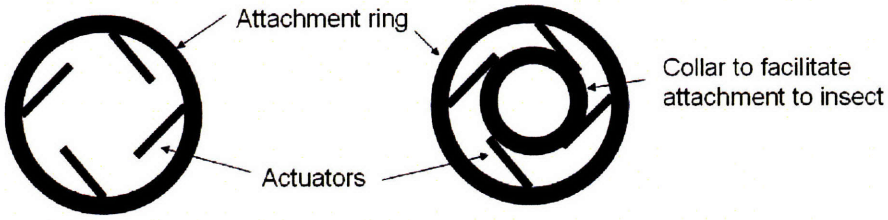

Figure 3-5 Concept of the ring actuators (courtesy of Martin Schmidt).

The rings were manually mounted onto the moth antennae when the moth was in hibernation. The mounting process was quite smooth with the aid of tweezers under a stereo optical microscope. But when the moth came back to life from hibernation, it resisted the rings very much and quickly threw them off by simply swinging its head and antennae. The rings turned out not to be stable because of the fact that the cross-section diameters of the moth antenna are not increasing gradually from the tip to the base, instead, the antenna is thickest in the middle and the base is much thinner than the middle part. The hole of the ring must match the thickest part in order to mount it, which make the moth capable of removing the rings. In addition, the variation between moths makes the rings unsuitable for every moth. This required the development of assembly structures to meet the mounting purpose.

3.3 Assembly Structures

Inspired by zip-like structures, we designed and fabricated a two-dimensional assembly as shown in Figure 3-6. By adopting the assembly structures, the problems of the simple rings in section 3.2 could be solved. Such a device can be directly attached to the base of the antenna without passing through the thickest middle

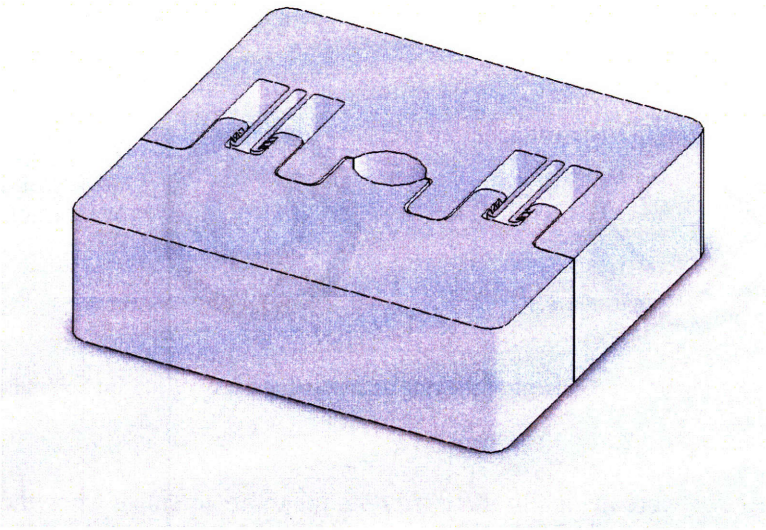

Figure 3-6 Two-dimensional assembly structures.

region; the three-step zip-like design makes it feasible to adjust the size of the central hole to fit each new moth. The geometries of the two-dimensional assembly structures are also easy to modify. Figure 3-7 shows the separate parts. The male assembly parts have different beam length. Devices with longer beam length are designed to be more flexible, while those with shorter beam stiffer.

Two-dimensional assembly structures solve the problems existing in the simple rings, however, they also bring their own inherent concerns. The two-dimensional structures are difficult to assemble on the moth antenna since there is no flat surface on the moth head to facilitate the process. Even assembled on a flat surface by tweezers with the aid of stereo optical microscope, the two-dimensional structures were only stable in plane, and out-of-plane mismatch could not be avoided when the assembly was lifted off the bench surface. Subsequently, a three-dimensional

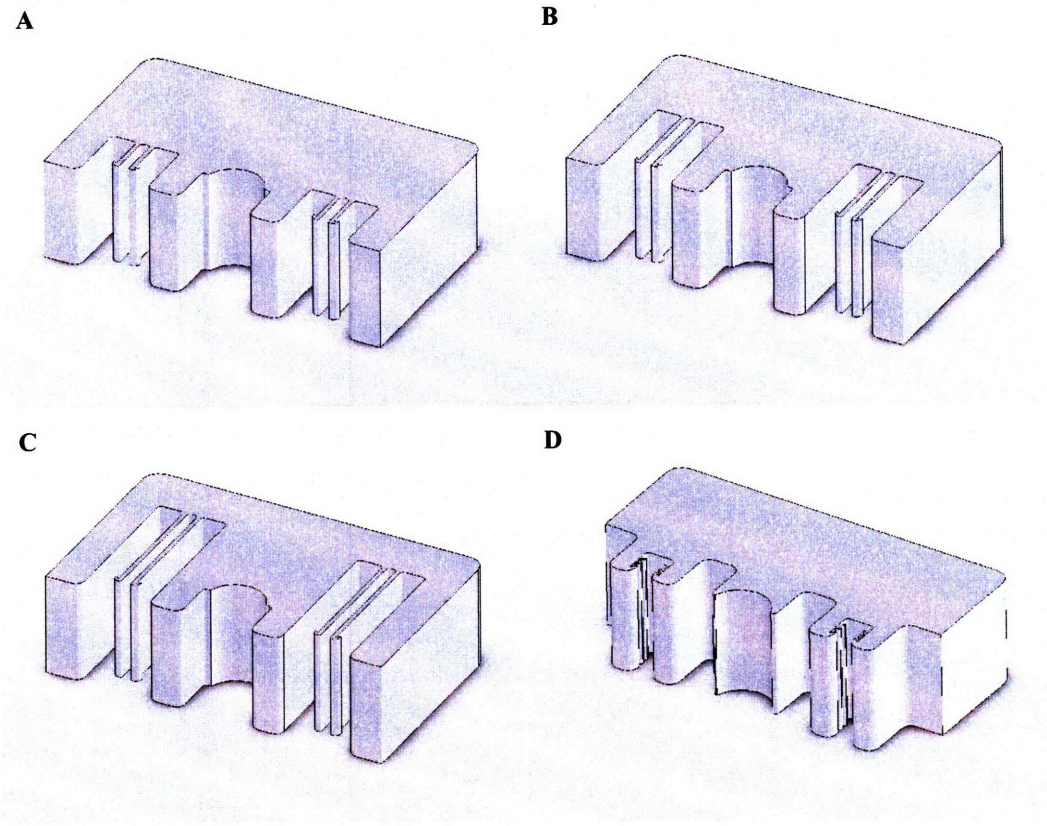

Figure 3-7 Two-dimensional assembly structures (A~C: male connectors with 300μm, 600μm, and 900μm long beams, respectively; D: female connector.)

assembly was designed to conquer the out-of-plane problem in the zip-like devices, as shown in Figure 3-8.

The three-dimensional assembly includes four parts, the base, three clamps, two protective rings, and the actuation ring. The base is attached to the moth head and possibly fixed with epoxy or wax, the three clamps hold the three ring-like structures, the top and bottom one of the three rings are identical and protect the middle ring, while the middle ring integrates the actuators. All parts are made of 0.68 mm thick silicon wafer, and assembled manually.

Figure 3-9 demonstrates the parts structures. The clamp (A) has six feet which insert into the holes in the base (C), and features two spacers to separate the three rings. The top and bottom fingers clamp the protective rings by fixing the tips into the slots in the protective rings (D). The middle ring shown in (B) has 16 springs

giving passive feedback to the antennal vibration.

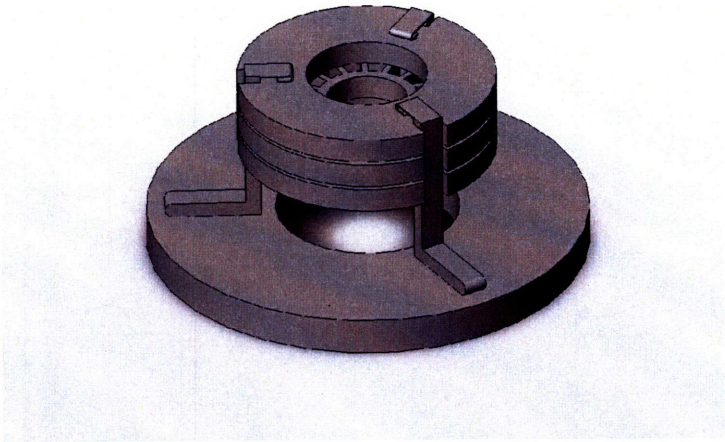

Figure 3-8 Schematic view of a three-dimensional assembly.

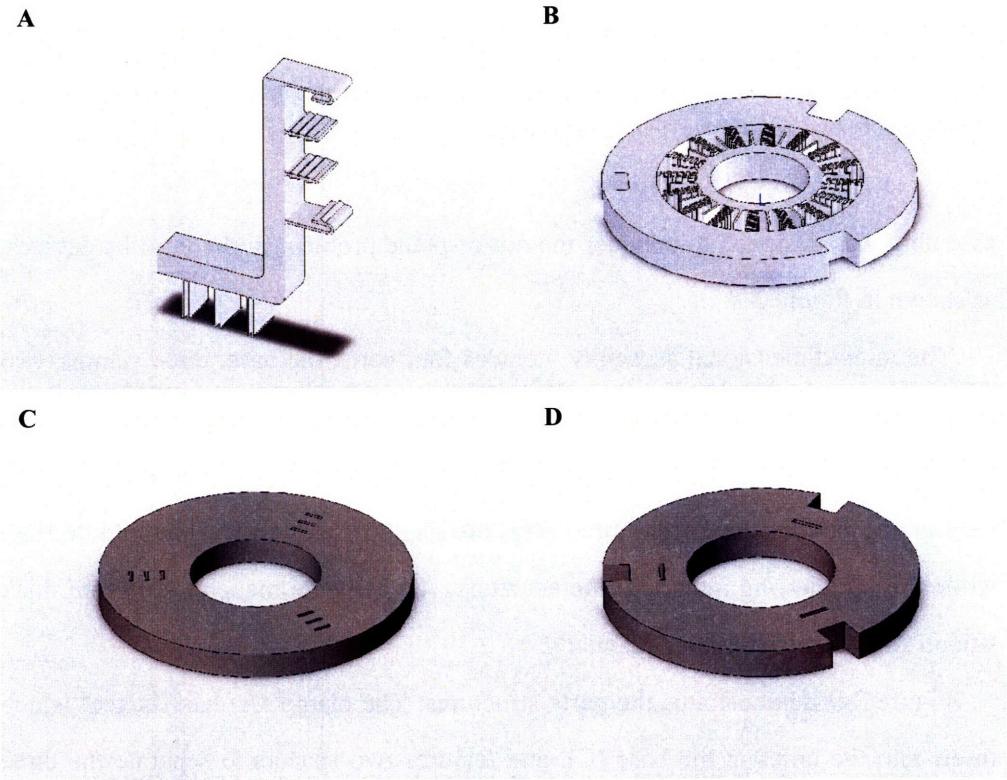

Figure 3-9 Schematic view of the three-dimensional assembly parts (A: clamp, B: middle ring, C: base, D: protective ring.)

The three-dimensional assembly provides a platform for the Mechanical Gyroscopic Stimulator. The middle ring can also integrate a variety of actuating components that actively stimulate the antennae motions. And the clamp can be modified into needle-shape-foot, which enables one to affix the device by penetrating the needle ends into the moth head directly (Figure 3-10).

Another three-dimensional assembly structure related to this project was also designed and fabricated, which will be discussed in Appendix B (Heat Sink).

3.4 Antennal Shackle

Three-dimensional assembly structures provide a platform for the micro-mechanical actuators for moth flight mechanics study. However, it is very challenging to assemble such devices. After carefully observation of the moth behavior, we found its antennal motion to be very limited. Though the moth can throw the simple rings off quite easily, by connecting two rings, the moth might not be able to remove the "shackle" like structure. Based on this hypothesis, we fabricated antennal shackles with different hole-sizes and beam lengths.

Shackles were manually fixed onto the moth with the two antennae in the holes (Figure 3-11), and our hypothesis was proven. Antennal shackles turned out to be very stable, and the moth with the shackle on its head could fly freely without any trouble. We further modified the design by adapting to the natural angel of 154°

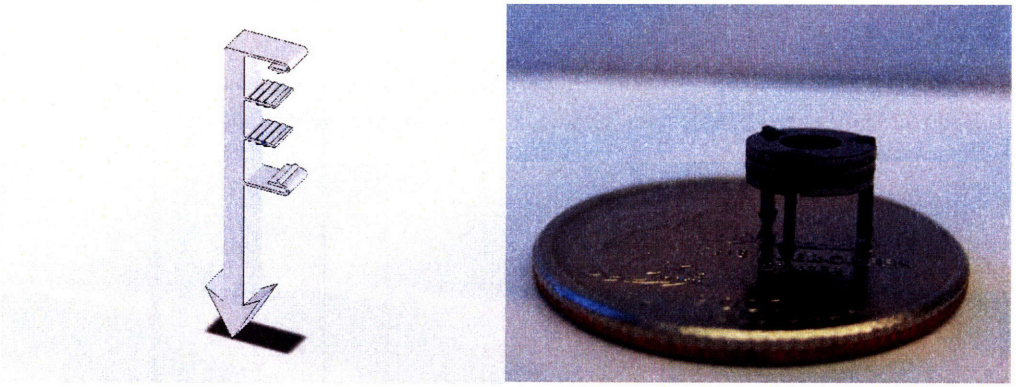

Figure 3-10 A modified three-dimensional device (left: schematic view of a modified clamp, right: an assembled device on a quarter).

between two antennae, as shown in Figure 3-12.

Compared to the three-dimensional assembly structure, the shackle is much simpler and easier to handle, and more able to integrate actuating elements due to its larger surface area. The shackle is the fundamental structure used to develop the stimulator discussed later in the next chapter.

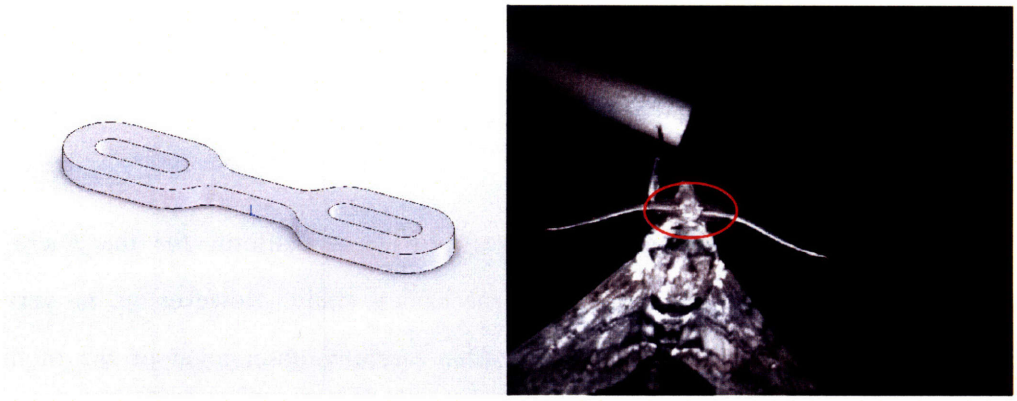

Figure 3-11 The "Shackle" (A: schematic view, B: live moth with the shackle).

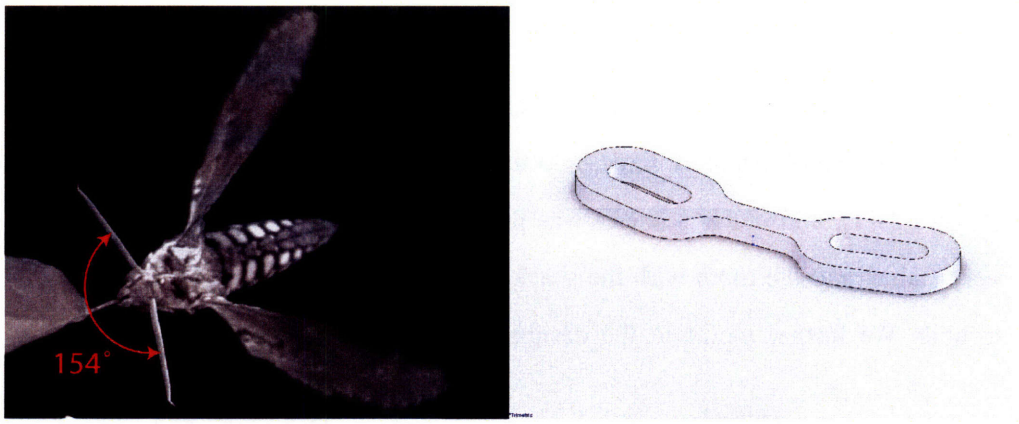

Figure 3-12 The modified "Shackle" (A: the angle between the moth antennae, courtesy of Ty Hedrick, University of Washington, Seattle; B: schematic view of the modified shackle).

Chapter 4 Piezoelectric Actuation

4.1 Motivation and Approaches

The hawk moth Manduca sexta vibrates antennae at a frequency of around 25Hz equal to its wing beat during flying. To stimulate the moth antennae effectively, the actuator should have a fast response speed and an adequate force output, require as little energy as possible to extend flying time between recharging, and be compatible with the moth motion.

Among the four most common actuation methods, piezoelectric actuation turns out to be the best candidate. Electrostatic actuation has a fast response, but it is susceptible to pull-in limitation and there is trade-off between magnitude of force and displacement. Thermal actuation is capable of achieving large displacement, but the relatively large power consumption limits its use in our stimulator. Magnetic actuation is capable of generating large displacement as well, however, the fabrication processes are quite complex. Piezoelectric actuation is capable of fast response and achieving moderately large displacement. In addition, miniature piezoelectric actuating elements are commercially available.

We took three kinds of piezoelectric actuation elements into consideration in terms of the physical shape, thin film/sheet, bender, and stack. Piezoelectric thin film deposition methods were briefly described in Section 2.2(4), among which sol-gel deposition is an attractive mean because it does not require complex equipment and can generate relatively thick films (up to 1μm) [30]. Piezoelectric sheets up to 2mm thick, bending actuators and miniature piezo-stacks are commercially available from vendors such as Piezo Systems, Inc. and Physik Instrumente (PI) GmbH & Co. KG. All these actuation approaches have been analyzed for our MGS application, and the details are discussed in the reminder of this chapter.

4.2 Piezoelectric Bi-morph Actuation

The silicon "shackle" is chosen as the base for our Mechanical Gyroscope Stimulator (refer to Section 3.4). Bi-morph actuation is achieved by piezoelectric thin films deposited on the silicon substrate or piezoelectric sheets (e.g. PZT sheets from Piezo Systems, Inc.) attached to the silicon shackle (Figure 4-1). When an electrical field is applied, the piezoelectric layer deforms and deflects the silicon shackle as shown in Figure 4-2.

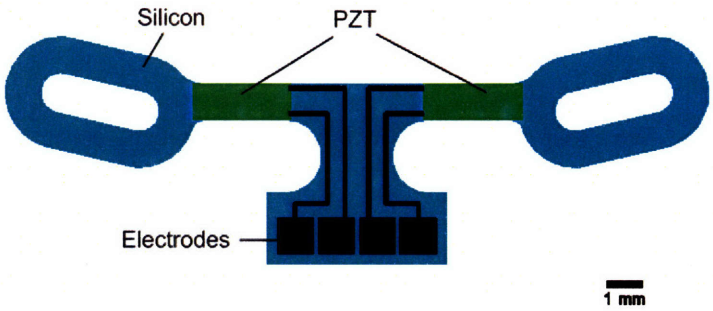

Figure 4-1 Schematic top-view of piezoelectric bi-morph structure.

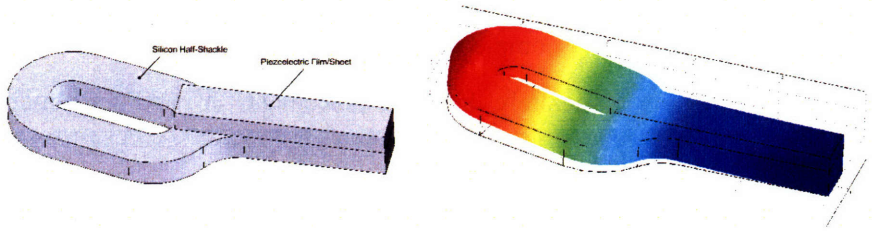

Figure 4-2 Piezoelectric bi-morph made of piezo-layer on silicon half-shackle, before deformation (left) and after deformation (right).

To analyze the deflection magnitude, the structure is simplified to a two-dimensional case shown in Figure 4-3. P_1 and P_2 are the interactive forces generated between the piezoelectric layer and the silicon substrate. M_1 and M_2 are the binding moments caused by P_1 and P_2. l_1 and l_2, a_1 and a_2 are the lengths and thicknesses of the piezo-layer and the extended silicon ring. Δ_1 and Δ_2 are the vertical displacements corresponding to l_1 and l_2, respectively, and ρ is the deflection radius.

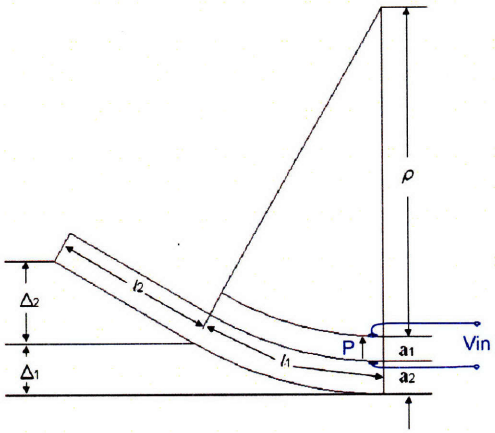

Figure 4-3 The simplified two-dimensional model. Left: the deformed bi-morph; above: the interactive region cut off from the deformed bi-morph.

Because there are no external forces, we have $P_1 = P_2 = P$ (1)

Moment balance leads to $M_1 + M_2 - P\left(\frac{a_1 + a_2}{2}\right) = 0$ (2)

ρ is the curvature radius: $\frac{1}{\rho} = \frac{M_1}{Y_1^E I_1} = \frac{M_2}{Y_2^E I_2}$ (3)

where I_1 and I_2 are moments of inertia, Y_1^E and Y_2^E are the Young's modulus for the piezo-layer and silicon, respectively.

Substituting Eq. (3) into Eq. (2), we have

$$P = \frac{2}{a_1 + a_2} \cdot \frac{Y_1^E I_1 + Y_2^E I_2}{\rho} \quad (4)$$

where $$I_1 = \frac{ba_1^3}{12}, I_2 = \frac{ba_2^3}{12} \quad (5)$$

and b is the common width of both parts.

At the interface, strains in the top and bottom layers are equal (for more about mechanical analysis, please refer to [31]):

$$d_{31}E + \frac{P}{a_1 b Y_1^E} + \frac{a_1}{2\rho} = -\frac{P}{a_2 b Y_2^E} - \frac{a_2}{2\rho} \quad (6)$$

where E is the applied electric field $E = V_{in}/a_1$. PZT is the most common piezoelectric material, and is also used in the following analysis. The initial depolarization field of PZT film/sheet is around 5×10^5 volt/meter. To be

conservative, we assume the applied electric field to be 3×10^5 volt/meter.

Combine Eqs. (4)-(6), we have the deflection curvature κ

$$\kappa = \frac{1}{\rho} = \frac{-d_{31}E}{\frac{(Y_1^E a_1^3 + Y_2^E a_2^3)}{6\cdot(a_1+a_2)}\cdot\left(\frac{1}{a_1 Y_1^E}+\frac{1}{a_2 Y_2^E}\right)+\frac{a_1+a_2}{2}} \tag{7}$$

The vertical deflections of the interactive part and extended ring part are:

$$\Delta_1 = \rho\cdot(1-\cos\theta) = 2\rho\sin^2(\theta/2) \approx 2\rho\cdot(\theta/2)^2 \approx 2\rho\cdot(l_1/2\rho)^2 = l_1^2/2\rho$$

$$\Delta_2 = l_2\sin\theta \approx l_2\cdot\theta \approx l_2\cdot(l_1/\rho)$$

Summarizing the two deflection magnitudes, the total endpoint deflection is

$$\Delta = \Delta_1 + \Delta_2 = \frac{1}{\rho}\cdot\left(l_1 l_2 + \frac{1}{2}l_1^2\right) = \kappa\cdot\left(l_1 l_2 + \frac{1}{2}l_1^2\right) \tag{8}$$

Let $Y_1^E = 50GPa$, $Y_2^E = 170GPa$, $d_{31} = -274\times10^{-12}\,m/v$, $a_2 = 0.66mm$, $l_1 = l_2 = 4mm$. The relationship of the endpoint deflection versus the thickness of the PZT film/sheet is plotted in Figure 4-4:

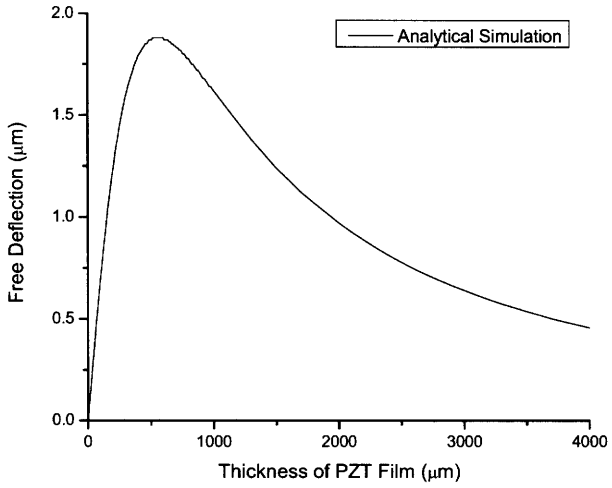

Figure 4-4 Endpoint deflection vs. PZT film thickness (analytical simulation).

Finite element analysis (FEA) modeling was also done to simulate the piezo-electric bi-morph deflection. The structure for FEA modeling is shown in Figure 4-2

(left). The right ends of the PZT sheet and the silicon half-shackle are set to be mechanically fixed, the applied electric field and the materials parameters are the same as the settings in the above analytical simulation. The thickness of the PZT film/sheet varies from 5μm to 2mm. The simulation results are like the one in Figure 4-2 (right), and more details can be found in Appendix A (Fundamentals of Piezoelectricity Analysis) and C1 (Modeling of Piezoelectric Bi-morph). The plot of the endpoint deflection versus the thickness of the PZT film/sheet is shown in Figure 4-5 along with the analytical simulation curve:

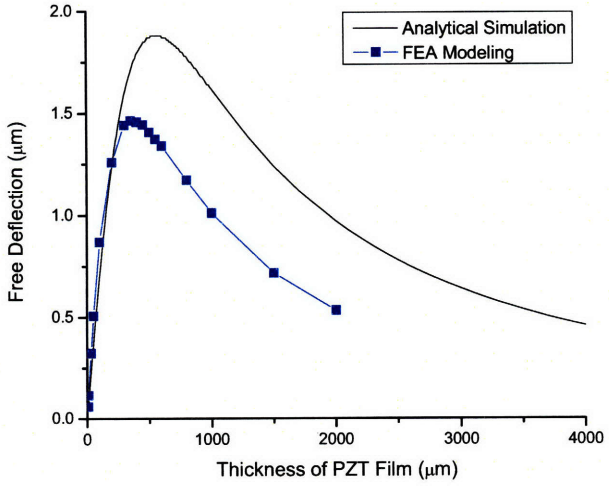

Figure 4-5 Endpoint deflection vs. PZT film thickness (FEA simulation).

The analytical and FEA simulations achieve quite consistent results with little difference, which might be caused by the simplification procedure during analytical modeling. Both curves show a deflection peak within the thickness range of the PZT layer. In analytical simulation, the ~1.8μm deflection peak appears with a 560μm thick PZT sheet. In FEA modeling, the maximum deflection is ~1.5μm at the PZT thickness of 350μm. In either modeling, the deflection magnitude is below 0.01μm if the PZT film is less than 1μm thick. As a result, the PZT thin film is excluded from MGS application since the deflection is apparently too small for moth antennae stimulation. One workable PZT-Si bi-morph actuation approach is to attach a 0.15mm~1mm thick PZT sheet onto the silicon shackle, which is able to deflect at the magnitude of over 1μm.

One way to achieve the bi-morph is to bind PZT and silicon with epoxy since silicon is not solderable, and solder wires to the top and bottom PZT electrodes. It is also feasible to deposit a buffer layer, such as a Ti/Au thin film, on the silicon substrate and have the PZT sheet soldered onto the surface. Wires are then soldered to the PZT top electrode and to the Ti/Au thin film deposited on the silicon substrate.

4.3 Piezoelectric Bending Actuation

Piezoelectric bending actuators can be built by laminating two piezoelectric layers to a center shim. The two-layer element produces curvature when one layer expands while the other layer contracts as shown in Figure 4-6. These transducers are often referred to as piezoelectric benders.

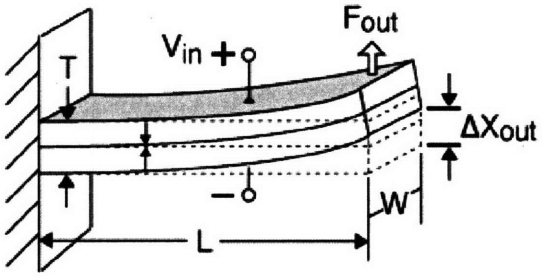

Figure 4-6 Two-layer piezoelectric bender.

Relative large bending force and the variety of mounting and motion options make benders a popular choice of design engineers. Our second approach to build MGS devices is to integrate the benders into the shackle structure. To achieve better actuation, the shackle is redesigned with three separate parts and connected by the benders. Two ends of a bender are glued onto silicon, and the middle region suspended in air. Six designs are shown in Figure 4-7. PZT benders were obtained from Piezo Systems, Inc., which were cut into 5mm by 2mm pieces. The deflection magnitude is proportional to length^2, and the 5mm-long bender is labeled to deflect by 5μm. As shown in the FEA modeling result, the shackle's endpoint deflection is up to 12.5μm when actuated by the PZT bender (Figure 4-8). The right end of the bender is mechanically fixed, and the applied voltage is 160V.

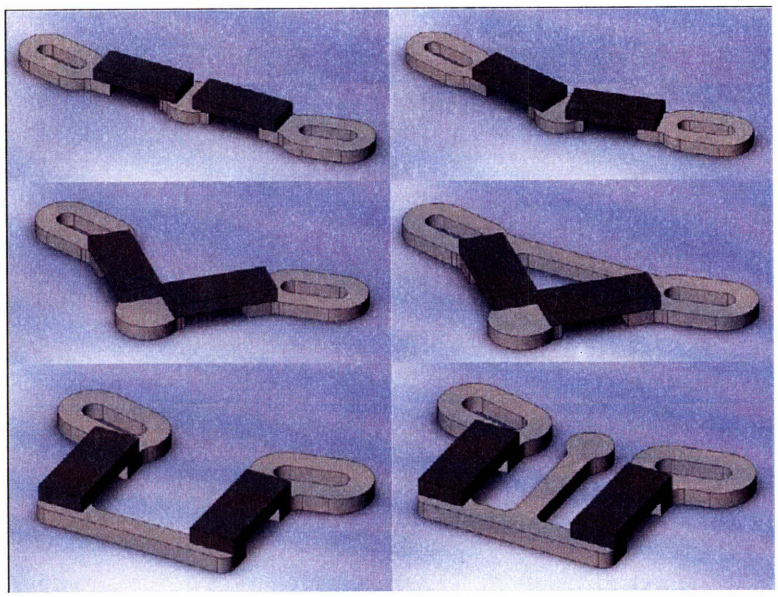

Figure 4-7 Schematic view of six Mechanical Gyroscope Stimulators made of PZT benders (dark gray) and silicon parts (light gray).

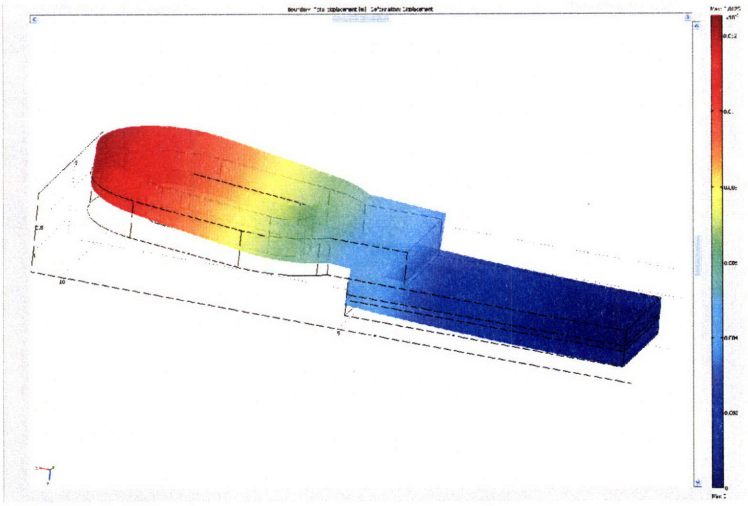

Figure 4-8 FEA modeling of bender actuation.

The benders are attached onto shackle parts by epoxy, and the entire device is then pushed off the wafer. By this means, the first workable MGS was assembled as shown in Figure 4-9. The straight beam actuator (top-left design in Figure 4-7) was also tried on a living Manduca sexta moth, with antennae passing through the shackle ring holes and the middle of the shackle waxed to the moth head (Figure

4-10).

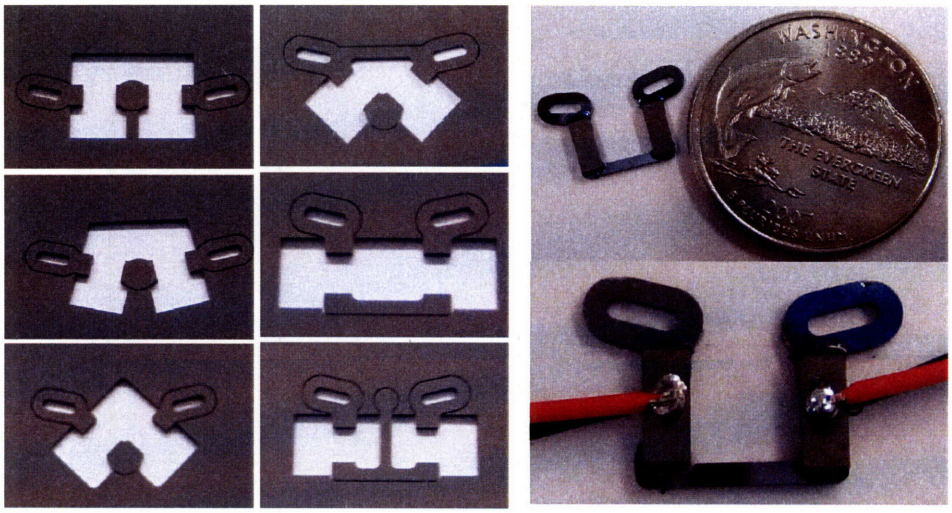

Figure 4-9 The 1st Mechanical Gyroscope Stimulator. Silicon parts are fabricated and kept on wafer (left); PZT benders are attached and the shackle is push off the wafer (top right); and wires are soldered to complete the assembly (bottom right).

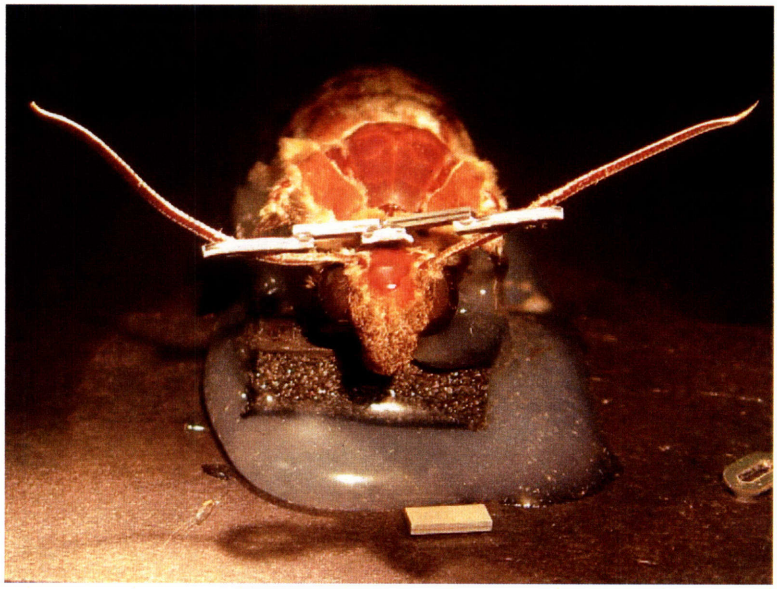

Figure 4-10 Bender-shackle on Manduca sexta.

The PZT bender-shackle is the first MGS device we tried on a moth. It can generate adequate deflection magnitude, however, it is apparently too big for the moth and interferes with the moth's flight. For practical use, the device needs to be smaller.

4.4 Piezoelectric Stack Actuation

Piezoelectric stack actuators are assembled with thin wafers of electro-active ceramic material electrically connected in parallel. Each layer has its polarization direction opposite to those of the adjacent layers, and all the layers expand or contract simultaneously when an electric field is applied (Figure 4-11). The tiny motions of each layer contribute to the overall displacement. Due to the multi-layer geometry, the operation voltage of the piezoelectric stack is reduced to ~100V instead of thousands of volts for the same size piezoelectric bulk devices.

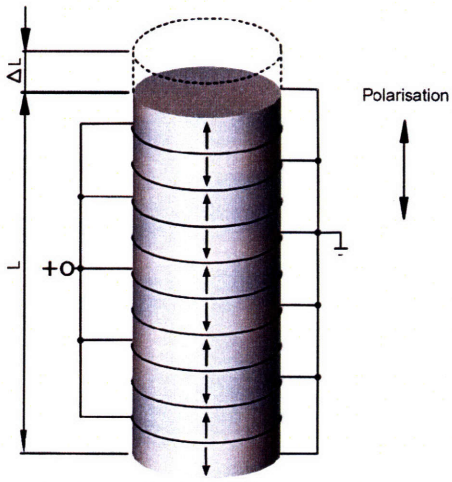

Figure 4-11 Design of a piezo stack actuator.

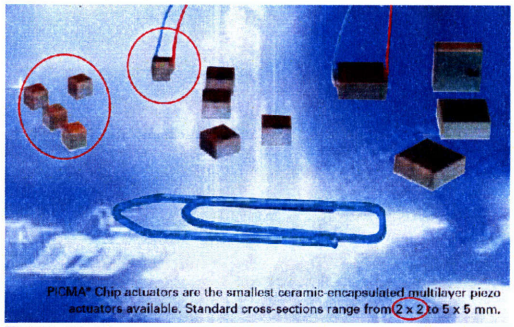

Displacement [µm @ 100 V] ±20%	Blocking force [N]	Electrical capacitance [nF] ±20%	Resonant frequency [kHz]
2.2	> 250	25	> 300

Figure 4-12 Piezo stacks from PI.

Miniature piezoelectric stacks are available with a variety of dimensions from Physik Instrumente (PI) GmbH & Co. KG. The smallest stack is $2\times2\times2$ mm with the displacement up to 2.2µm as highlighted in Figure 4-12. With such stacks, we are then able to assemble smaller actuating shackles, and two designs are illustrated in Figure 4-13. With the left design, we can actuate the two antennae independently, while with the right one we pull or push both antennae simultaneously. For the independent operation stimulator, the middle attaching part or the two end rings are also designed with different sizes and shapes. One appropriate piezo-stack shackle was mounted on a moth, as shown in Figure 4-14.

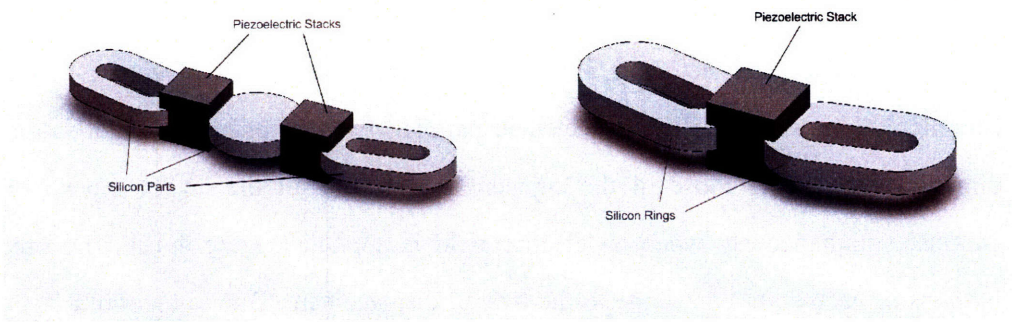

Figure 4-13 Designs of piezo-stack shackles.

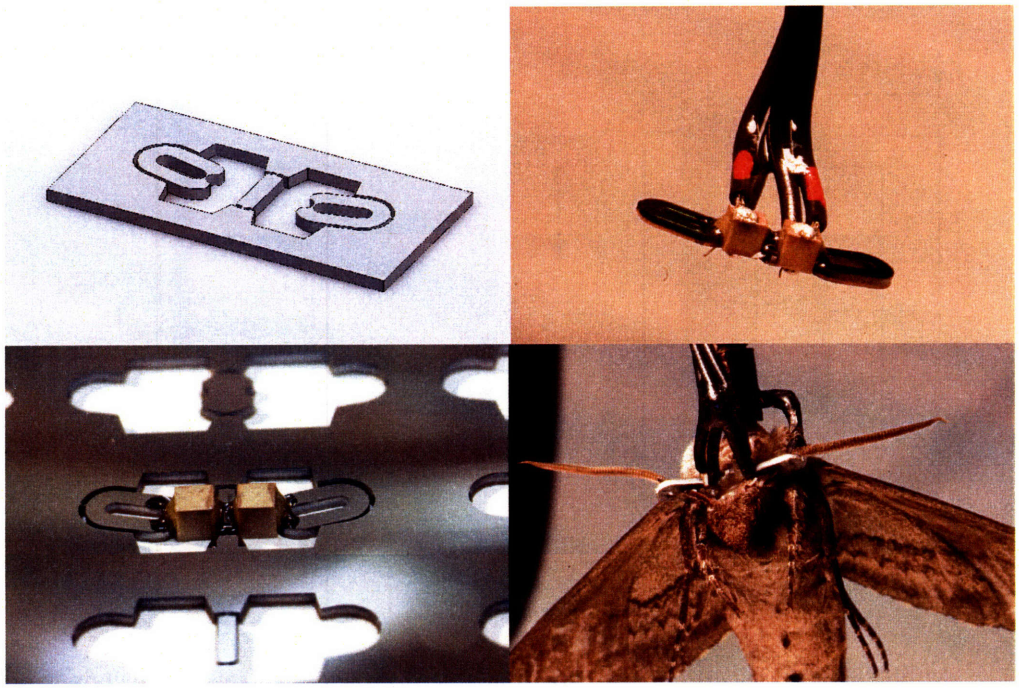

Figure 4-14 The 2nd Mechanical Gyroscope Stimulator: schematic view of the silicon parts (top left); piezo stacks glued on wafer (bottom left); completed stimulator (top right); and the tested moth with stimulator on head (bottom right).

The 2nd MGS device was made by similar means like the bender-shackle in Section 4.3. Piezo stacks were glued onto silicon parts with UV-epoxy and then soldered with wires. The stimulator was then mounted onto the moth, with antennae passing through the ring holes and the middle section waxed onto the moth's head. The moth was stimulated while resting or flying with this actuator, and the testing results are discussed in Chapter 6 (Live Testing).

Chapter 5 Micro-lever Actuation Amplifier

5.1 Motivation

The actuators in Chapter 4 are capable of generating deflections of the order of microns, and a larger displacement is always favorable to stimulate the moth. On the other hand, piezoelectric benders and stacks provide a force much bigger than needed as a MGS device. Thus, can we achieve a greater stimulation magnitude by using the excess force?

A lever is a rigid object that couples the mechanical force and the distance. For the lever shown in Figure 5-1, if a 5μm displacement is applied at the load point A, the endpoint deflection will reach 144.4μm.

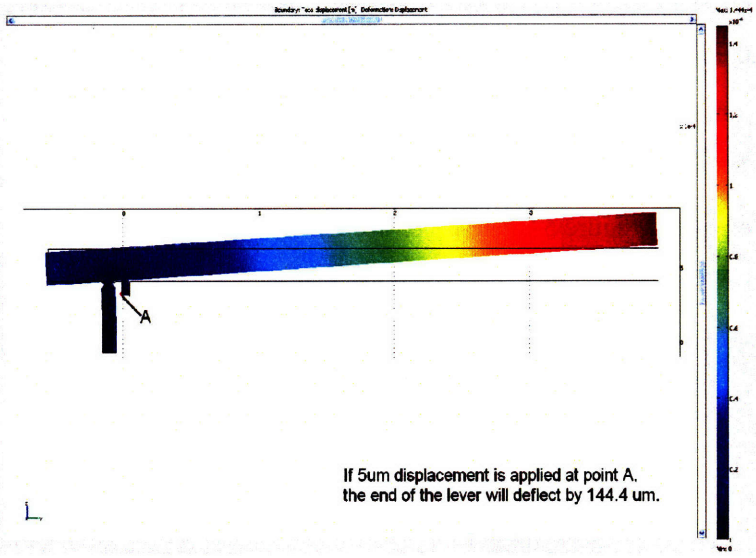

Figure 5-1 Demonstration of the micro-lever displacement amplifier.

Based on the leverage mechanism, a micro-lever is designed to amplify the actuation (Figure 5-2). In this design, a piezo bender is used to demonstrate the lever amplification, with modeling and testing discussed in the rest of this chapter.

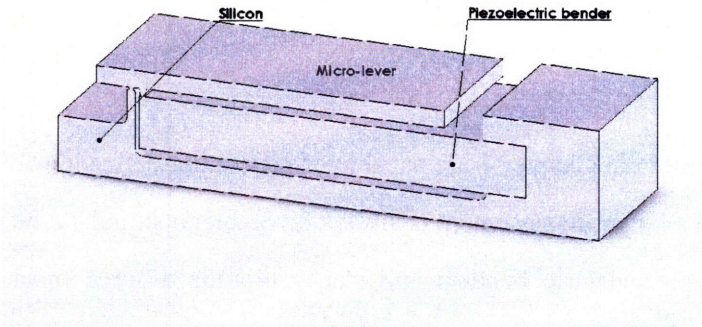

Figure 5-2 Schematic view of a micro-lever.

5.2 Modeling

The fabricated micro-levers have similar structures as shown in Figure 5-1, with the in-plane depth set by the thickness of the silicon wafer which is about 680μm. The horizontal lever beam is 4mm long and 200μm high, and the vertical supporting beam is 100μm wide. Micro-levers with a variety of neck widths and load point offsets, defined in Figure 5-3, are modeled and tested.

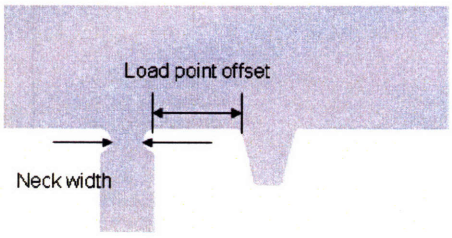

Figure 5-3 Definition of neck width and load point offset.

(1) Micro-lever Neck Design

For a certain neck width, the shape of the neck plays a role in determining the maximum stress. For example, the three levers in Figure 5-4 (B-D) have the same neck width of 30μm but different shapes. The curvature radii are 35μm, 20μm, 35μm,

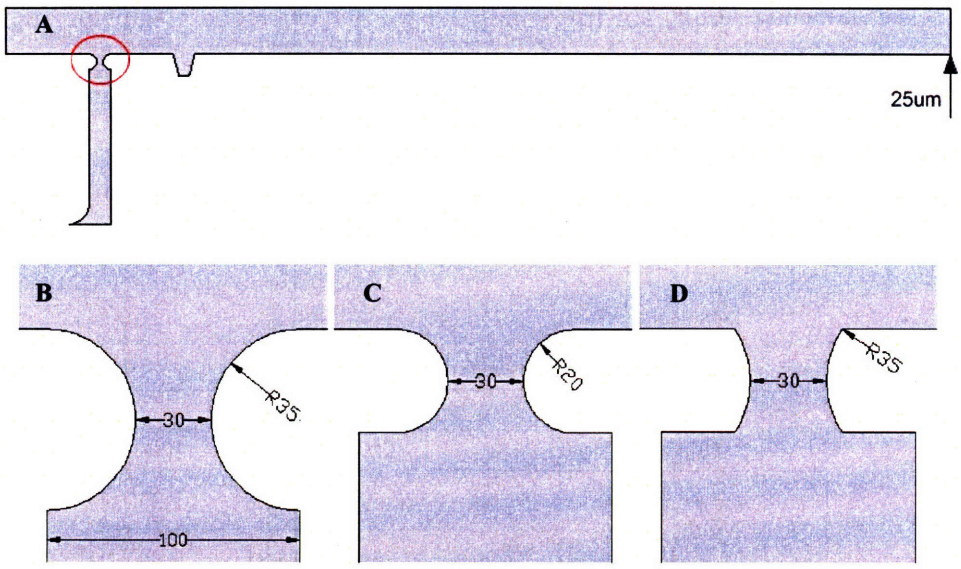

Figure 5-4 Designs of 30μm-wide micro-lever neck (A: schematic view of the micro-lever with endpoint deflection of 25μm; B-D: necks with various curvature radii and neck locations).

respectively, and the neck of (B) is 15μm lower than (C) and (D). If the endpoint deflections of the levers reach 25μm, the von Mises stress at the necks will vary from 198.6 MPa (B), 261.6 MPa (C), to 230.2 MPa (D) from FEA modeling. At the same neck height, the bigger the curvature radius, the lower the stress is (C:D); while with the same radius of 35μm, the half circle geometry is better than a less-than-half circle one in reducing the stress (B:D). Thus, the micro-levers are designed with half- circle-shaped necks and the curvature radius equal to half of the difference between the support beam width (100μm) and the neck width (30, 40, or 60μm).

$$R = (w_{s.b.} - w_{neck})/2 = (100\mu m - w_{neck})/2$$

(2) Actuation Amplification Modeling

A series of micro-levers are analyzed by finite element method with COMSOL Multiphysics. The shape of the neck is designed like the one in Figure 5-4(B). Neck width is set as 30, 40, or 60μm, and the load point offset is 150, 300, 500, or 1000μm. The piezo benders are the ones described in Section 4.3, and 1mm of the bender length will be fixed inside the silicon frame and thus the effective bender length is

set as 4mm in the modeling. The micro-lever is 680μm thick into the plane.

The modeling results are listed in Table 5-1 for deflection magnitude and in Table 5-2 for the maximum von Mises stress concentrated at the neck points. 3-D illustrations are also shown in Figure 5-5 and Figure 5-6, respectively. For more details about FEA modeling results, please refer to Appendix C2 (Modeling of Micro-Lever Actuation Amplifier).

Table 5-1 Endpoint deflection of micro-levers.

Endpoint Deflection (μm) ↘		Load Point Offset (μm)			
		150	300	500	1000
Neck Width (μm)	30	30.68	22.79	16.28	9.37
	40	27.09	21.54	15.81	9.30
	60	24.00	20.32	15.35	9.22

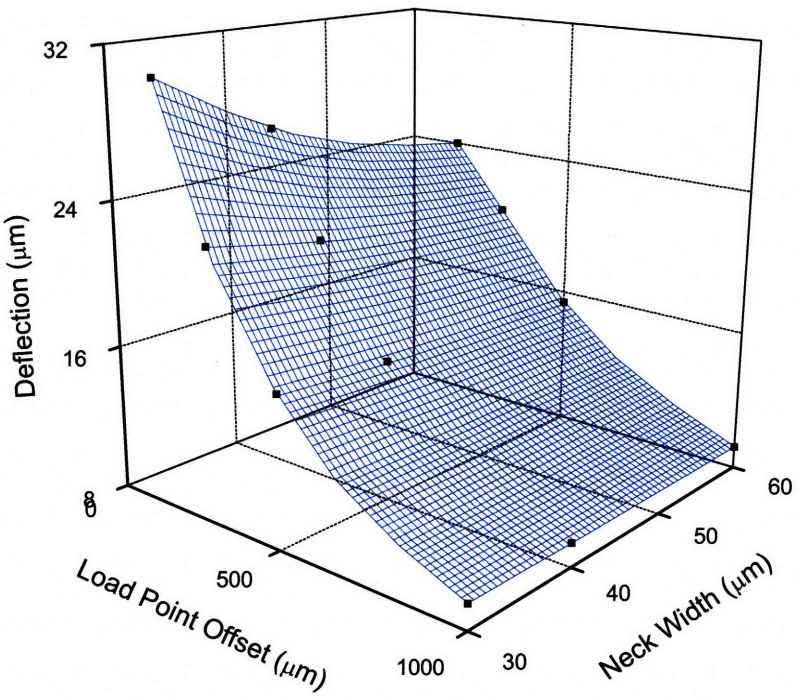

Figure 5-5 Endpoint deflection of micro-levers (FEA modeling).

Table 5-2 Maximum von Mises stress of micro-levers.

Maximum Stress (MPa) ↘		Load Point Offset (μm)			
		150	300	500	1000
Neck Width (μm)	30	271.9	263.4	151.3	88.7
	40	216.4	171.3	134.2	67.1
	60	147.4	124.2	100.7	59.4

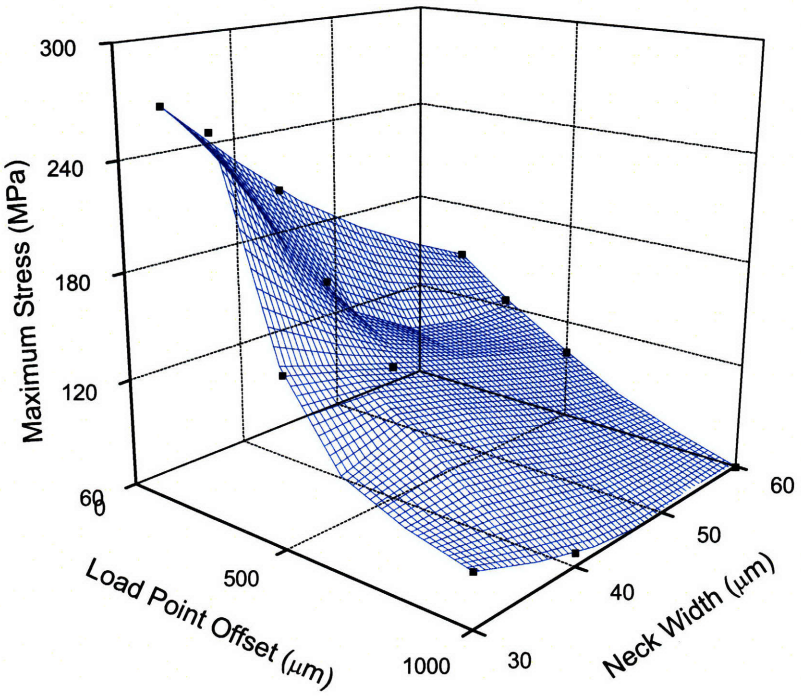

Figure 5-6 Maximum von Mises stress of micro-levers (FEA modeling).

The free deflection of a 4mm long bender is 2.72μm in FEA modeling, and the endpoint displacement of the micro-lever is around one order higher if the load point offset is less than 300μm. It also clearly shows that both the endpoint deflection of the micro-lever and the von Mises stress concentrated at the neck point follow the same trend, and they increase by decreasing the load point offset or the neck width. And with the same load point offset, though the deflection does not increase much by shrinking the neck width, the stress is greatly relieved.

Micro-levers were assembled for testing. First, the piezo bender is fixed inside the silicon frame with epoxy. Then wires are soldered onto the top and bottom electrodes of the bender. Finally, the tip of the bender is secured with the silicon load point (so-called "contact point") by applying a tiny drop of epoxy (Figure 5-7).

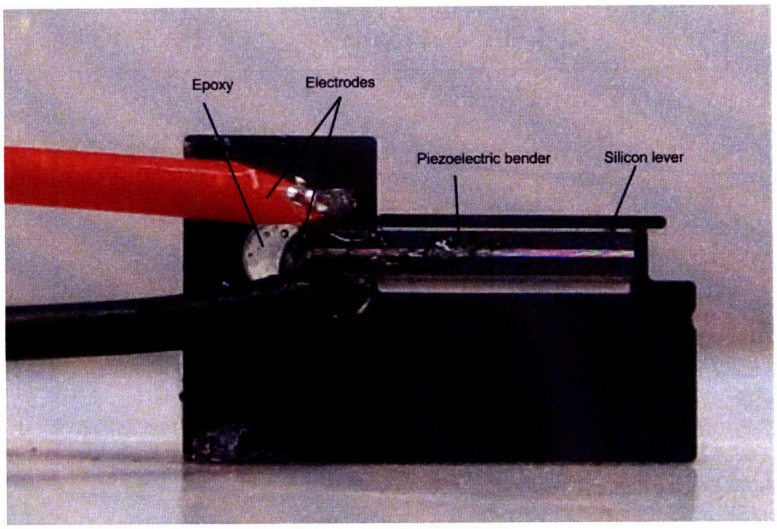

Figure 5-7 An assembled micro-lever.

5.3 Experimental Results

By considering the assembly difficulty and the amplification efficiency, three micro-levers are chosen, and the endpoint deflections were measured with a Polytec Scanning Vibrometer 200. The three devices have the same load point offsets of 300μm, and their neck widths are 30μm, 40μm, and 60μm, respectively. One of the three devices is shown in Figure 5-8. Micro-levers are fixed on glass slides with epoxy for test handling.

The principle of the deflection measurement is demonstrated in Figure 5-9. In our experiments, a sinusoidal signal causes the piezo bender to vibrate. The measurement beam from the interferometer in the scanning head is positioned to a scan point on the measurement object (the bender or the lever) by means of mirrors and is scattered back, and the reflected laser light interferes in the scanning head with the reference beam of the interferometer. A photodetector records the interfered

scattered light, and a decoder in the vibrometer provides a voltage which is proportional to the velocity of the vibration parallel to the measurement beam. The deflection magnitude is calculated from the vibration velocity.

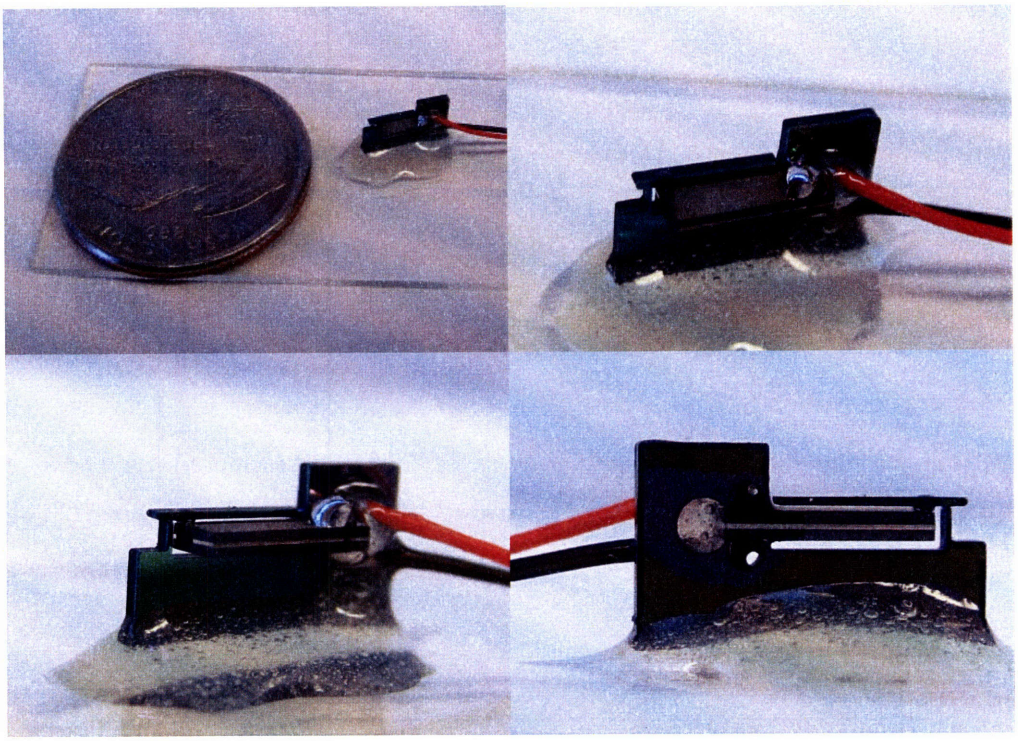

Figure 5-8 A tested micro-lever. Top-left: micro-lever with a quarter; top-right: top view; bottom-left: front view; bottom-right: back view.

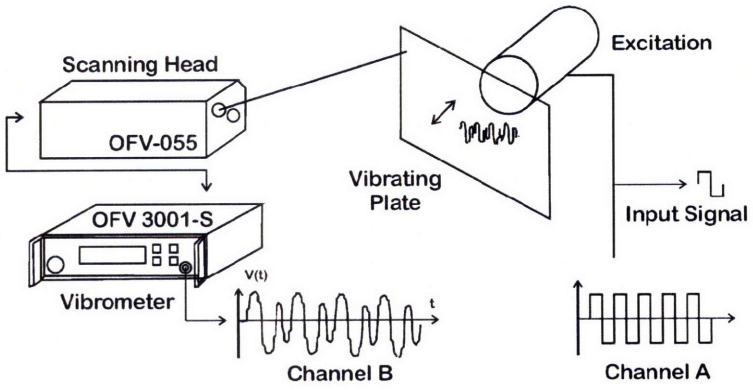

Figure 5-9 Principle of data recording with the PSV.

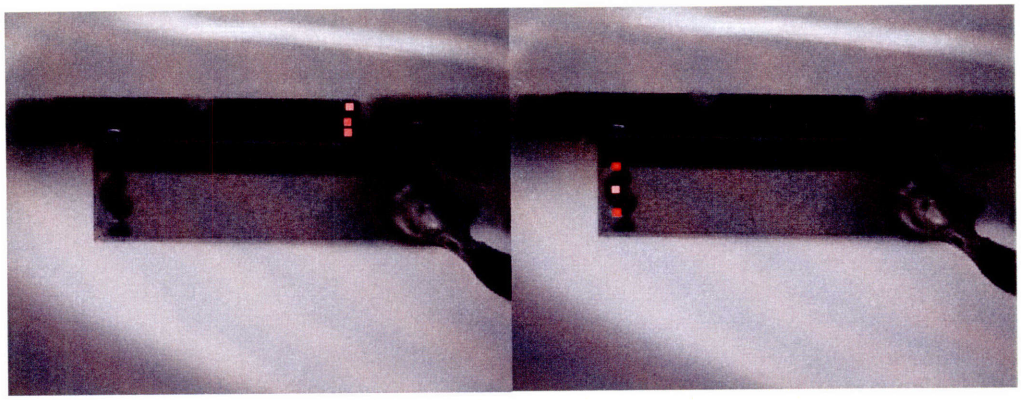

Figure 5-10 Deflection testing points (top view of the micro-lever). Left: testing points of the micro-lever end; right: testing points of the piezo bender.

Deflecting results of three points were collected and averaged for each measurement (Figure 5-10). The operation electrical frequency is 7.8Hz, and the results for the three devices are listed in Table 5-3. The micro-lever endpoint deflection magnitudes are 28.27, 21.63, 17.49μm for micro-levers with 30, 40, 60μm in neck width, respectively.

Table 5-3 Experimental results @ 7.8Hz.

Load Point Offset = 300μm		Deflection (μm)		d_2/d_1	Effective Amp. Ratio
		Bender (d_1)	Micro-lever (d_2)		
4mm bender		2.32	--	--	--
Micro-lever Neck Width (μm)	30	1.95	28.27	14.5	12.19
	40	1.80	21.63	12.0	9.32
	60	1.36	17.49	12.9	7.54

At the testing frequency of 7.8Hz, the 4mm bender itself deflects by 2.32μm, which is close to the modeled 2.72μm at static condition. The micro-levers deflect 17.49, 21.63, and 28.27μm with the neck widths of 30, 40, and 60μm, respectively. The experimental results are quite consistent with the FEA prediction, amplifying the bender deflection by an order of magnitude successfully.

The differences between experimental and FEA modeling results are also observed. First, the load point offsets are not exactly 300μm as designed because of

the application of epoxy on the contact points; and second, though the piezo benders are carefully aligned with the silicon frames under stereo optical microscope, the manually assembly offsets cannot be avoided. The two effects cause the variation of the amplification structures and the ratio of d_2/d_1. Combining with the variation of material properties and instrumental errors, the effective amplification ratios (E.A.R.), which are the deflection ratios of the micro-lever over the free bender, are biased at a small scale from the FEA modeling results.

Table 5-4 Comparison of experimental and FEA results

Load Point Offset = 300μm		Experimental		FEA Modeling	
		d_2/d_1	E.A.R.	d_2/d_1	E.A.R.
Micro-lever Neck Width (μm)	30	14.5	12.19	~10	8.38
	40	12.0	9.32		7.92
	60	12.9	7.54		7.47

Chapter 6 Live Testing

The Mechanical Gyroscope Stimulator #2, which is described in Section 4.4 Figure 4-14, was mounted onto a living Manduca sexta moth, which was subsequently stimulated. A tiny magnet was glued on the moth thorax with epoxy, and the moth was stabilized by fixing the magnet to the iron probe. The experimental setup is shown in Figure 6-1. Voltage pulses were then applied while the moth was resting or flapping its wings. The moth was raised by our collaborators in University of Washington at Seattle, and we brought our MGS devices to Seatlle and did the live testing there. The peak operational voltage is 100 volts. The LED indicated the impulses.

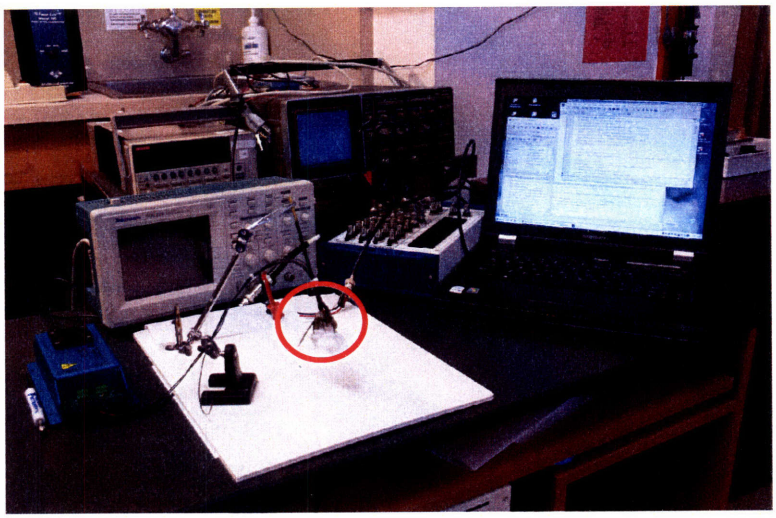

Figure 6-1 Experimental setup of MGS live testing.

The live testing was recorded, showing the moth's strong reaction to the antennal stimulation. With an impulse applied, while the moth was resting, the moth stretched its six legs and started flipping the wings; while the moth was flapping wings as it does during flying, the moth swung the legs and the wing flapping magnitude was enlarged. The same results were observed when either the left or right piezo stack was activated. In addition, the moth also swung its abdomen when stimulated under

all circumstances. Images captured from the experimental video are shown in Figure 6-2 and Figure 6-3.

It is exciting to see all the moth responses to the mechanical stimulus. It is very likely that the moth flight can be affected by the abdomen motion, and thus we are one step closer to our final goal to achieve controllable moth flight.

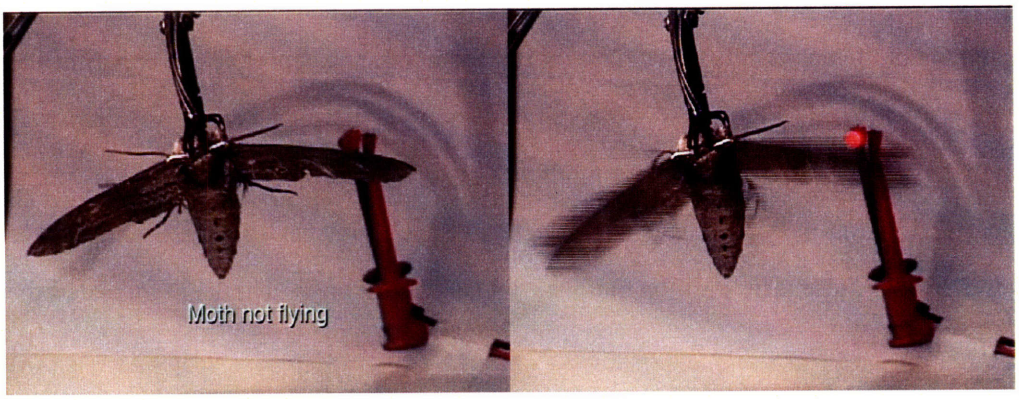

Figure 6-2 MGS stimulating while the moth's resting.

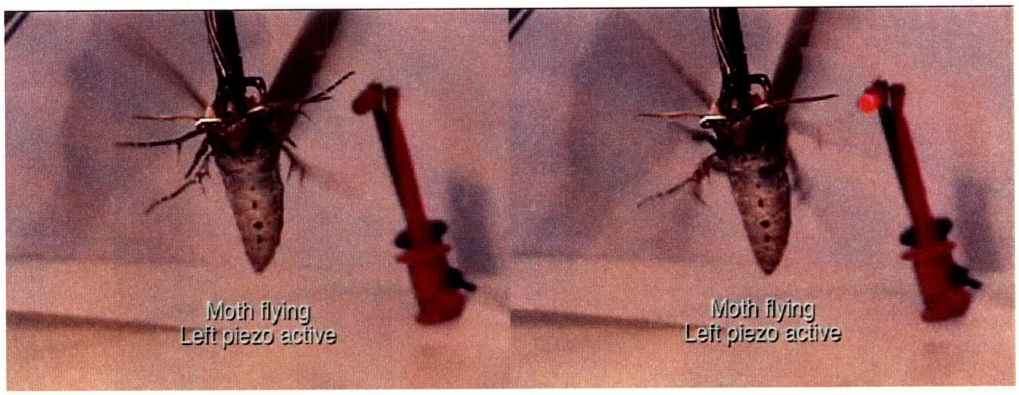

Figure 6-3 MGS stimulating while the moth's flapping wings.

Chapter 7 Future Work

Future work will focus on further device minimization, actuation amplification, and multi-degree actuation.

(1) Further Minimization

The Mechanical Gyroscope Stimulator #2 fits the moth, but if it is further miniaturized, it will definitely work better by reducing the moth's burden. First, the silicon wafer that we were using is 680μm thick. This led us to consider the use of a thinner silicon wafer which will lessen the device weight and probably will still be good enough for operation. Second, the smallest piezo stack we used was purchased directly from PI, but the vendor also offers customization options. Thus we can order smaller piezo actuators; at least we can reduce the height of the stack to lighten the actuator parts.

(2) Actuation Amplification

The actuation amplifiers were modeled and tested with the PZT benders. In the future, such leverage structures need to be modeled and tested with piezo stacks which are able to offer comparable actuation magnitude but smaller than the benders we used. Also the amplifier should be minimized to fit the moth.

(3) Multi-degree Actuation

All the devices modeled and fabricated to now actuate in only one degree, though the benders are vertically actuating while the stacks are horizontally actuating. Two-degree or three-degree actuation concepts and the devices are going to be developed.

However, the focus of attention is subject to change depending on what our

collaborators and other scientists discover or observe regarding the moth flight mechanism.

Chapter 8 Conclusions

Our project was to aid the study of moth flight mechanisms by mechanically stimulating the moth antennae. We first developed a series of mounting structures for the moth antennae, from simple rings, 2-D assembly structures, 3-D assembly structures, to the finally adopted "antennal shackles". The shackles fit the moth very well and form the base for the Mechanical Gyroscope Stimulator (MGS).

Once the mounting kits were selected, we tried to integrate the actuation elements into the shackle structure. Extensive finite element analysis modeling was performed in the design and evaluation stages. COMSOL Multiphysics is the FEA tool used. From the FEA modeling results, we excluded the approach of depositing piezoelectric thin film onto the shackles, and instead, we took several practical approaches, such as attaching the 350~500μm thick PZT sheet onto the shackle, using piezo benders as the actuating beams (MGS #1), and the piezo stack MGS #2. Live testing of MGS #2 was also done by stimulating one moth antenna while the moth was resting or mimicking flying. The moth reacts strongly to the mechanical stimulus, which makes it possible in principle to obtain a flight-controllable cyborg moth.

Actuation amplifiers were also studied, and leverage structures were adopted. The actuation magnitudes were amplified by an order of magnitude and such amplifier might be further minimized and used in later MGS devices.

Appendix

Appendix A Fundamentals of Piezoelectricity Analysis

The piezoelectric effect was discovered by Jacques and Pierre Curie in 1880. If certain crystals are subject to mechanical strain, they are electrically polarized and the polarization degree is proportional to the applied strain. These same materials also deform when they are exposed to an electric field. This has become known as the inverse piezoelectric effect.

The piezoelectric effect exists in a number of naturally-occurring crystals, for instances quartz and lithium niobate. Besides, an important group of piezoelectric materials are the piezoelectric ceramics, of which lead zirconate titanate (PZT) is an example. The piezoelectric devices discussed in this thesis, the piezo film/sheet, piezo benders and piezo stacks, are all made of PZT ceramics, and the materials properties of PZT are crucial to model the devices performance.

PZT ceramics are polycrystalline ferroelectric materials with the perovskite crystal structure. Above a temperature known as the Curie point, this crystal lattice is of cubic symmetry, and the elementary cell is shown in Figure A-1(1). In this structure, positive and negative charges sites coincide, so there are no dipoles present in the material. Below the Curie temperature, the crystal lattice is of tetragonal symmetry and then each cell has an electric dipole (Figure A-1(2)). When an electric

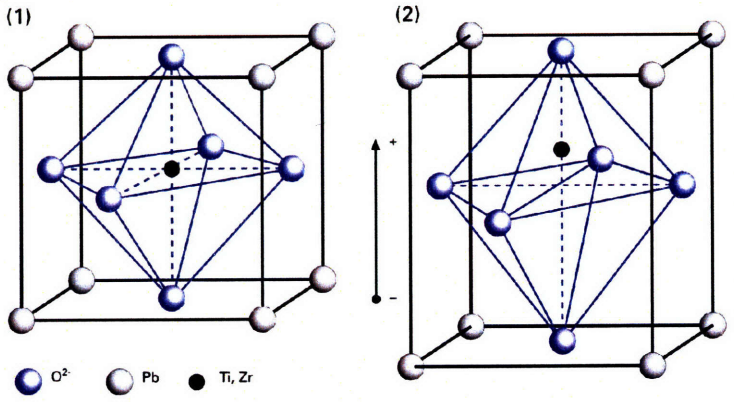

Figure A-1 PZT elementary cell. (1) Cubic lattice; (2) tetragonal lattice.

field is applied, the cell can be reversed or biased.

Piezoelectric effects are strongly orientation dependent. To analyze the piezoelectric devices, the notation conventions are discussed first. PZT ceramics need to be poled in a particular direction, and the direction of positive polarization is chosen to coincide with the Z-axis of an orthogonal system (Figure A-2). Alternatively, the normal stress components along axes X, Y, and Z are denoted by subscripts 1, 2, and 3, respectively. Shear stress and strain components about these axes are denoted by subscripts 4, 5, and 6.

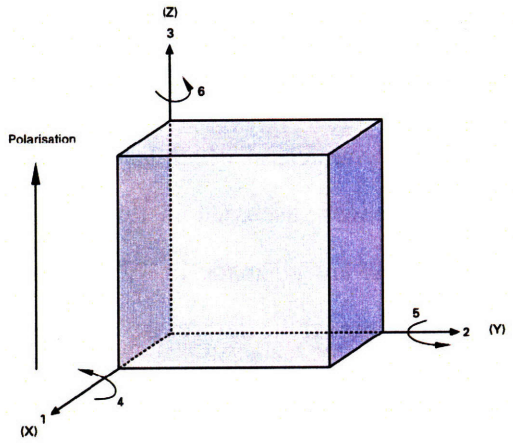

Figure A-2 Illustration of the axes and directions of stress and strain.

In a piezoelectric crystal, the constitutive equation that relates electric polarization (D) and applied mechanical stress (T) is

$$D = dT + \varepsilon E \tag{A-1}$$

where d is the piezoelectric coefficient matrix, ε is the electrical permittivity matrix, and E is the electrical field. The general constitutive equation can be written in the full matrix form (SI units):

$$\begin{bmatrix} D_1 \\ D_2 \\ D_3 \end{bmatrix} = \begin{bmatrix} d_{11} & d_{12} & d_{13} & d_{14} & d_{15} & d_{16} \\ d_{21} & d_{22} & d_{23} & d_{24} & d_{25} & d_{26} \\ d_{31} & d_{32} & d_{33} & d_{34} & d_{35} & d_{36} \end{bmatrix} \begin{bmatrix} T_1 \\ T_2 \\ T_3 \\ T_4 \\ T_5 \\ T_6 \end{bmatrix} + \begin{bmatrix} \varepsilon_{11} & \varepsilon_{12} & \varepsilon_{13} \\ \varepsilon_{21} & \varepsilon_{22} & \varepsilon_{23} \\ \varepsilon_{31} & \varepsilon_{32} & \varepsilon_{33} \end{bmatrix} \begin{bmatrix} E_1 \\ E_2 \\ E_3 \end{bmatrix} \tag{A-2}$$

The terms T_1 through T_3 are normal stresses along axes 1, 2, and 3, and T_4 through T_6 are shear stresses.

The inverse piezoelectric effect is similarly described by Equation (A-3). The total strain (S) is related to both the applied electric field and any mechanical stress (SI units):

$$S = sT + dE \tag{A-3}$$

where S is the strain vector and s is the compliance matrix. Equation (A-3) can be written in a matrix form:

$$\begin{bmatrix} S_1 \\ S_2 \\ S_3 \\ S_4 \\ S_5 \\ S_6 \end{bmatrix} = \begin{bmatrix} s_{11} & s_{12} & s_{13} & s_{14} & s_{15} & s_{16} \\ s_{21} & s_{22} & s_{23} & s_{24} & s_{25} & s_{26} \\ s_{31} & s_{32} & s_{33} & s_{34} & s_{35} & s_{36} \\ s_{41} & s_{42} & s_{43} & s_{44} & s_{45} & s_{46} \\ s_{51} & s_{52} & s_{53} & s_{54} & s_{55} & s_{56} \\ s_{61} & s_{62} & s_{63} & s_{64} & s_{65} & s_{66} \end{bmatrix} \begin{bmatrix} T_1 \\ T_2 \\ T_3 \\ T_4 \\ T_5 \\ T_6 \end{bmatrix} + \begin{bmatrix} d_{11} & d_{21} & d_{31} \\ d_{12} & d_{22} & d_{32} \\ d_{13} & d_{23} & d_{33} \\ d_{14} & d_{24} & d_{34} \\ d_{15} & d_{25} & d_{35} \\ d_{16} & d_{26} & d_{36} \end{bmatrix} \begin{bmatrix} E_1 \\ E_2 \\ E_3 \end{bmatrix} \tag{A-4}$$

For PZT ceramics, the matrices of d, ε, and s are simplified due to their tetragonal symmetric lattice:

$$d = \begin{bmatrix} 0 & 0 & 0 & 0 & d_{15} & 0 \\ 0 & 0 & 0 & d_{15} & 0 & 0 \\ d_{31} & d_{31} & d_{33} & 0 & 0 & 0 \end{bmatrix} \tag{A-5}$$

$$\varepsilon = \begin{bmatrix} \varepsilon_{11} & 0 & 0 \\ 0 & \varepsilon_{11} & 0 \\ 0 & 0 & \varepsilon_{33} \end{bmatrix} \tag{A-6}$$

$$s = \begin{bmatrix} s_{11} & s_{12} & s_{13} & 0 & 0 & 0 \\ s_{12} & s_{11} & s_{13} & 0 & 0 & 0 \\ s_{13} & S_{13} & s_{33} & 0 & 0 & 0 \\ 0 & 0 & 0 & s_{44} & 0 & 0 \\ 0 & 0 & 0 & 0 & s_{44} & 0 \\ 0 & 0 & 0 & 0 & 0 & 2(s_{11} - s_{12}) \end{bmatrix} \tag{A-7}$$

Among all the d constants, d_{33} and d_{31} are sometimes referred to as "piezo gain". d_{33} describes the strain parallel to the polarization vector of the ceramics (thickness)

and is used when calculating the displacement of stack actuators; d_{31} is the strain orthogonal to the polarization vector (width) and is used for calculating tube and strip actuators. Typical matrices d and s for PZT-5H are:

$$d = \begin{bmatrix} 0 & 0 & 0 & 0 & 741 & 0 \\ 0 & 0 & 0 & 741 & 0 & 0 \\ -274 & -274 & 593 & 0 & 0 & 0 \end{bmatrix} \times 10^{-12} C/N \qquad \text{(A-8)}$$

$$s = \begin{bmatrix} 16.5 & -4.78 & -8.45 & 0 & 0 & 0 \\ -4.78 & 16.5 & -8.45 & 0 & 0 & 0 \\ -8.45 & -8.45 & 20.7 & 0 & 0 & 0 \\ 0 & 0 & 0 & 43.5 & 0 & 0 \\ 0 & 0 & 0 & 0 & 43.5 & 0 \\ 0 & 0 & 0 & 0 & 0 & 42.6 \end{bmatrix} \times 10^{-12} Pa^{-1} \qquad \text{(A-9)}$$

Appendix B Heat Sink

To achieve controllable remote flight machines, the power supply is a critical issue. Our collaborators are trying to harvest energy from the moth itself, such as thorax motion and also the thermal difference between the moth body and the environment.

Thermoelectricity refers to a class of phenomena in which a temperature difference creates an electric potential or an electric potential creates a temperature difference. In modern technical usage, the term almost always refers collectively to the Seebeck effect, Peltier effect, and the Thomson effect. All these effects have been employed in devices using suitable compound semiconductors: thermogenerator devices for converting heat into electric energy (Figure B-1) and Peltier cooler devices for pumping heat using a current flow. The heat sink is attached on the Cold Side or Hot Side to conduct the heat. Silicon is a good choice to build the heat sink because of its good thermal properties. The thermal conductivity of silicon is 149 $W \cdot m^{-1} \cdot K^{-1}$, close to that of aluminum which is 237 $W \cdot m^{-1} \cdot K^{-1}$. Besides, silicon can be precisely fabricated at micro-scale.

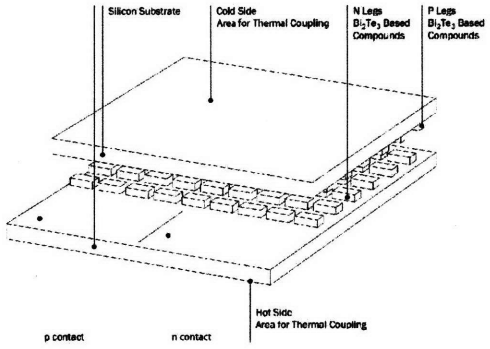

Figure B-1 Schematic view of a thermogenerator.

The silicon heat sinks we made for our collaborators are other examples of three-dimensional assembly. Finger-array and the base are fabricated separately, and the parts are then manually assembled and fixed with epoxy. The fingers are inserted

into the moth body, and also pointed out to air. Finally, a power of ~50μW was obtained by a specially designed thermogenerator attached with the heat sinks.

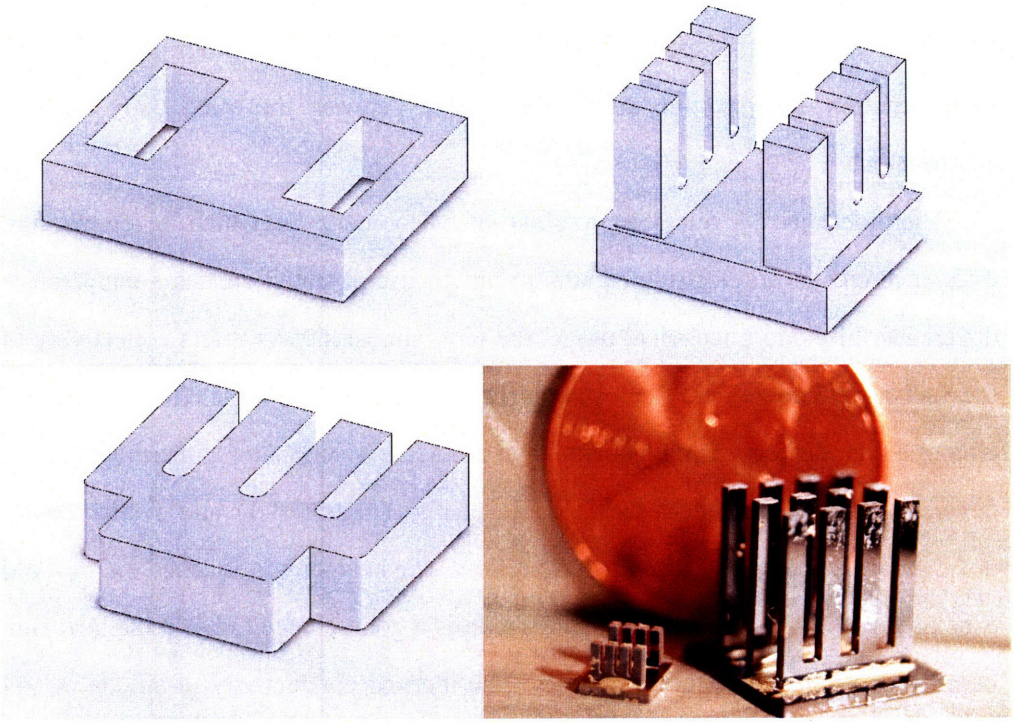

Figure B-2 The heat sink. Top-left: base part; bottom-left: erected part; top-right: schematic view of the heat sink; bottom-right: fabricated and assembled heat sinks.

Appendix C Modeling of Piezoelectric Actuation

C1 Modeling of Piezoelectric Bi-morph

Silicon half-shackle is fixed with PZT film/sheet on the top surface. The PZT film/sheets are 5mm long and 2mm wide. The thickness of the silicon half-shackle is 660μm, and the thicknesses of PZT film/sheet vary from 5μm to 5000μm in the following FEA modeling. The FEA modeling results are shown in Table C-1 and plotted in Figure C-1. Individual results are also shown in Figure C-2 ~ Figure C-20.

Table C-1 FEA modeling results of silicon half-shackle bound with PZT film/sheet.

PZT(μm)	Deflection(μm)	PZT(μm)	Deflection(μm)	PZT (μm)	Deflection(μm)
5	0.0575	350	1.46	800	1.168
10	0.314	400	1.454	1000	1.006
30	0.323	450	1.44	1500	0.712
50	0.504	500	1.404	2000	0.527
100	0.867	550	1.368	5000	0.294
200	1.256	600	1.336		
300	1.437	660	1.286		

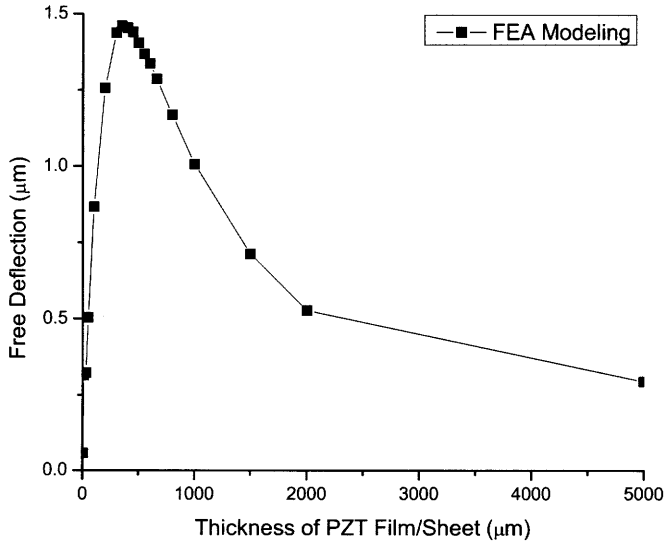

Figure C-1 FEA modeling results of silicon half-shackle bound with PZT film/sheet.

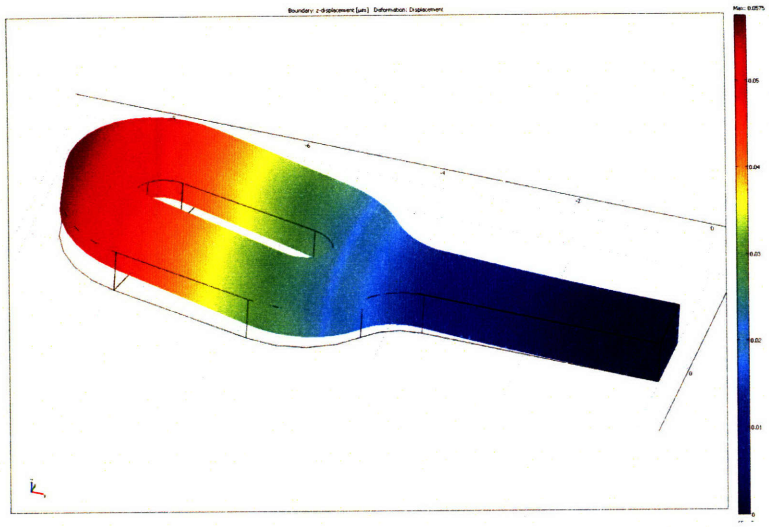

Figure C-2 Silicon half-shackle with 5μm thick PZT film/sheet.

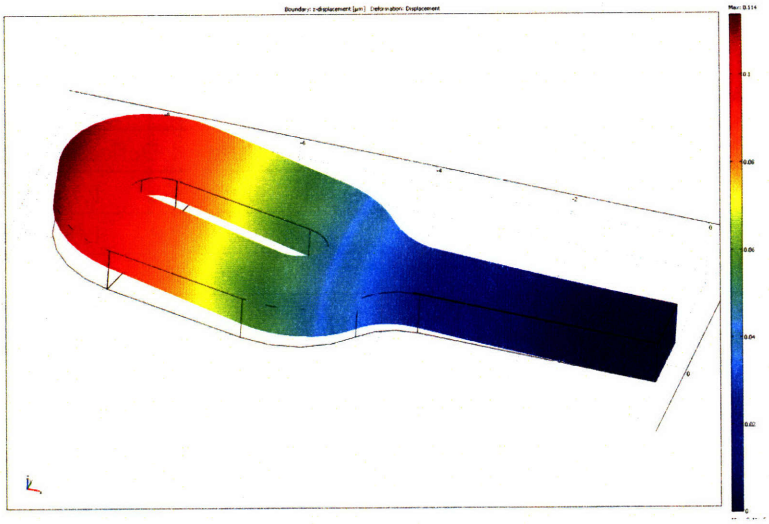

Figure C-3 Silicon half-shackle with 10μm thick PZT film/sheet.

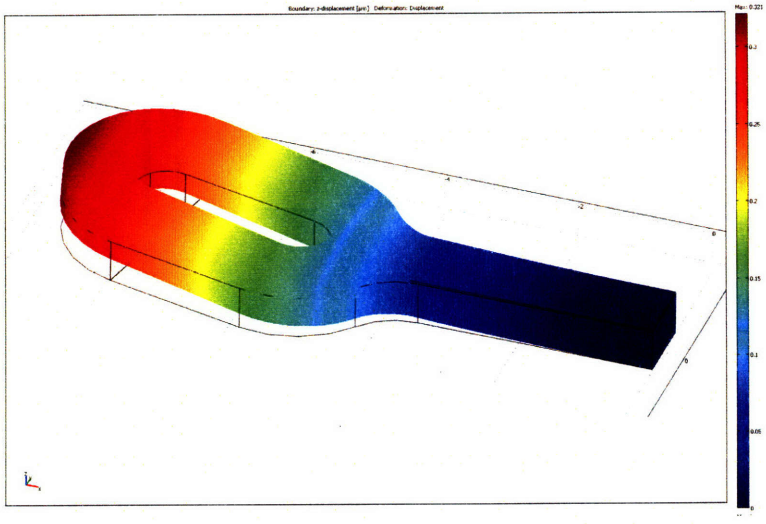

Figure C-4 Silicon half-shackle with 30μm thick PZT film/sheet.

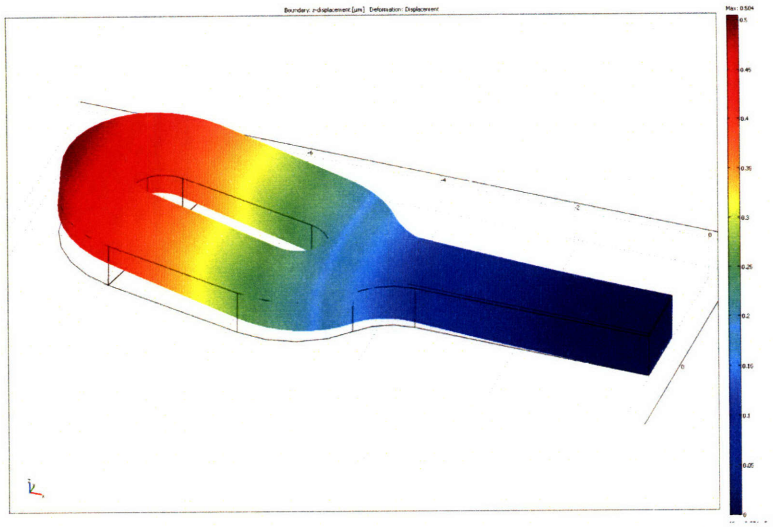

Figure C-5 Silicon half-shackle with 50μm thick PZT film/sheet.

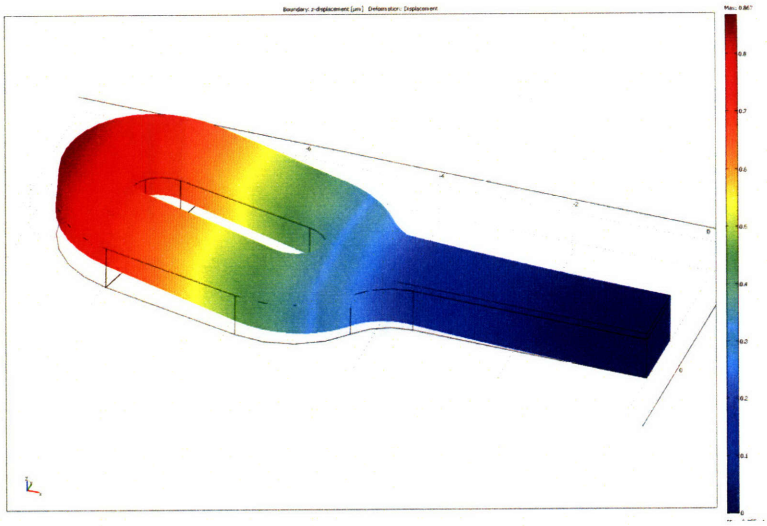

Figure C-6 Silicon half-shackle with 100μm thick PZT film/sheet.

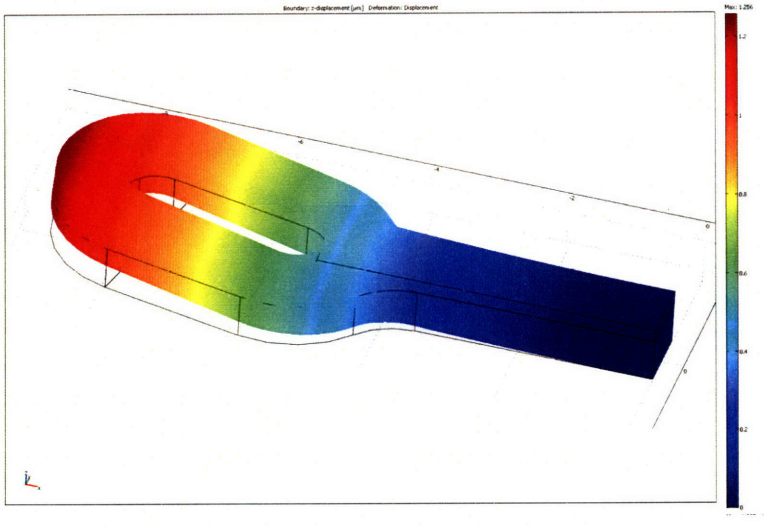

Figure C-7 Silicon half-shackle with 200μm thick PZT film/sheet.

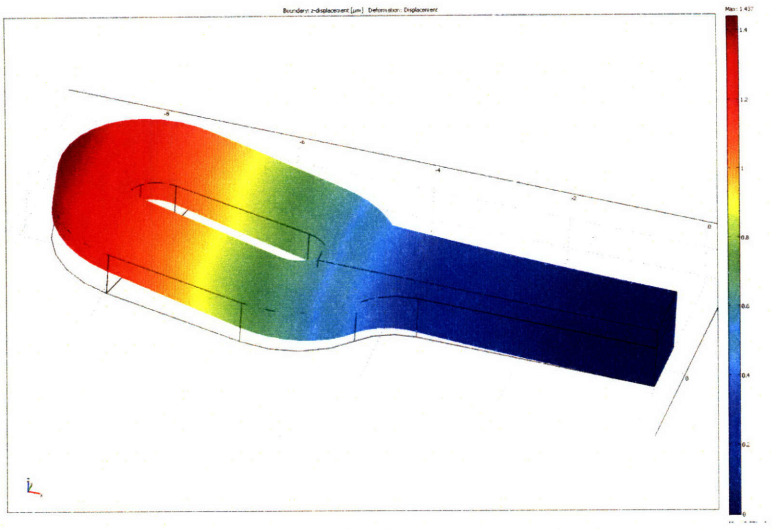

Figure C-8 Silicon half-shackle with 300μm thick PZT film/sheet.

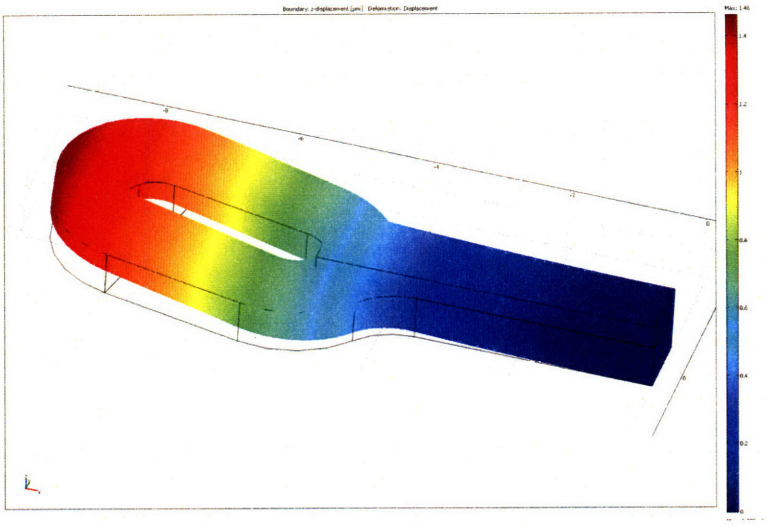

Figure C-9 Silicon half-shackle with 350μm thick PZT film/sheet.

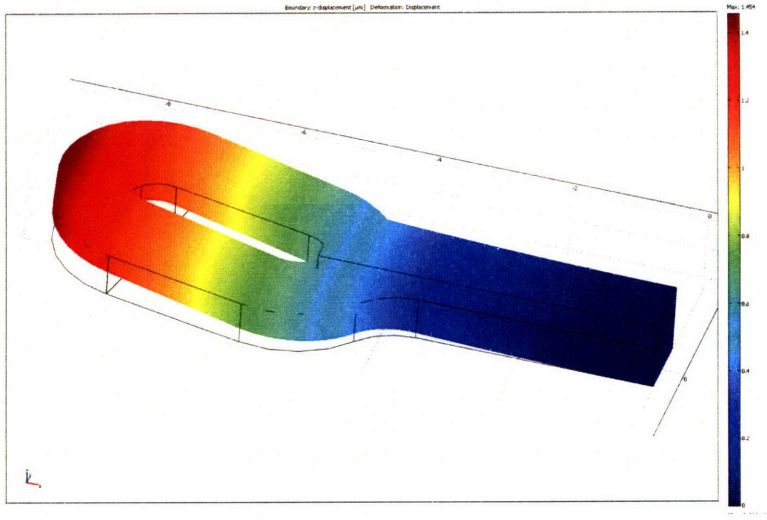

Figure C-10 Silicon half-shackle with 400μm thick PZT film/sheet.

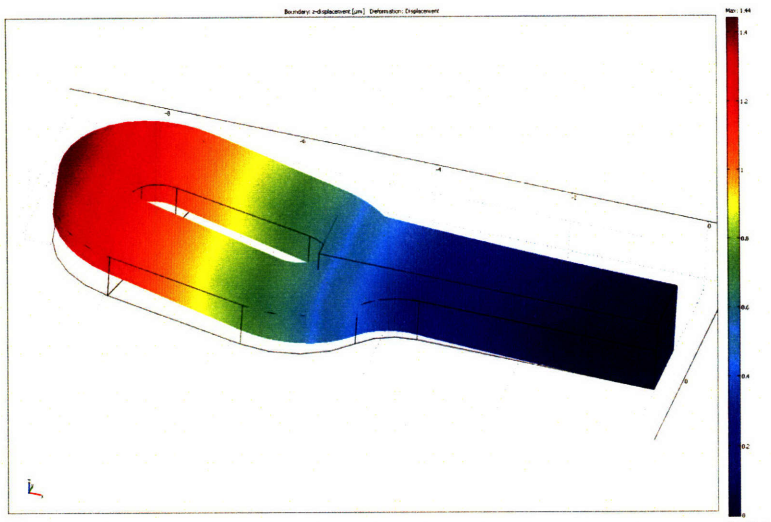

Figure C-11 Silicon half-shackle with 450μm thick PZT film/sheet.

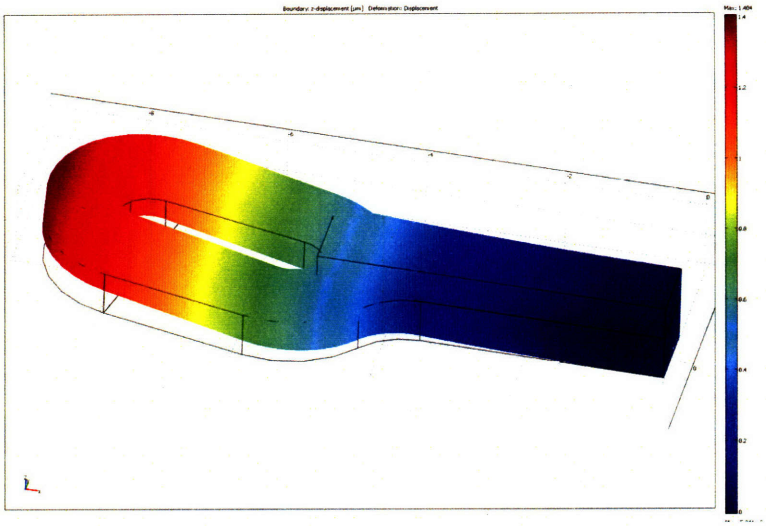

Figure C-12 Silicon half-shackle with 500μm thick PZT film/sheet.

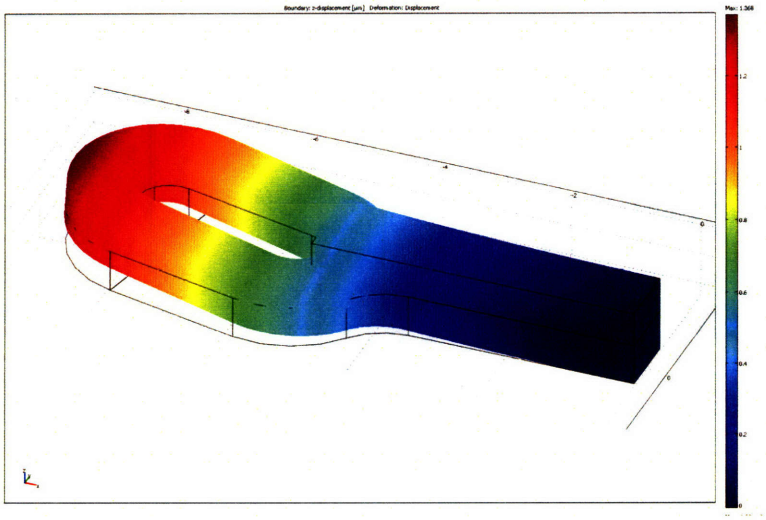

Figure C-13 Silicon half-shackle with 550μm thick PZT film/sheet.

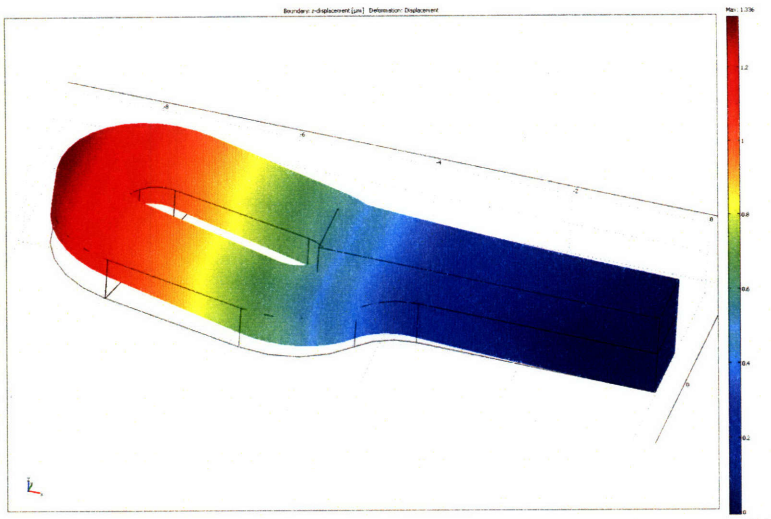

Figure C-14 Silicon half-shackle with 600μm thick PZT film/sheet.

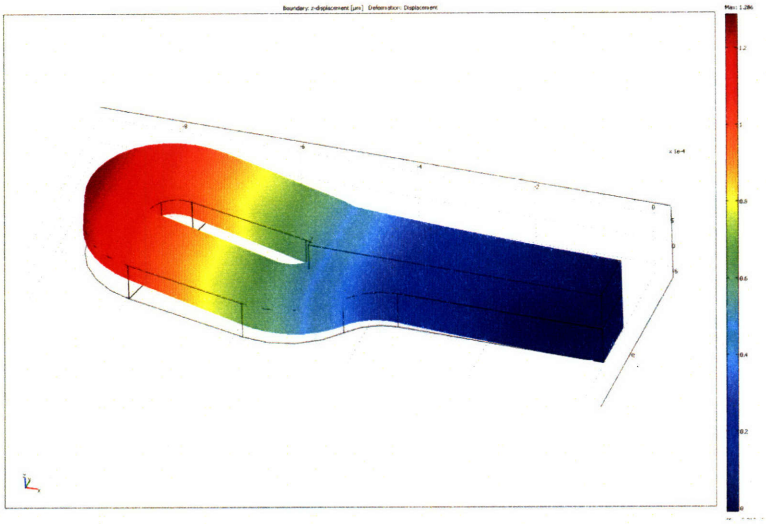

Figure C-15 Silicon half-shackle with 660μm thick PZT film/sheet.

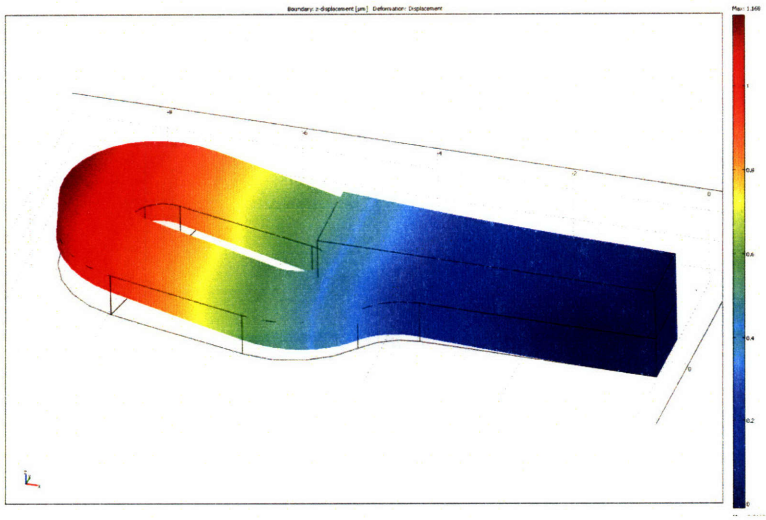

Figure C-16 Silicon half-shackle with 800μm thick PZT film/sheet.

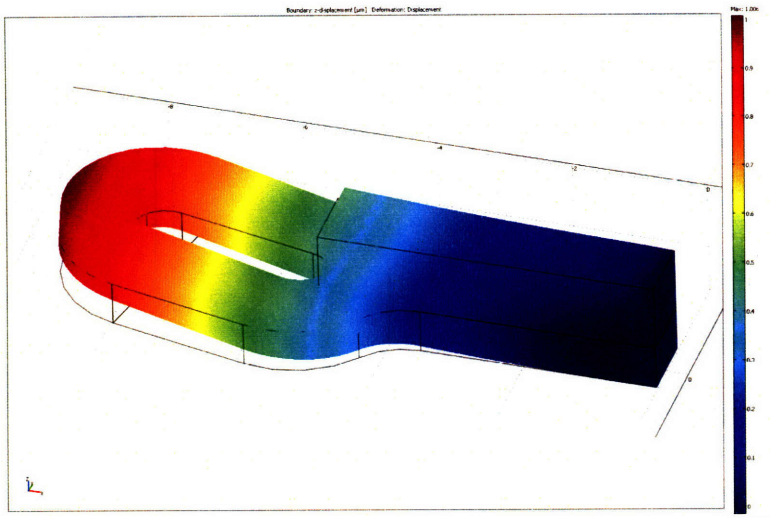

Figure C-17 Silicon half-shackle with 1000μm thick PZT film/sheet.

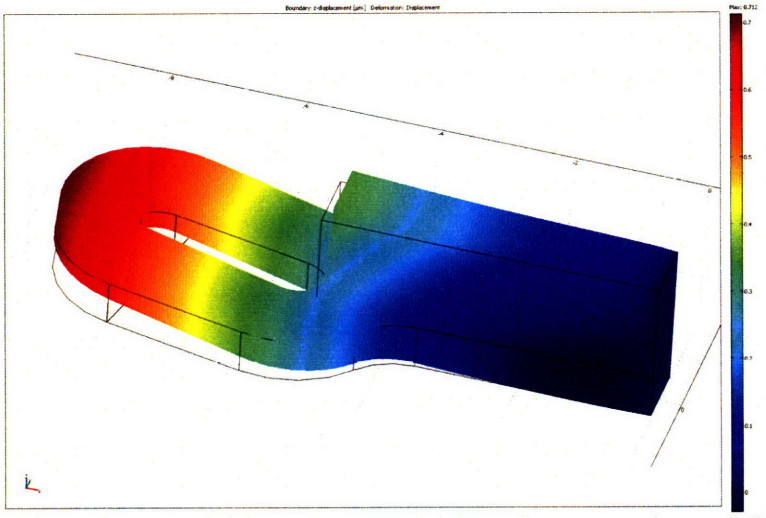

Figure C-18 Silicon half-shackle with 1500μm thick PZT film/sheet.

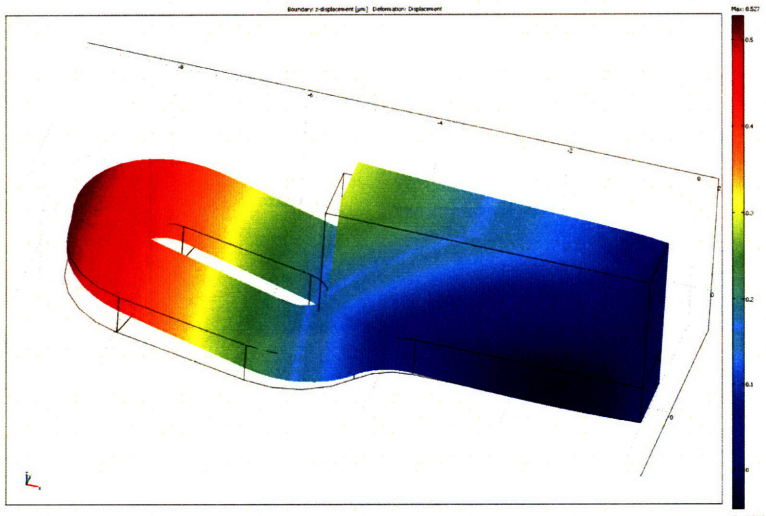

Figure C-19 Silicon half-shackle with 2000μm thick PZT film/sheet.

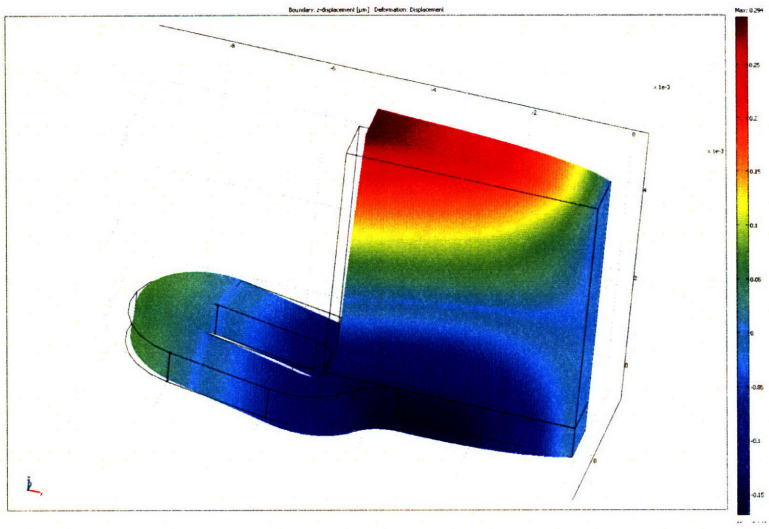

Figure C-20 Silicon half-shackle with 5000μm thick PZT film/sheet.

C2 Modeling of Micro-Lever Actuation Amplifier

Piezoelectric benders are 5mm long and 2mm wide. Because 1mm of the length is buried inside the silicon frame, the effective bending length of the piezo bender is set as 4mm. The modeling result of the 4mm bender is shown in Figure C-21, with the free deflection magnitude of 2.72μm.

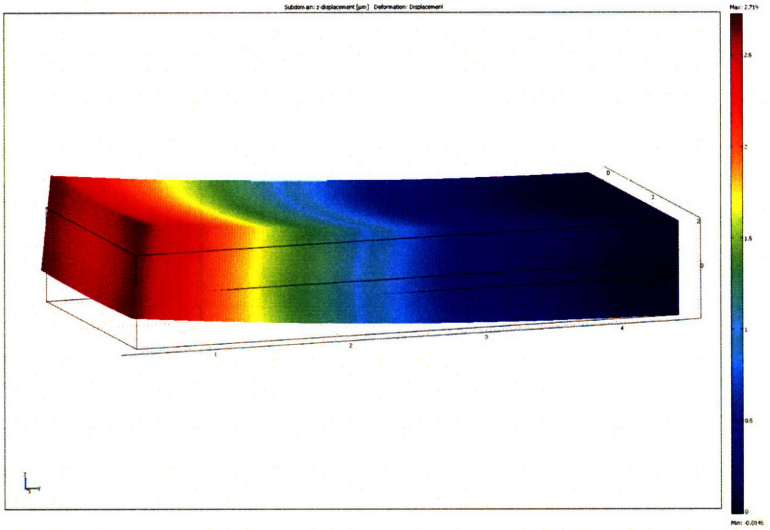

Figure C-21 Free deflection of 4mm PZT bender.

The modeling results of the micro-levers are summarized in Table 5-1 & 5-2, and plotted in Figure 5-5 & 5-6. The 12 individual results are plotted in Figure C-22 ~ Figure C-33. In each figure, the top plot is the endpoint deflection of the micro-lever; the bottom-left one is the deflection of the bender end; and the bottom-right one shows the von Mises stress of the micro-lever neck region.

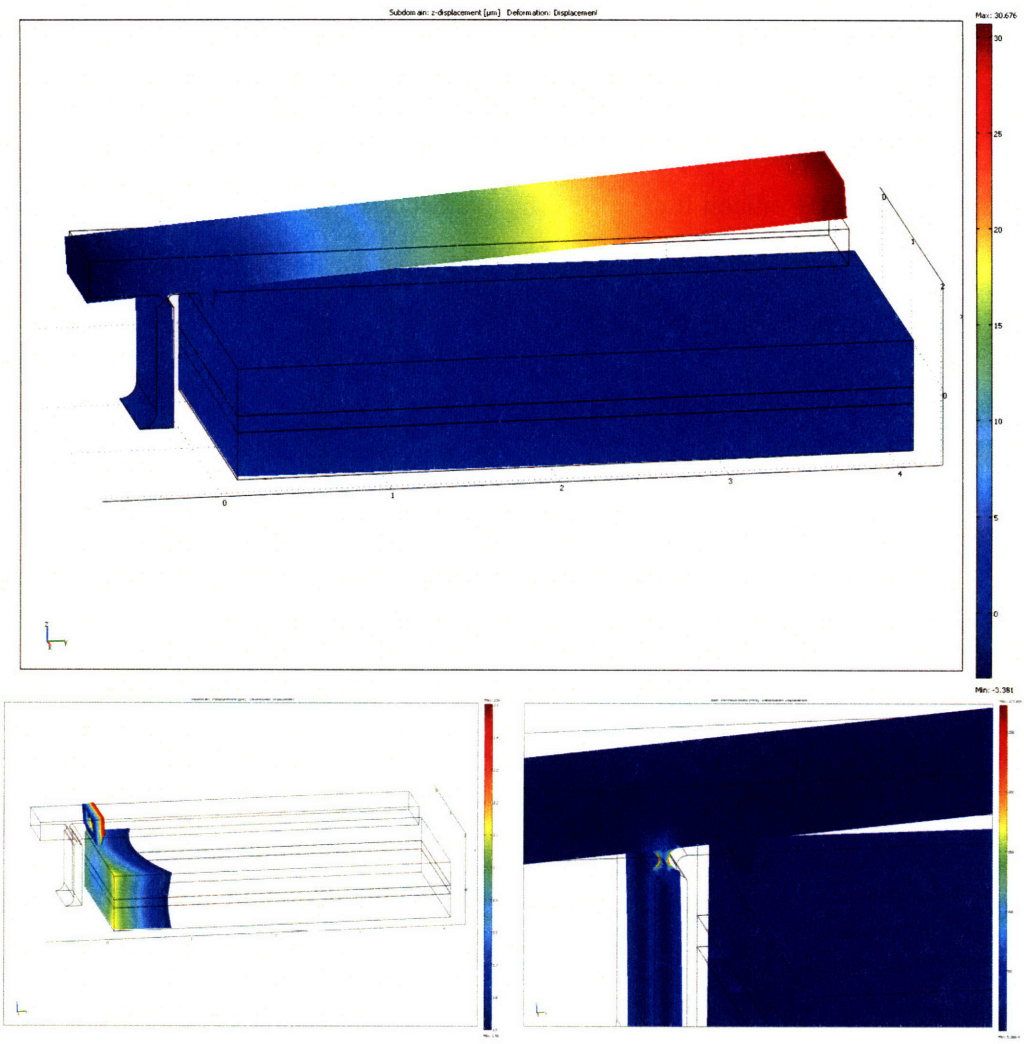

Figure C-22 Modeling results for the micro-lever with 30µm neck width and 150µm load point offset.

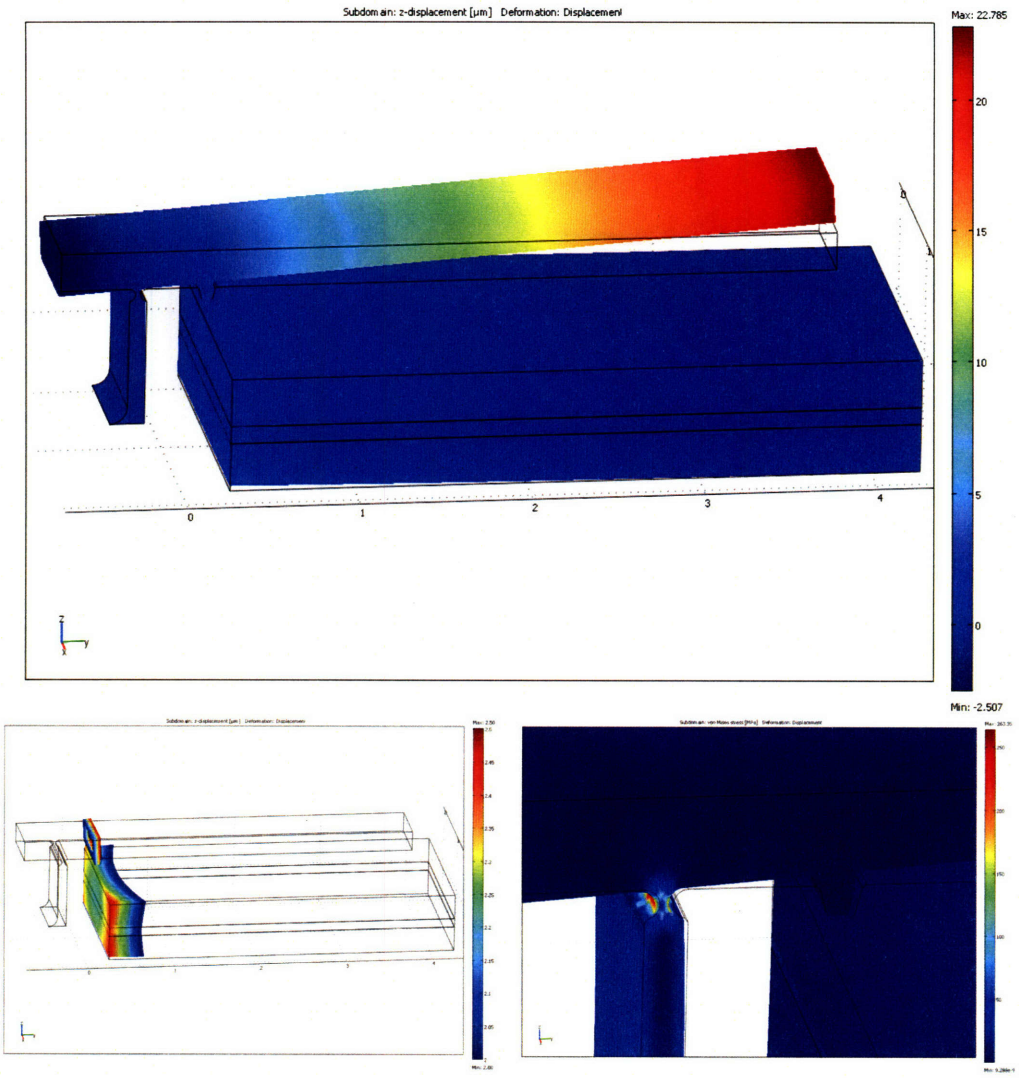

Figure C-23 Modeling results for the micro-lever with 30µm neck width and 300µm load point offset.

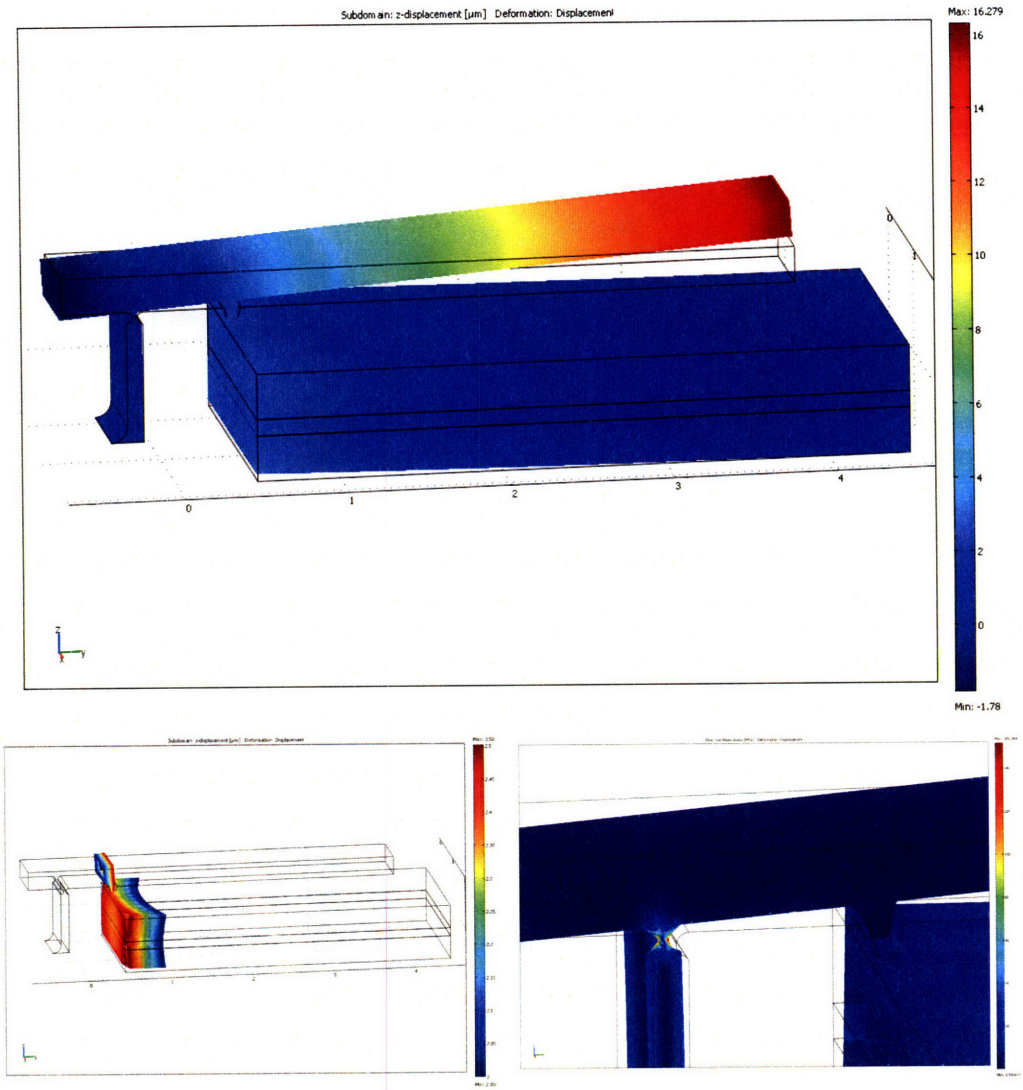

Figure C-24 Modeling results for the micro-lever with 30µm neck width and 500µm load point offset.

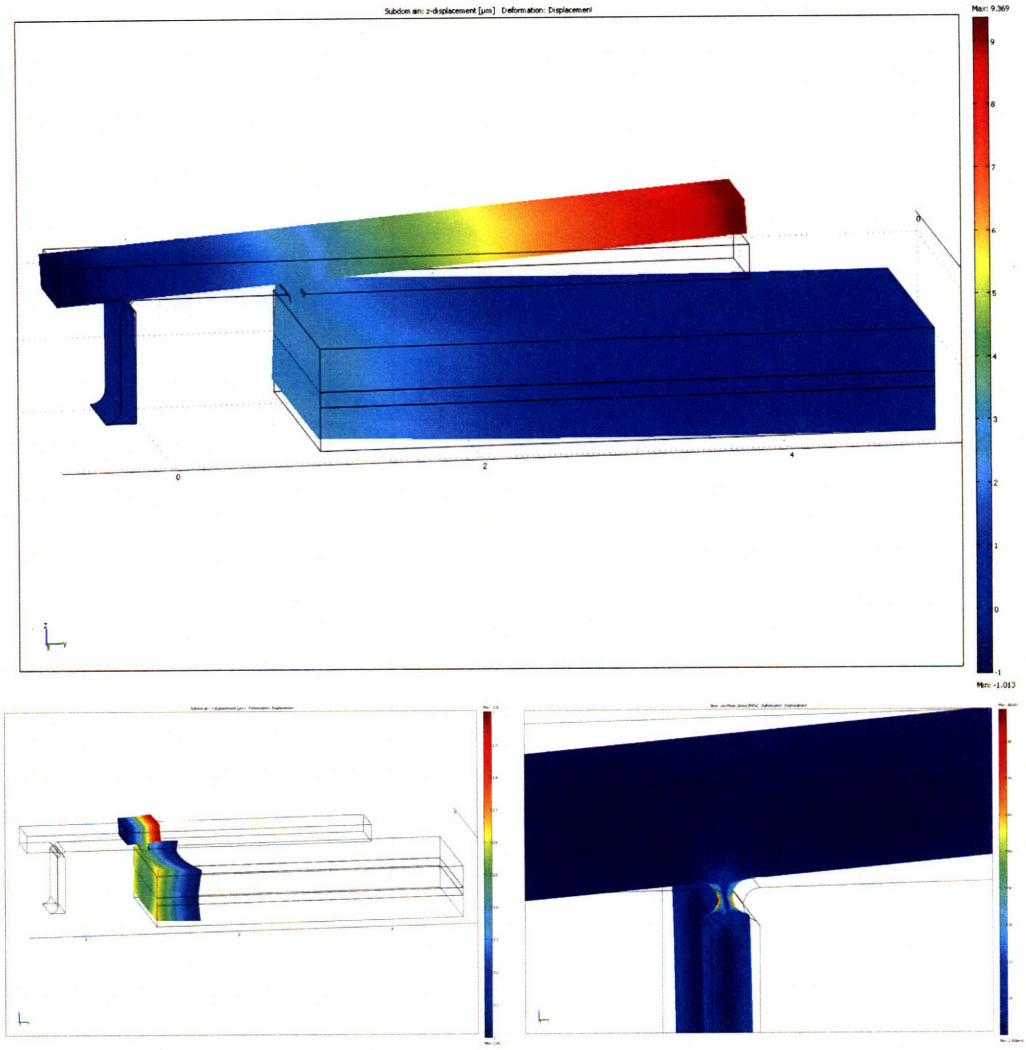

Figure C-25 Modeling results for the micro-lever with 30µm neck width and 1000µm load point offset.

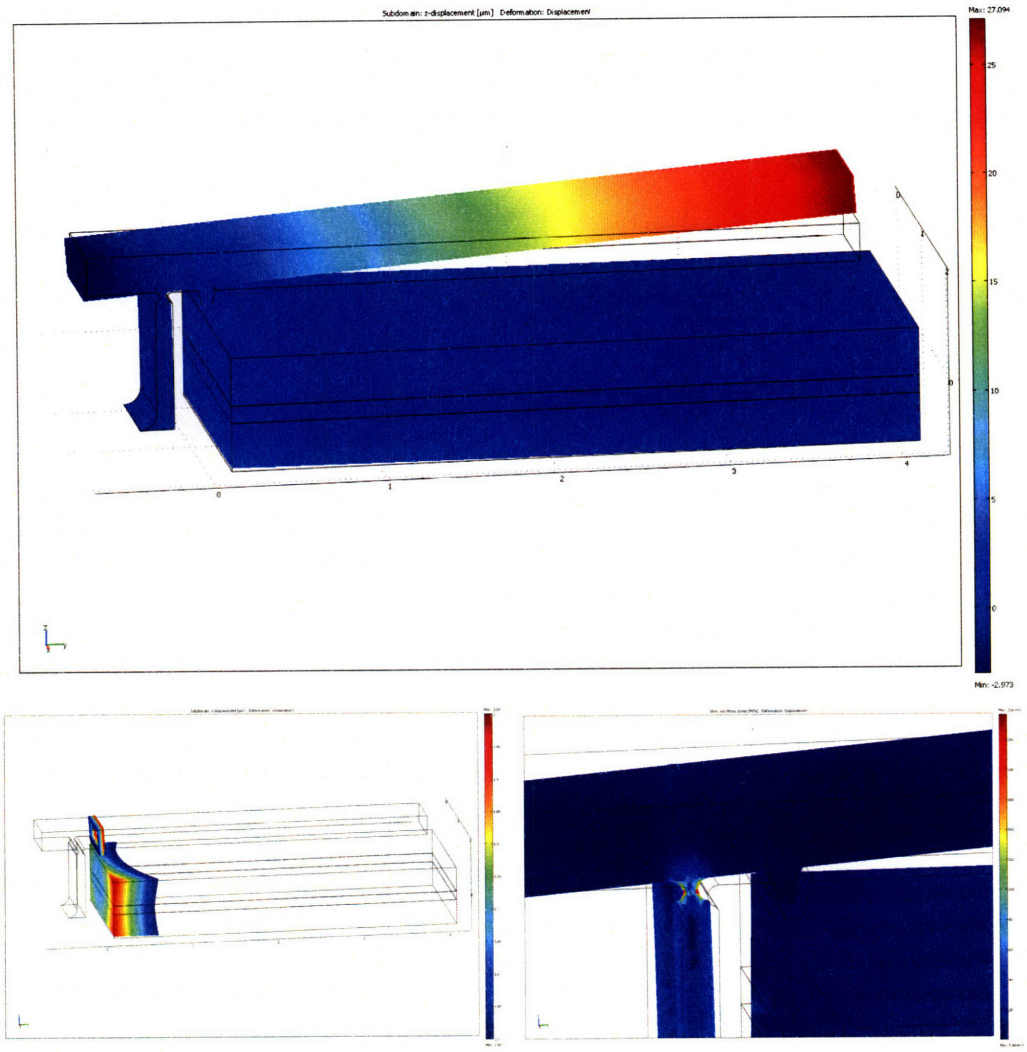

Figure C-26 Modeling results for the micro-lever with 40µm neck width and 150µm load point offset.

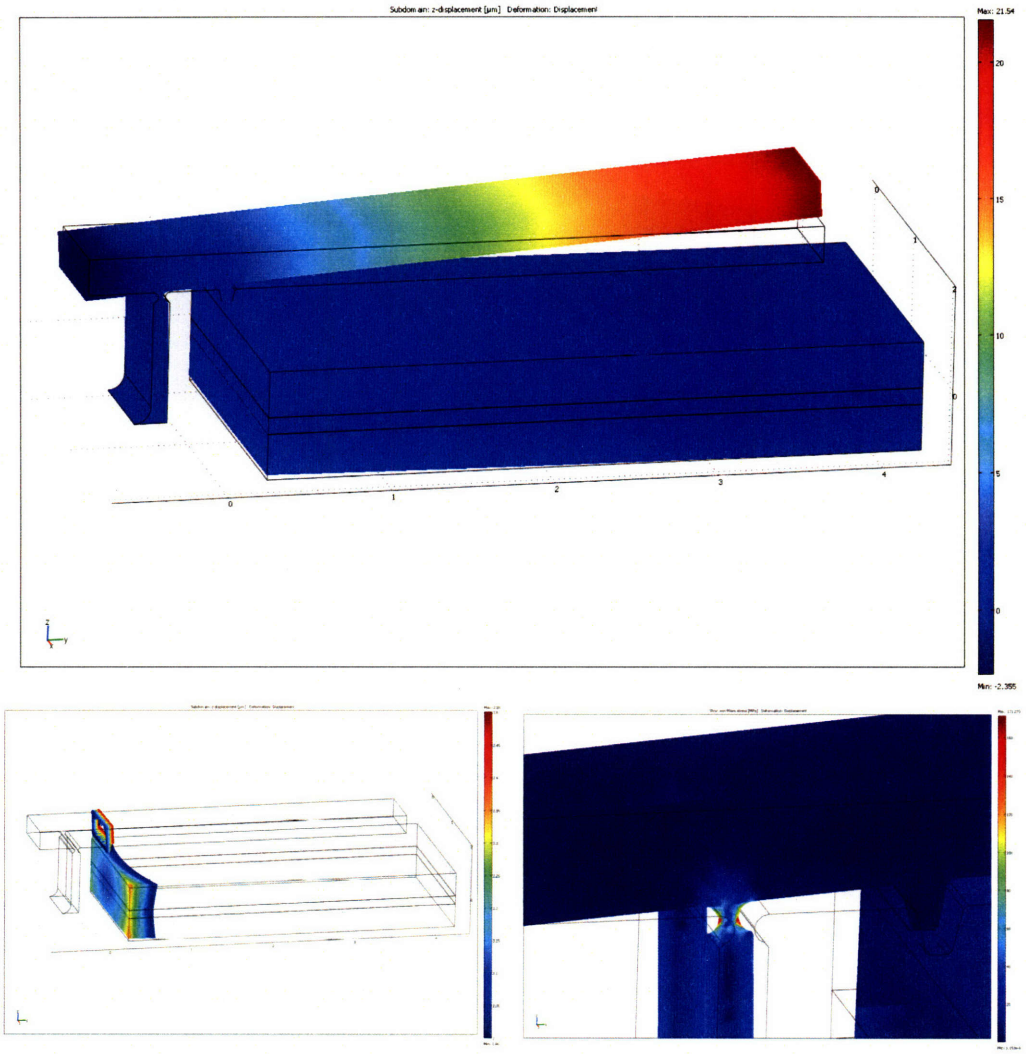

Figure C-27 Modeling results for the micro-lever with 40µm neck width and 300µm load point offset.

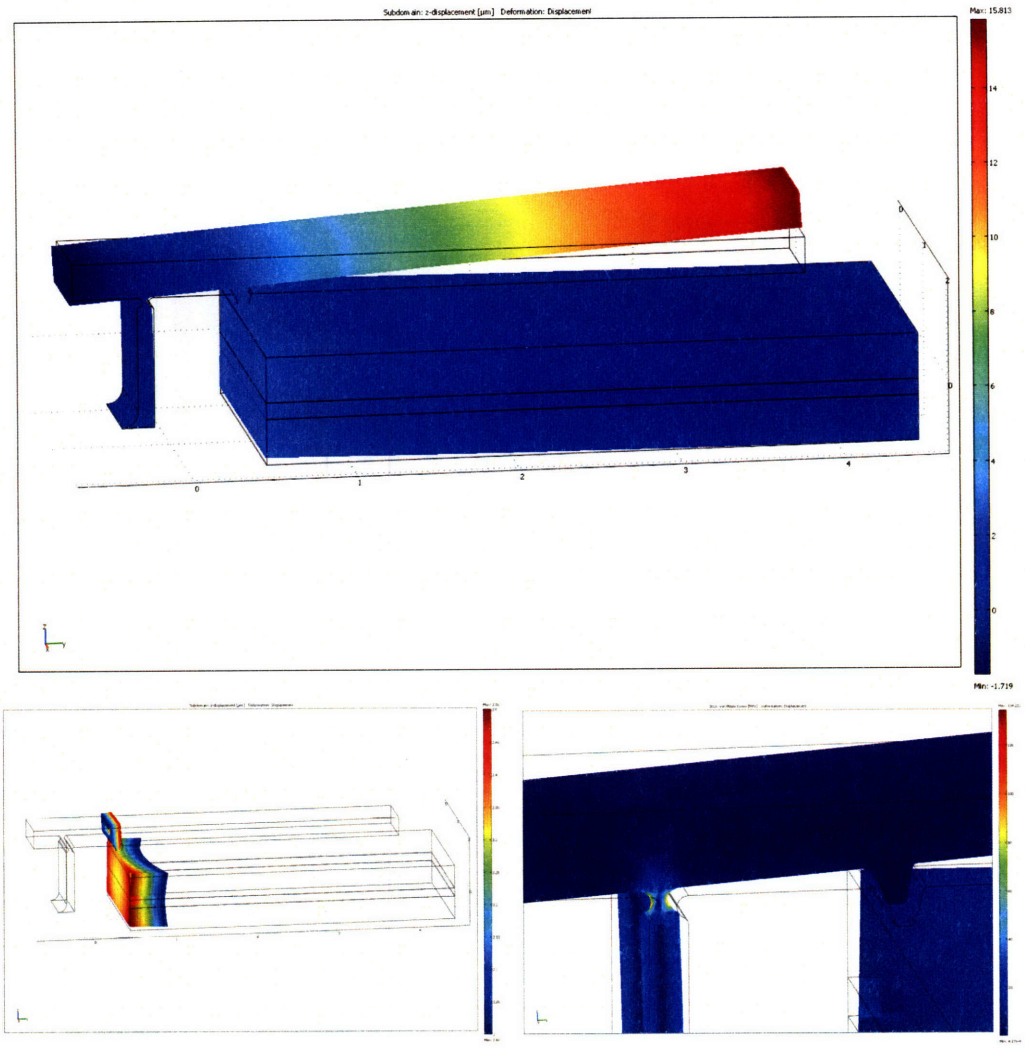

Figure C-28 Modeling results for the micro-lever with 40µm neck width and 500µm load point offset.

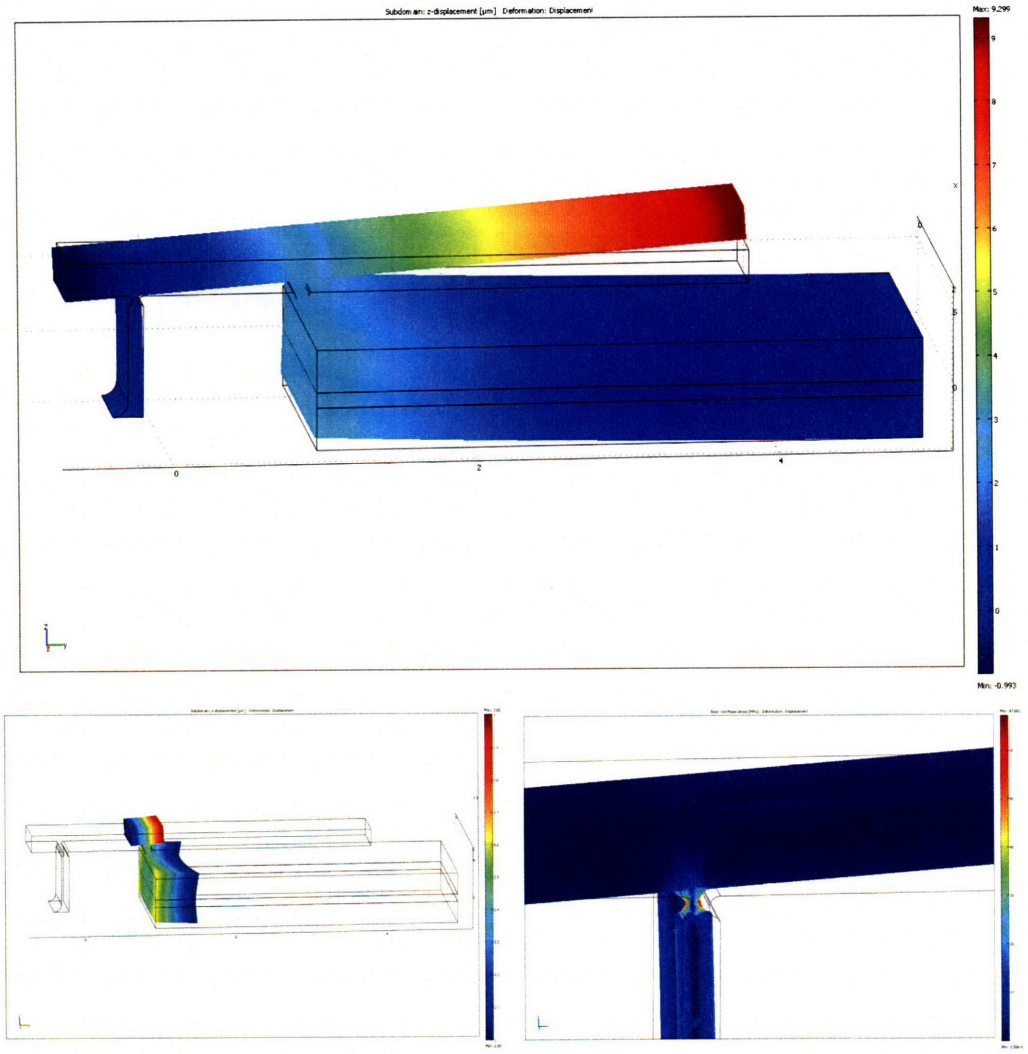

Figure C-29 Modeling results for the micro-lever with 40µm neck width and 1000µm load point offset.

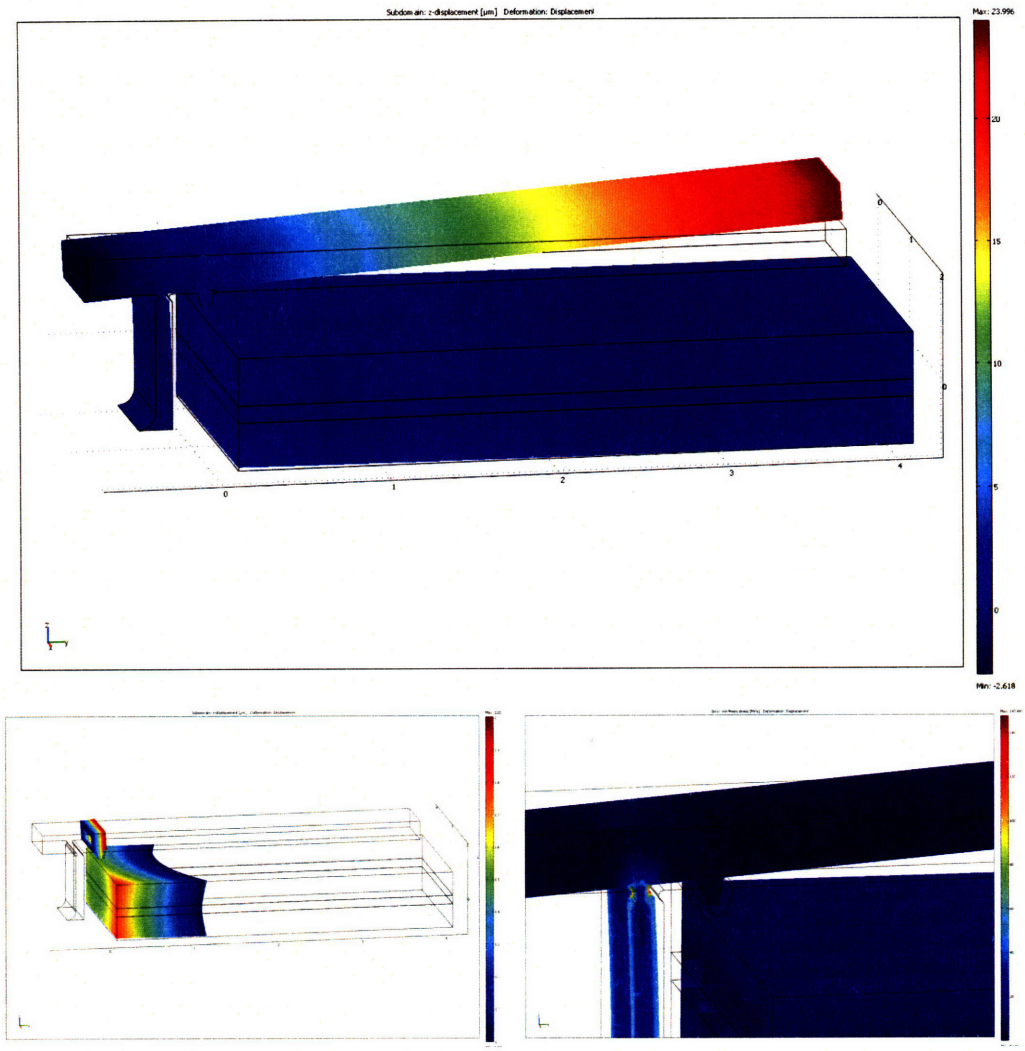

Figure C-30 Modeling results for the micro-lever with 60µm neck width and 150µm load point offset.

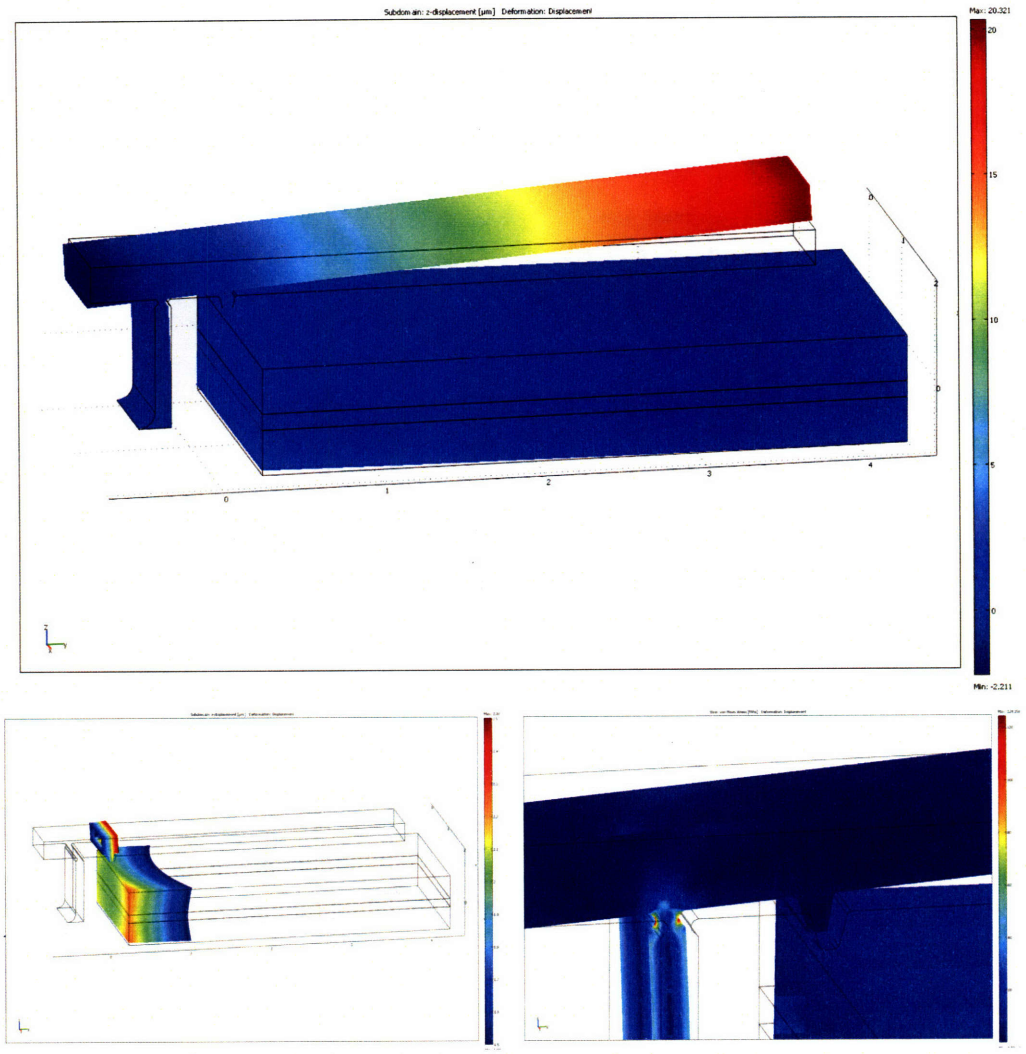

Figure C-31 Modeling results for the micro-lever with 60µm neck width and 300µm load point offset.

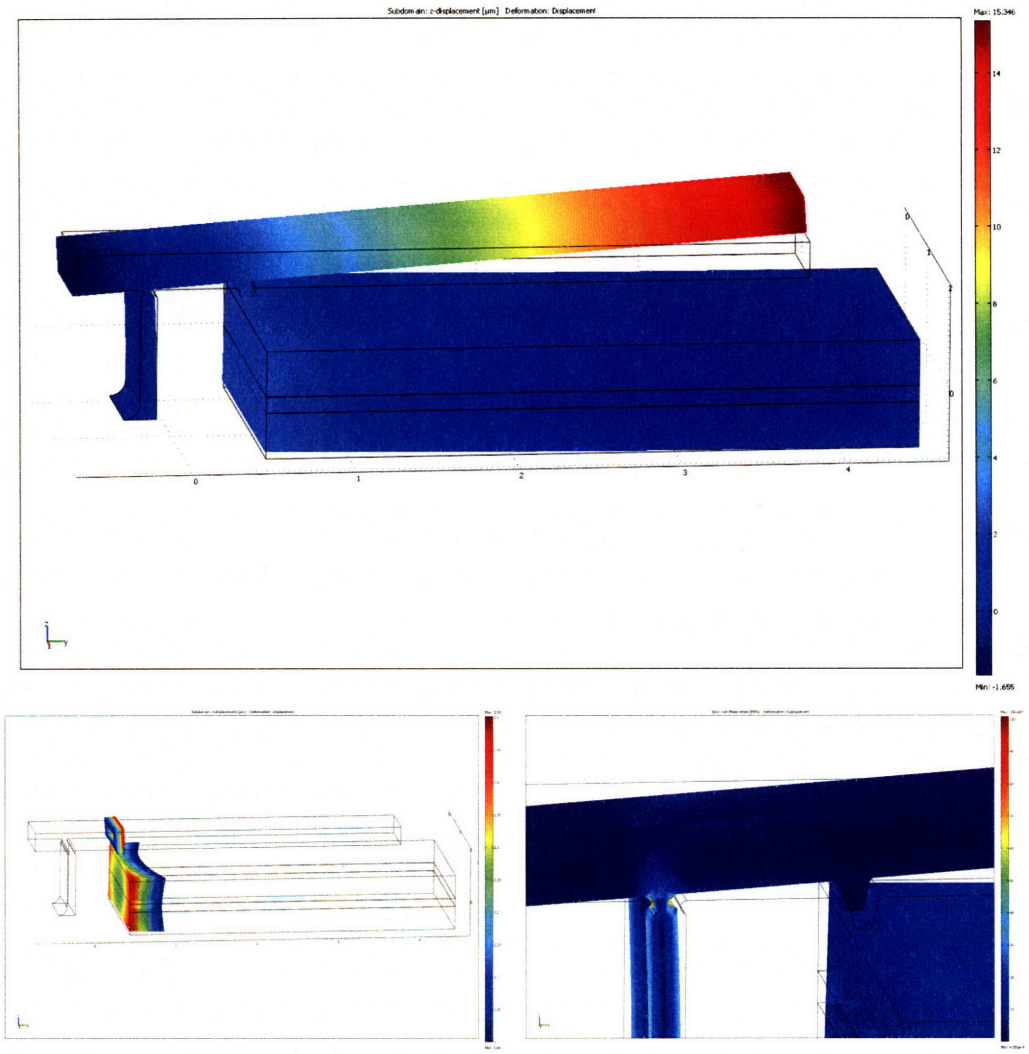

Figure C-32 Modeling results for the micro-lever with 60µm neck width and 500µm load point offset.

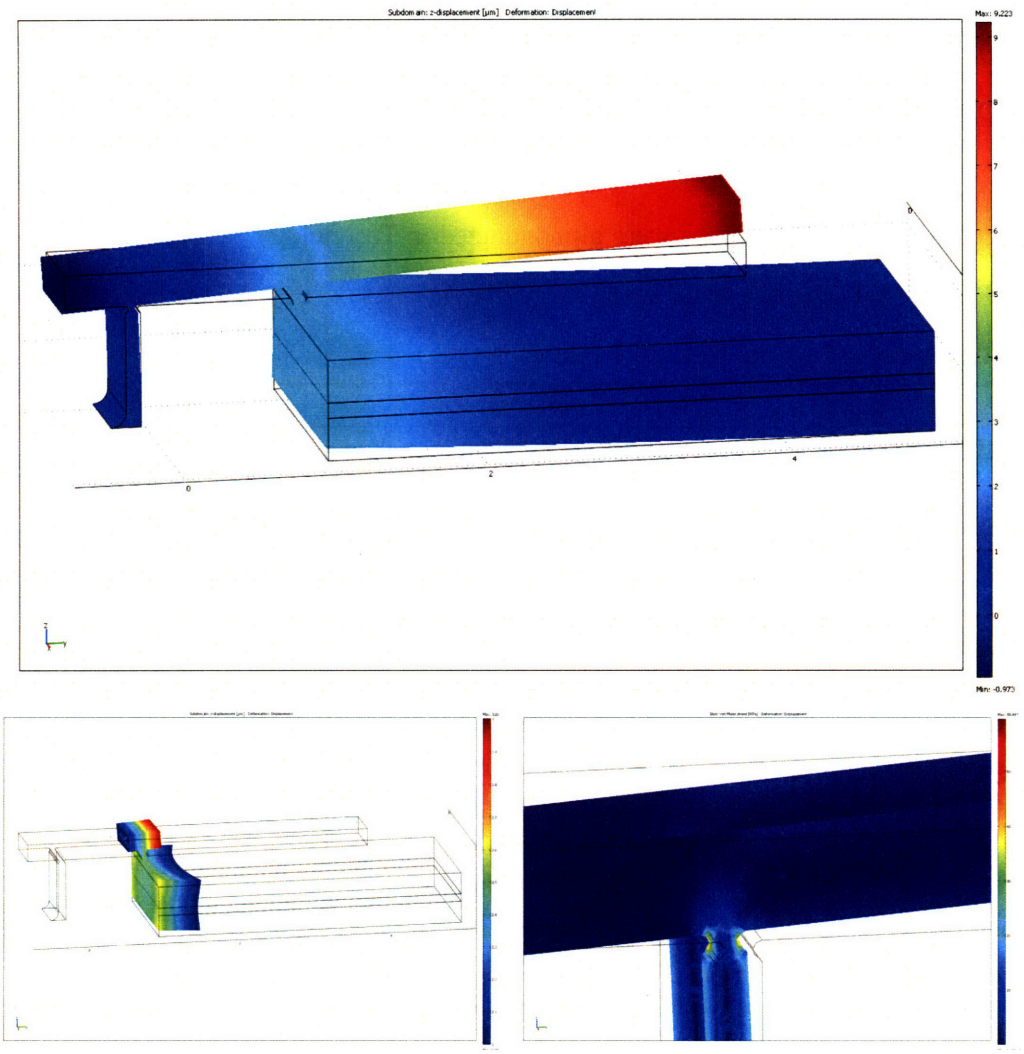

Figure C-33 Modeling results for the micro-lever with 60µm neck width and 1000µm load point offset.

Appendix D Process Flows

The silicon fabrications were all conducted in Technology Research Laboratory (TRL) of MIT Microsystems Technology Laboratories (MTL). All the recipes shown in the process flows are for TRL facilities.

Step	Description
Starting material	6" (100) single side polished silicon wafer
Photo Lithography	
HMDS	HMDS vapor deposition #3
Spin Coat Photoresist #1	Dispense: static for 15 seconds
(AZ 4620, thick)	Spread: 1500 rpm for 6 seconds
	Spin: 1500 rpm for 60 seconds
Pre-bake	At 90°C for 20 minutes
Spin Coat Photoresist #2	Dispense: 750 rpm for 15 seconds
(AZ 4620, thick)	Spread: 750 rpm for 6 seconds
	Spin: 1500 rpm for 60 seconds
Pre-bake	At 90°C for 60 minutes
Exposure (Mask #1)	4 intervals, each with 15 sec. exposure and 15 sec. waiting
Develop	For no more than 4 min.
Post-bake	At 90°C for 30 minutes
Mounting	
Staring materials	6" quartz wafer
Spin Coat Photoresist	1500 rpm for bulls-eye pattern
(AZ 4620, thick)	
Mount	Mount the silicon wafer onto the quartz wafer
Bake	At 90°C for 10~20 min
Etch	Etch through the wafer with STS-2. Recipe: ole3
Post-treatment	
Release	Release the silicon wafer off quartz wafer in acetone
Rinse	Rinse in isopropanol then in DI water
Ashing	For at least one hour in TRL asher
Surface Passivation	
Clean	Piranha clean in TRL Acidhood-1
Oxidation	Thermal oxidation in tube B-1

The process flow can be improved by growing a 0.5μm thick oxide layer at the very beginning:

Step	Description
Starting material	6" (100) single side polished silicon wafer
Oxidation	
Clean	RCA clean
Oxidation	Thermal oxidation in tube A-2
Photo Lithography	
HMDS	HMDS vapor deposition #3
Spin Coat Photoresist #1	Dispense: static for 15 seconds
(AZ 4620, thick)	Spread: 1500 rpm for 6 seconds
	Spin: 1500 rpm for 60 seconds
Pre-bake	At 90°C for 20 minutes
Spin Coat Photoresist #2	Dispense: 750 rpm for 15 seconds
(AZ 4620, thick)	Spread: 750 rpm for 6 seconds
	Spin: 1500 rpm for 60 seconds
Pre-bake	At 90°C for 60 minutes
Exposure (Mask #1)	4 intervals, each with 15 sec. exposure and 15 sec. waiting
Develop	For no more than 4 min.
Post-bake	At 90°C for 30 minutes
Oxide Etch	BOE (7:1) in TRL Acid Hood #1
Mounting	
Staring materials	6" quartz wafer
Spin Coat Photoresist	1500 rpm for bulls-eye pattern
(AZ 4620, thick)	
Mount	Mount the silicon wafer onto the quartz wafer
Bake	At 90°C for 10~20 min
Silicon Etch	Etch through the silicon wafer with STS-2 (recipe: ole3)
Post-treatment	
Release	Release the silicon wafer off quartz wafer in acetone
Rinse	Rinse in isopropanol then in DI water
Ashing	For at least one hour in TRL asher
Surface Passivation	
Clean	Piranha clean in TRL Acid Hood #1
Oxidation	Thermal oxidation in tube B-1

Appendix E Mask Layouts

All the devices previously shown were all prepared by single-mask fabrication. For delicate features, "halo" structures are adopted to improve plasma etch homogeneity.

(1) Single rings (Section 3.2)

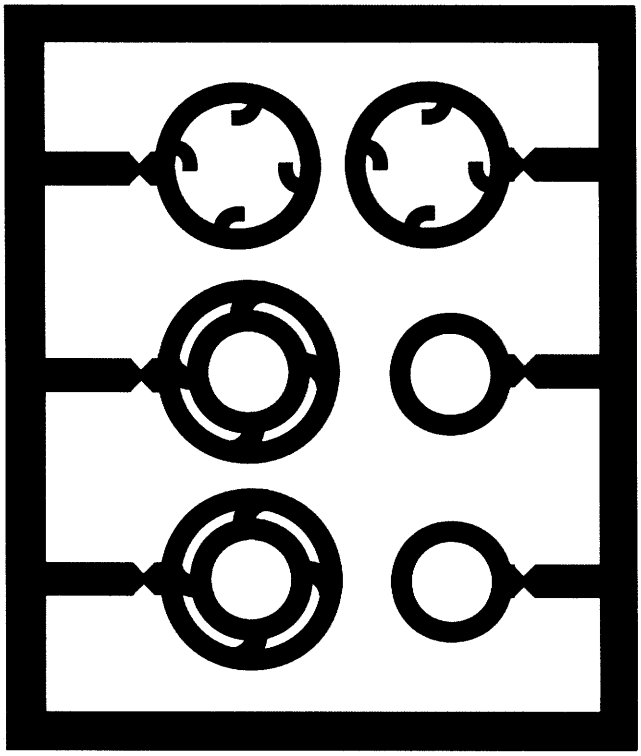

(2) 2D Assembly (Section 3.3)

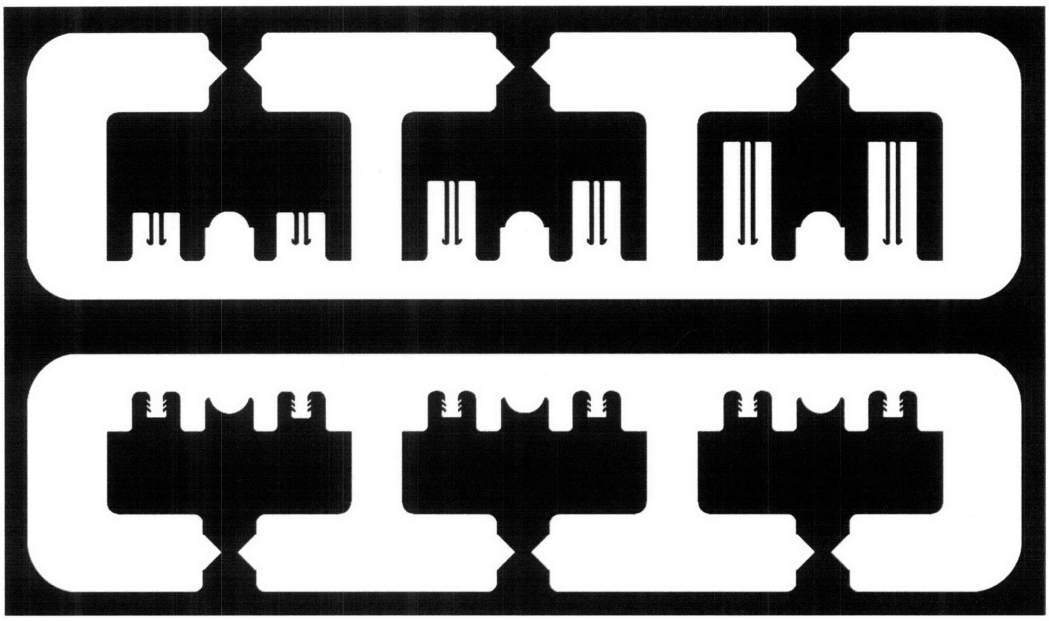

(3) 3D Assembly (Section 3.3)

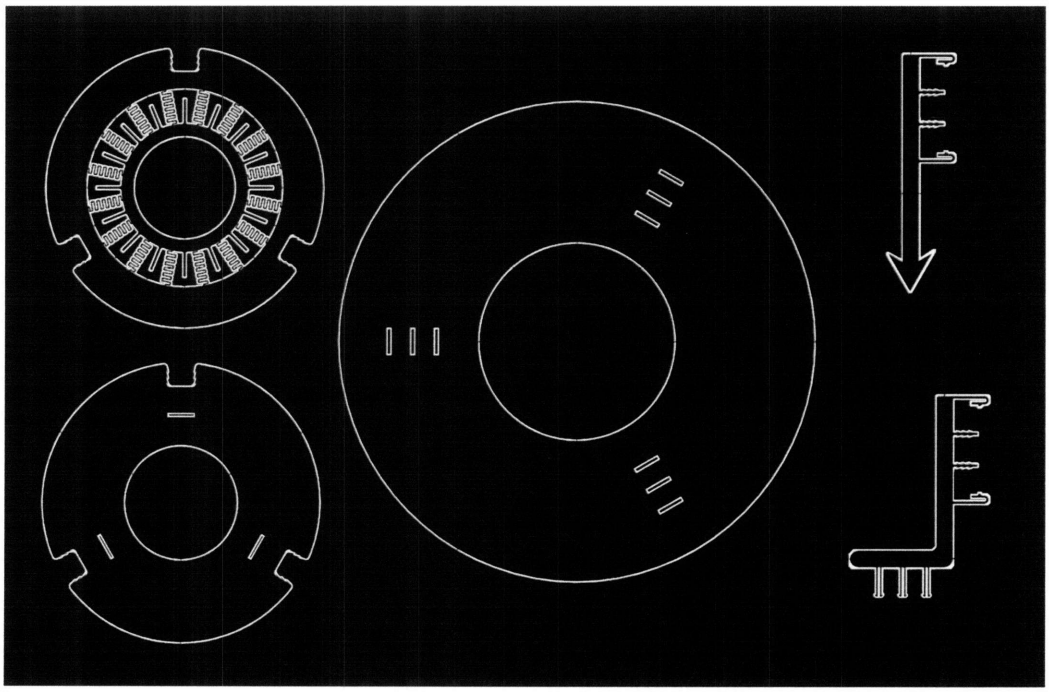

(4) Shackles (Section 3.4)

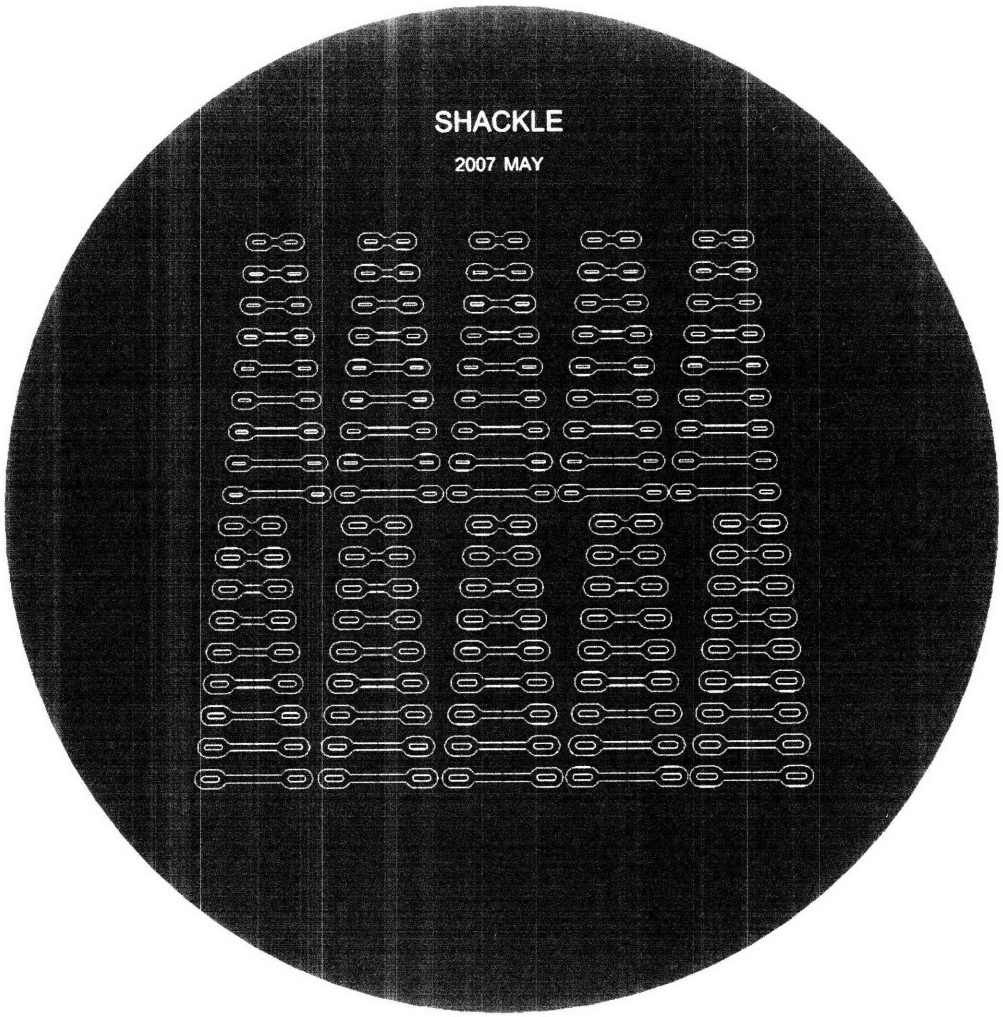

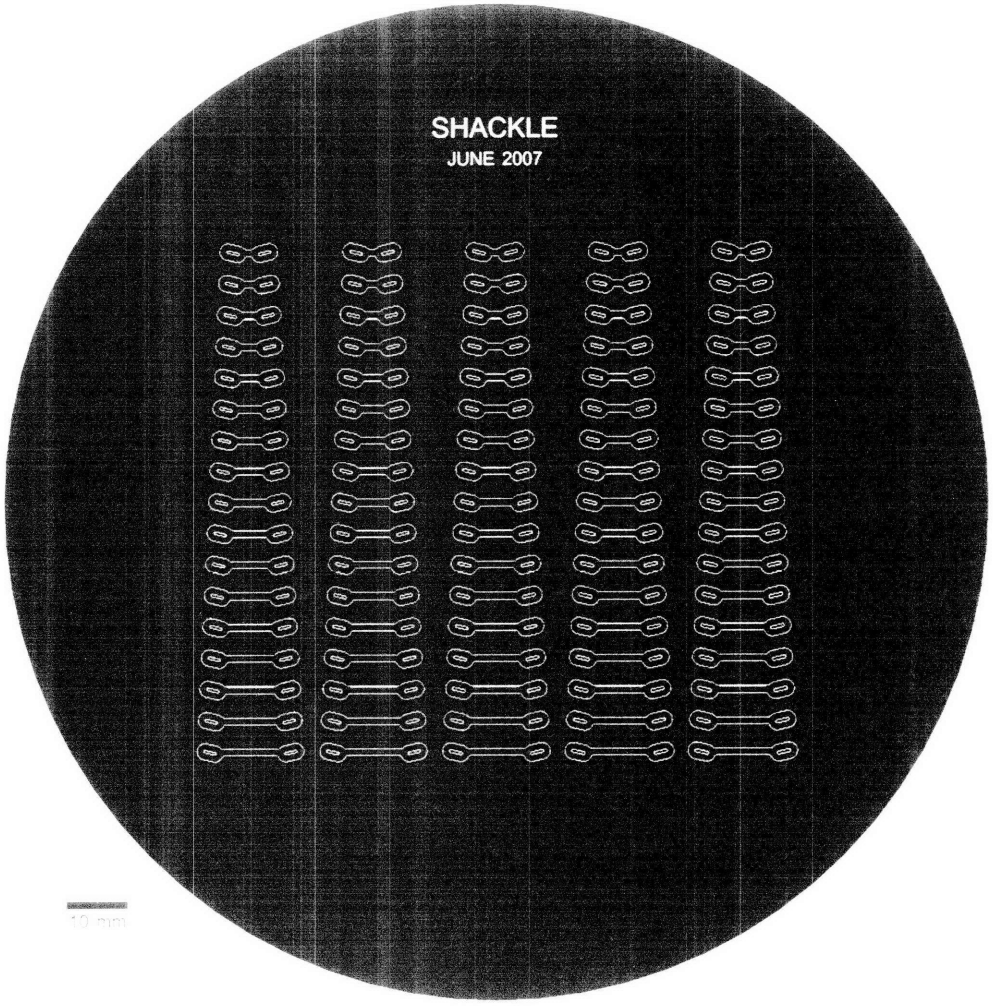
SHACKLE
JUNE 2007
10 mm

(5) Shackles (Section 4.3)

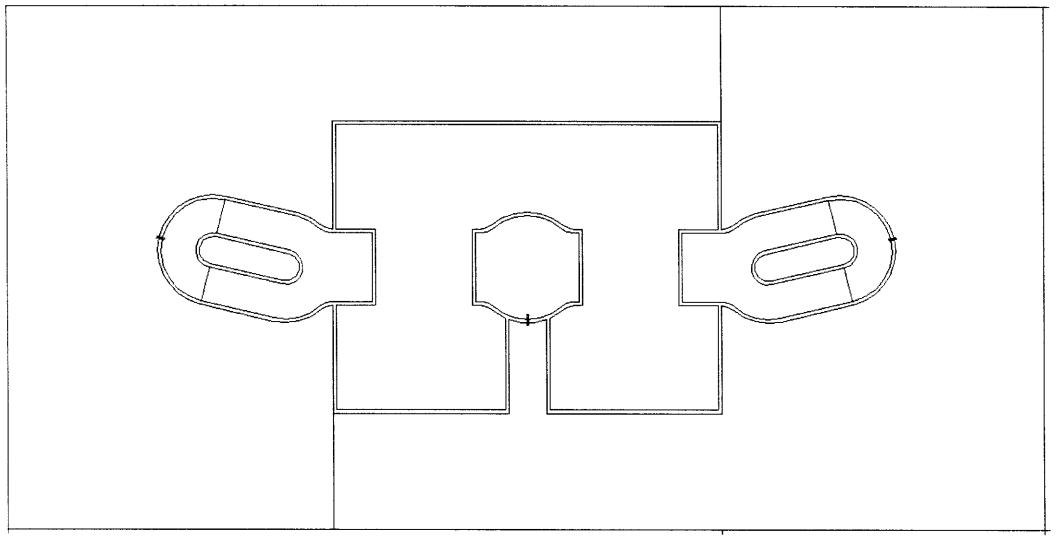

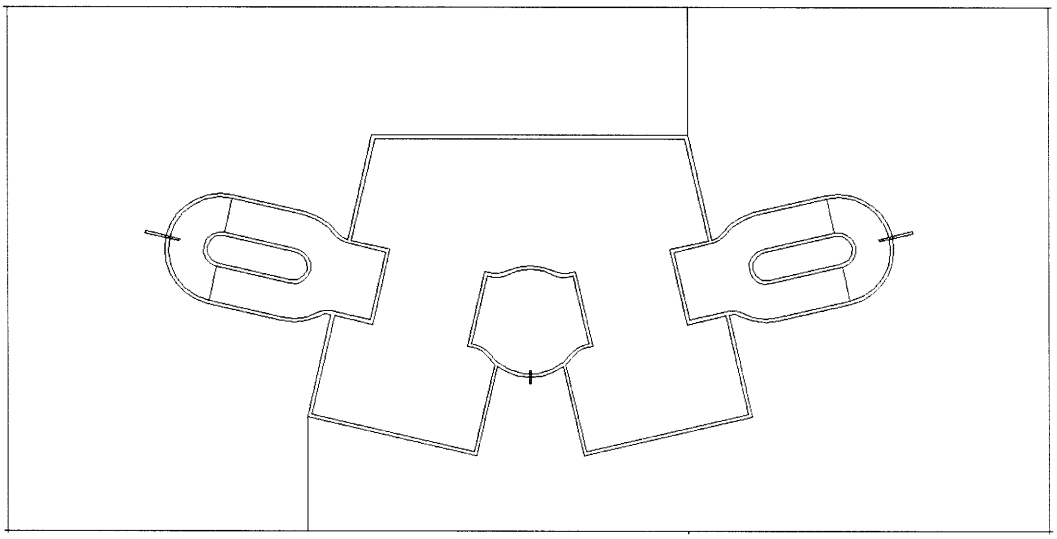

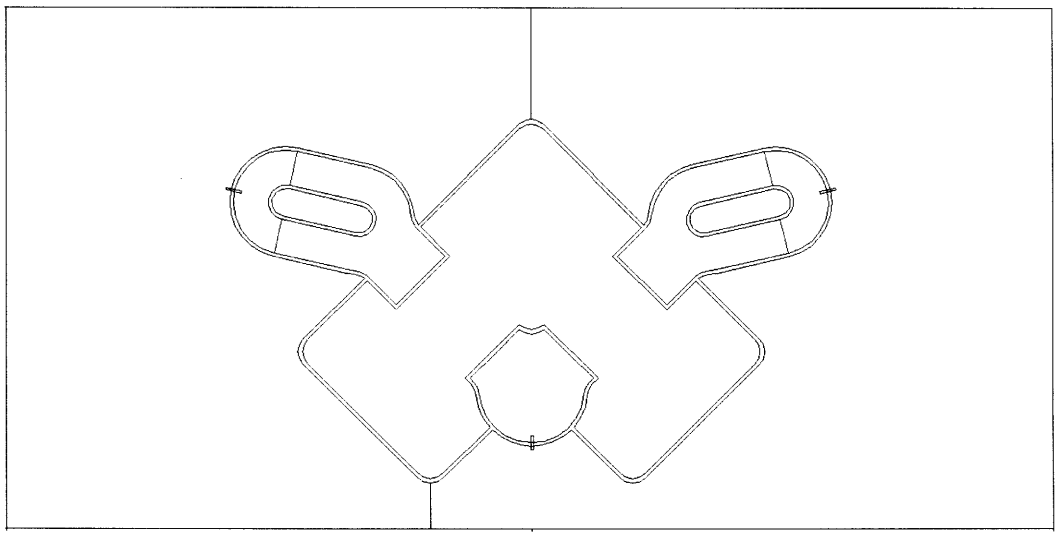

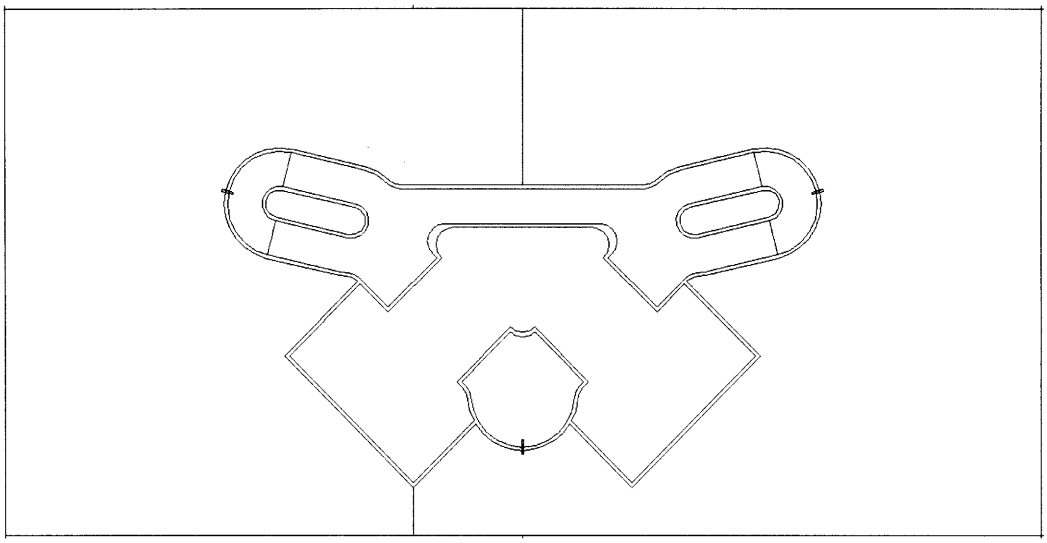

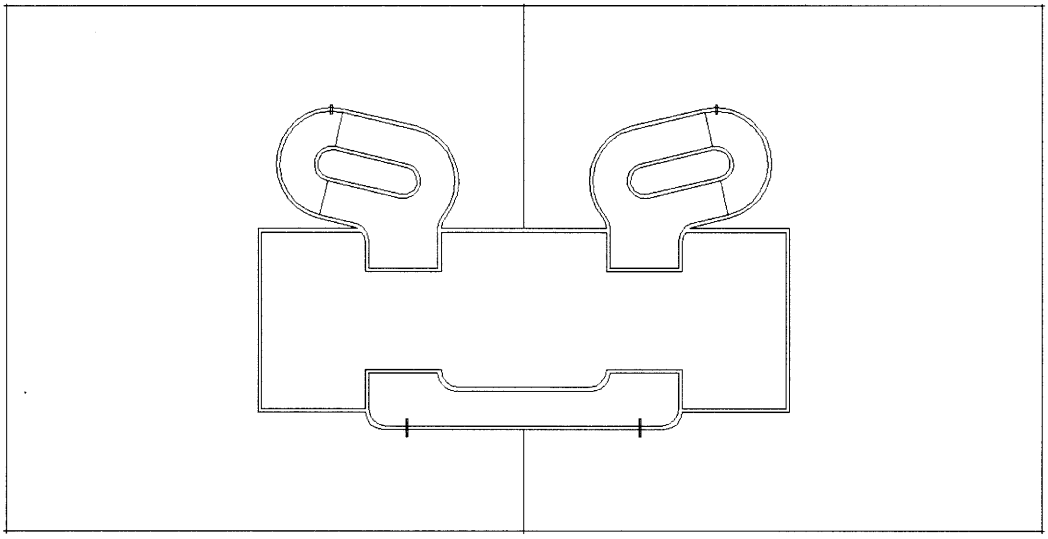

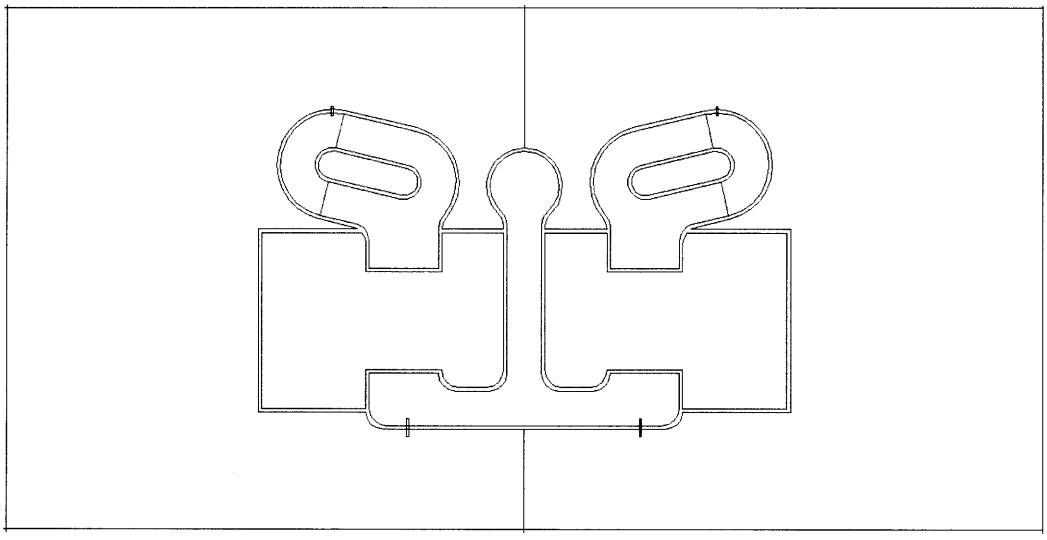

(5) Shackles (Section 4.4)

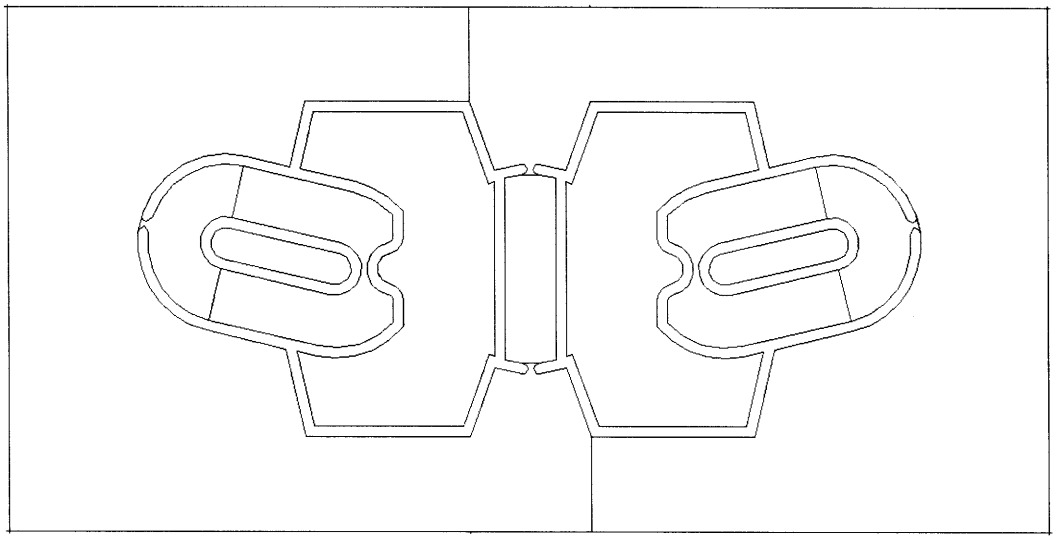

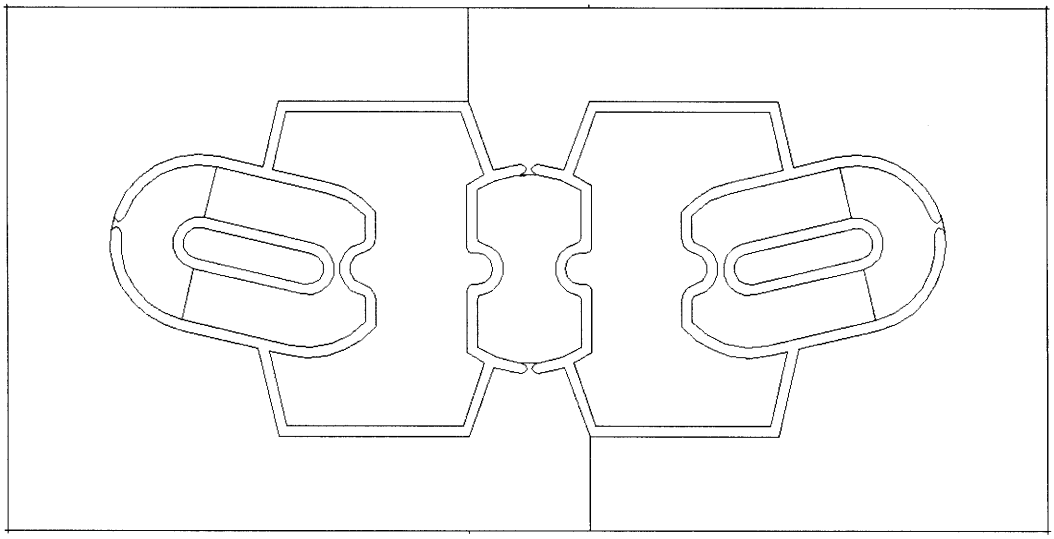

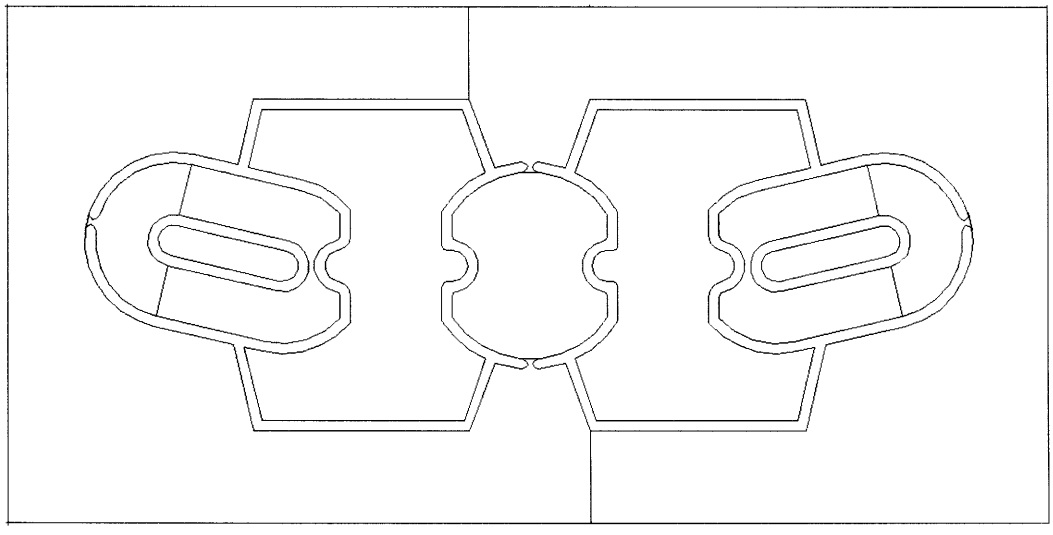

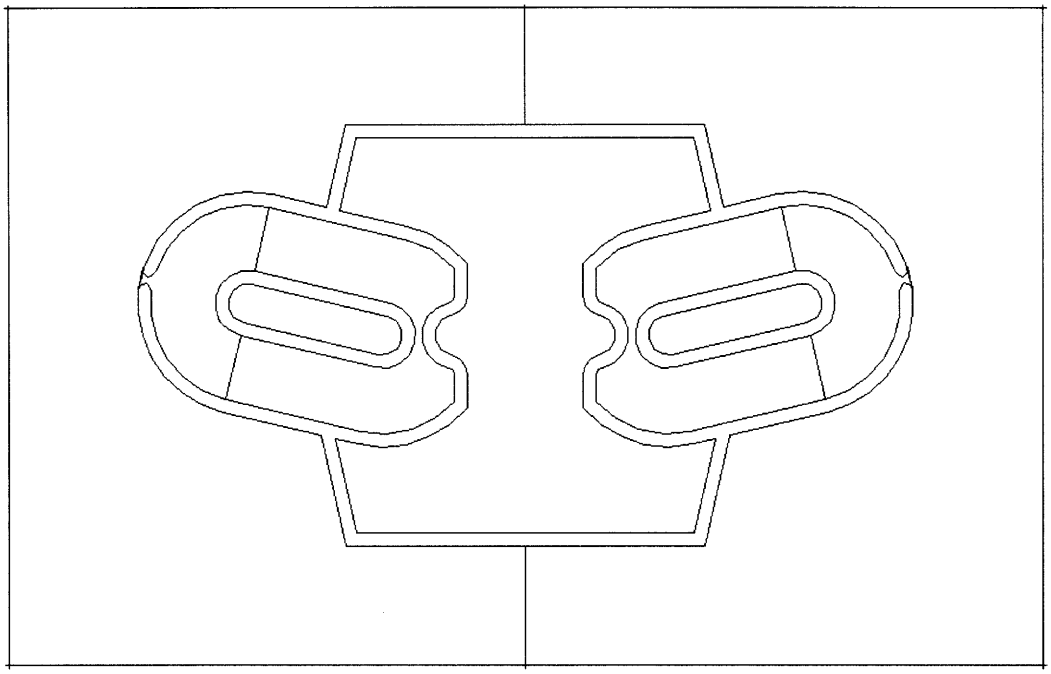

(6) Micro-levers

a. Neck width 30μm, load point offset 150μm

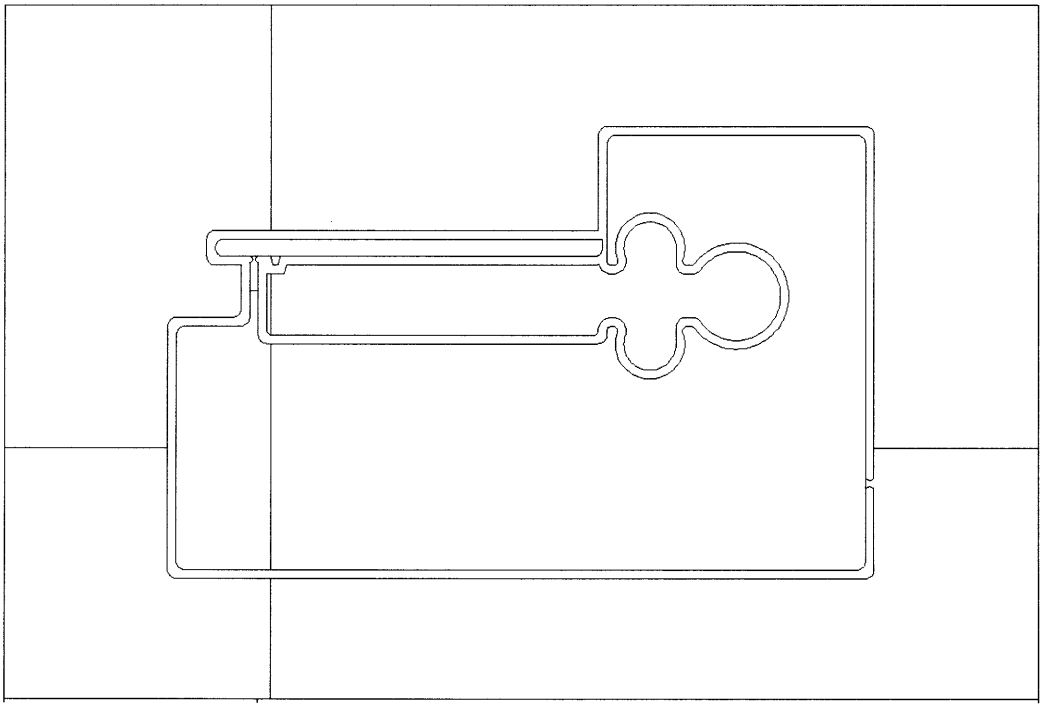

b. Neck width 40μm, load point offset 300μm

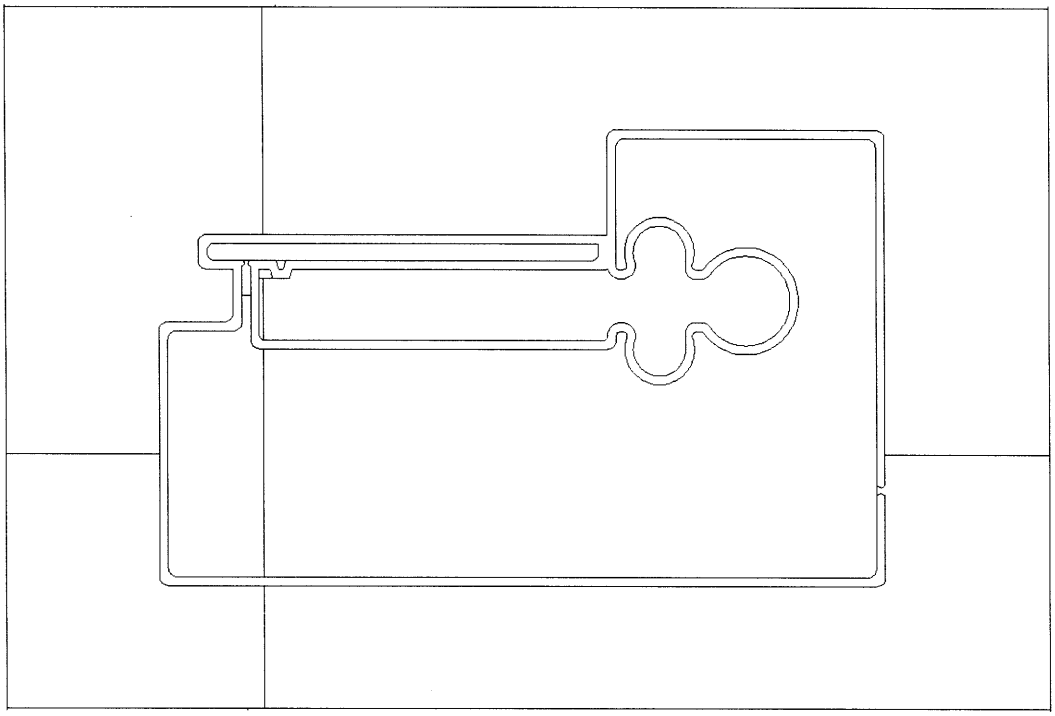

c. Neck width 60μm, load point offset 500μm

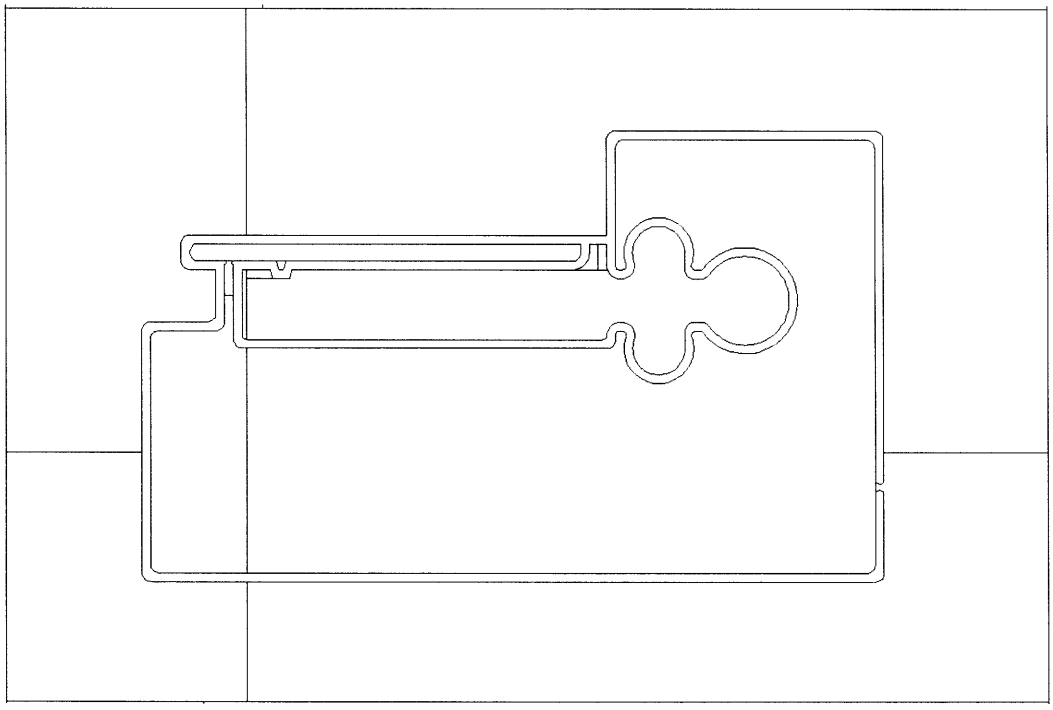

d. Neck width 30μm, load point offset 1000μm

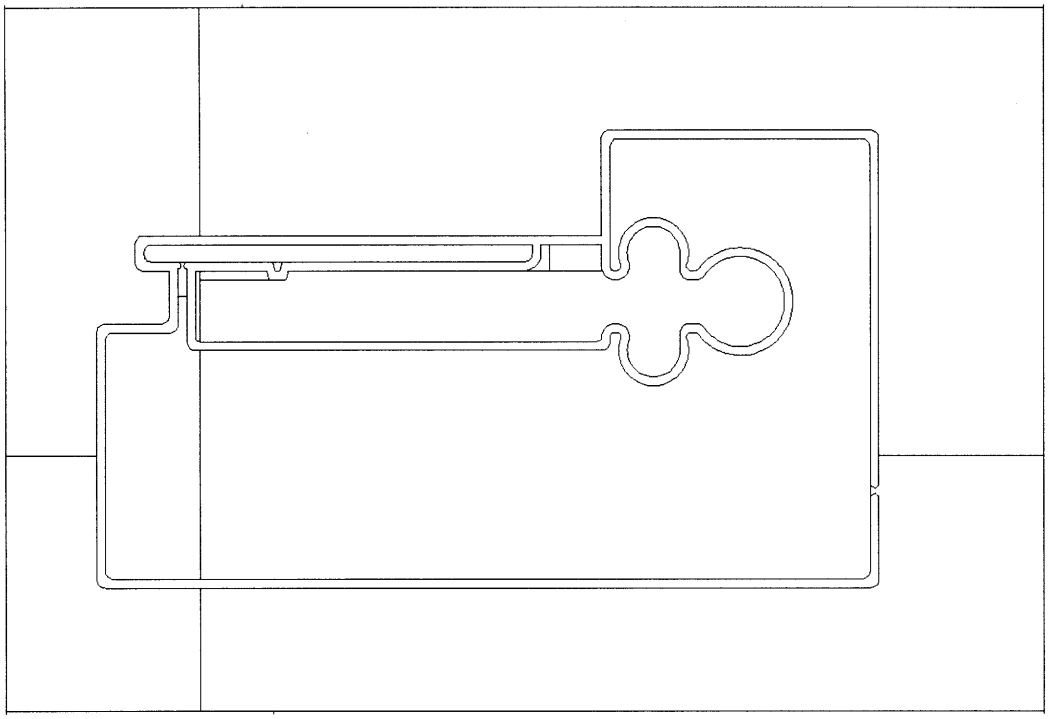

(7) Heat Sinks (Appendix B)

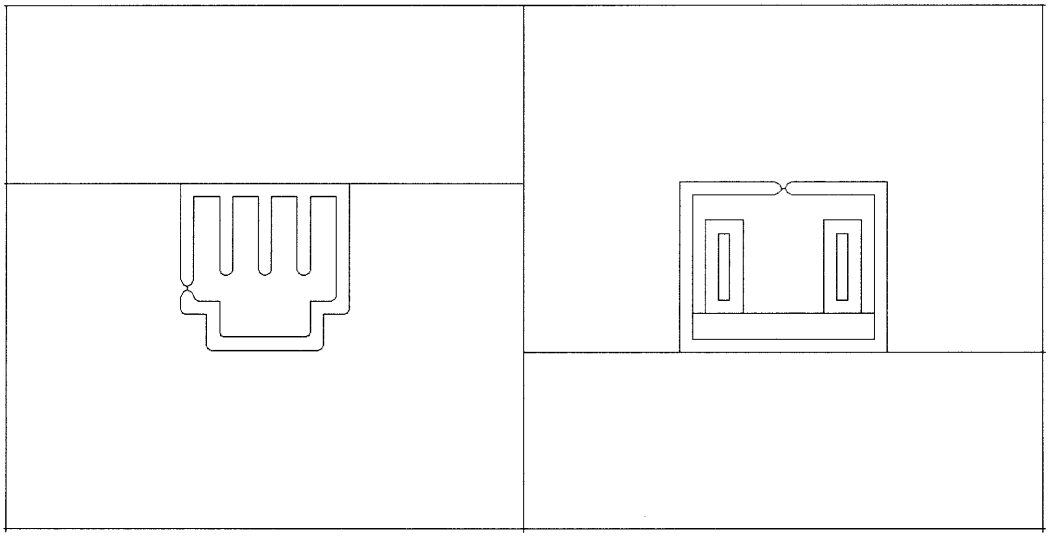

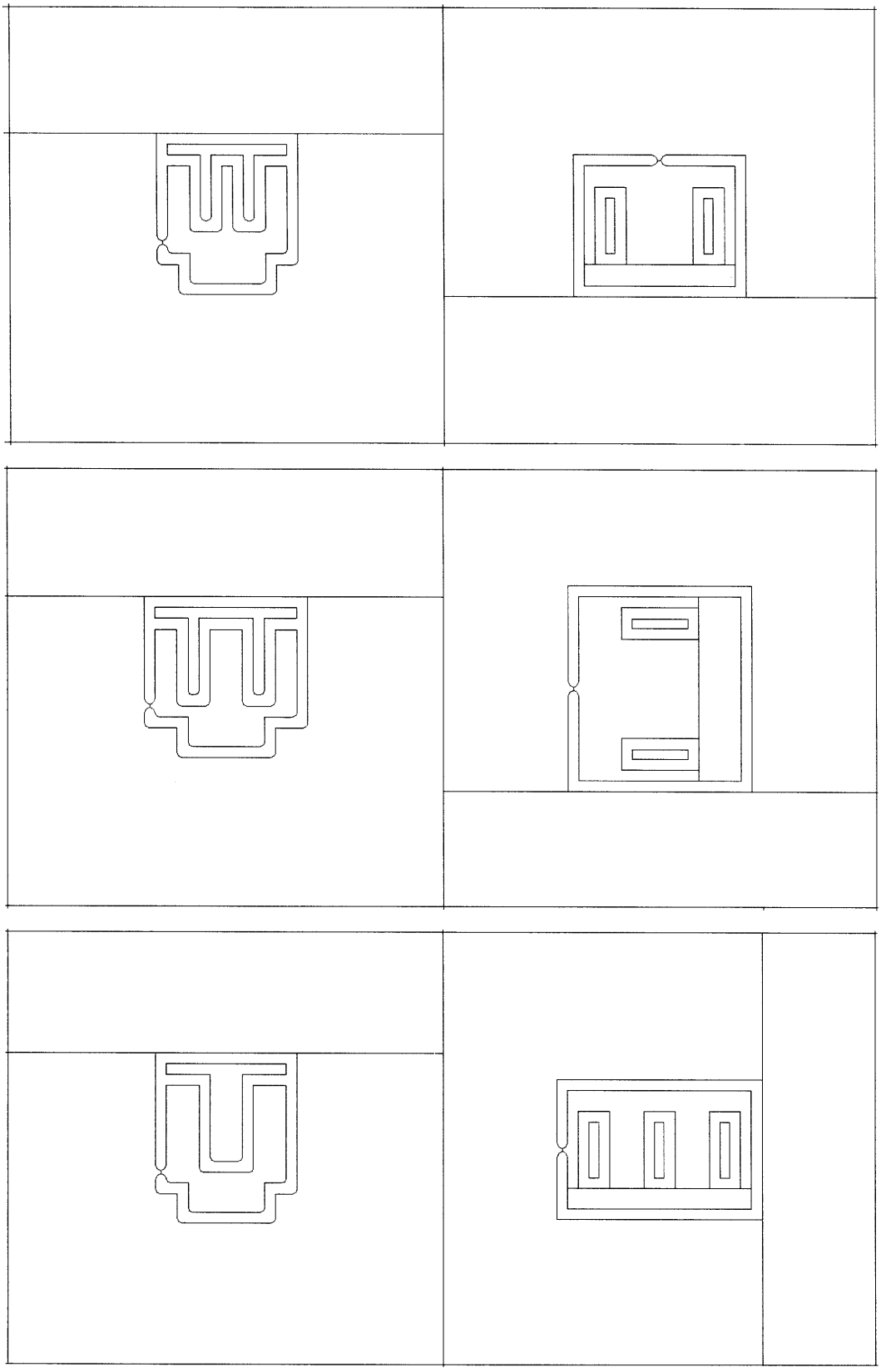

References

[1] M. Gewecke, "Antennae: another wind-sensitive receptor in locusts," *Nature*, vol. 225, no. 5239, pp. 1263-1264, Mar. 1970.

[2] S.P. Sane, A. Dieudonné, M.A. Willis, and T.L. Daniel, "Antennal mechano-sensors mediate flight control in moths," *Science*, vol. 315, pp. 863-866, Feb. 2007.

[3] C. Liu, *Foundations of MEMS*, Pearson Education, Upper Saddle River, NJ, 2006.

[4] M. Tabib-Azar, *Microactuators*, Kluwer Academic Publishers, Boston, 1998.

[5] H. Janocha, *Actuators*, Springer-Verlag Berlin Heidelberg, 2004.

[6] L.-S. Fan, Y.-C. Tai, and R.S. Muller, "IC-processed electrostatic micro-motors," *IEEE International Electronic Device Meeting*, Dec. 1988.

[7] S.C. Jacobsen, R.H. Price, J.E. Wood, T.H. Rytting, and M. Rafaelof, "A design overview of an eccentric- motion electrostatic micromotor (the wobble motor)", *Sensors and Actuators*, 20 (1), pp. 1-16, 1989.

[8] W. Trimmer and R. Jebens, "Harmonic electrostatic motors", *Sensors and Actuators*, 20 (1), pp. 17-24, 1989.

[9] L.G. Frechette, S.F. Nagle, R. Ghodssi, S.D. Umans, M.A. Schmidt, and J.H. Lang, "An electrostatic induction micromotor supported on gas-lubricated bearings", *The 14th IEEE International Conference on Micro Electro Mechanical Systems*, pp. 290-293, 2001.

[10] C. Livermore, A.R. Forte, T. Lyszczarz, S.D. Umans, A.A. Ayon, J.H Lang, "A high-power MEMS electric induction motor", *Journal of Microelectromechanical Systems*, 13 (3), pp. 465-471, 2004.

[11] W.C. Tang, T.H. Nguyen, M.W. Judy, R.T. Howe, "Electrostatic-comb drive of lateral polysilicon resonators", *Sensors and Actuators A*, 21(1-3), pp. 328-331, 1990.

[12] S. Lee, S. Park, and D. Cho, "The surface/bulk micromachining (SBM) process: a new method for fabricating released MEMS in single crystal silicon", *Journal of Microelectromechanical Systems*, 8(4), pp. 409-416, 1999.

[13] M. Ataka, A. Omodaka, M. Takeshima, and H. Fujita, "Fabrication and operation of polyimide bimorph actuators for a ciliary motion system", *Journal of Micro- electromechanical Systems*, 2(4), 1993.

[14] L. Que, J.-S. Park, and Y.B. Gianchandani, "Bent-beam electrothermal actuators—part I: single beam and cascaded devices", *Journal of Microelectro-mechanical Systems*, 10(2), pp. 247-254, 2001.

[15] J.H. Comtois, and V.M. Bright, "Applications for surface-micromachined polysilicon thermal actuators and arrays", *Sensors and Actuators A*, 58, pp. 19-25, 1997.

[16] J.T. Butler, V.M. Bright, and W.D. Cowan, "Average power control and positioning of polysilicon thermal actuators", *Sensors and Actuators A*, 72, pp. 88-97, 1999.

[17] P. Krause, E. Obermeier, and W. Wehl, "A micromachined single-chip inkjet printhead", *Sensors and Actuators A*, 53, pp. 405-409, 1996.

[18] J.-D. Lee, J.-B. Yoon, J.-K. Kim, H.-J. Chung, C.-S. Lee, H.-D. Lee, H.-J. Lee, C.-K. Kim, and C.-H. Han, "A thermal inkjet printhead with a monolithically fabricated nozzle plate and self-aligned ink feed hole", *Journal of Microelectromechanical Systems*, 8(3), pp. 229-236, 1999.

[19] M. Woytasik, J.-P. Grandchamp, E. Dufour-Gergam, J.-P. Gilles, S. Megherbi, E. Martincic, H. Mathias, and P. Crozat, "Two- and three-dimensional microcoil fabrication process for three-axis magnetic sensors on flexible substrates", *Sensors and Actuators A*, 132, pp. 2-7, 2006.

[20] K.L. Scott, T. Hirano, H. Yang, H. Singh, R.T. Howe, and A.M. Niknejad, "High- performance inductors using capillary based fluidic self-assembly", *Journal of Microelectromechanical Systems*, 13, pp. 300-309, 2004.

[21] C.H. Ahn, Y.J. Kim, and M.G. Allen, "A planar variable reluctance magnetic micromotor with fully integrated stator and coils", *Journal of Microelectro-mechanical Systems*, 2, pp. 165-173, 1993.

[22] C. Liu, T. Tsao, G.-B. Lee, J.T.S. Leu, Y.W. Yi, Y.-C. Tai, and C.-M. Ho, "Out-of-plane magnetic actuators with electroplated permalloy for fluid dynamics control", *Sensors and Actuators A*, 78, pp. 190-197, 1999.

[23] H. Miyajima, N. Asaoka, M. Arima, Y. Minamoto, K. Murakami, K. Tokuda, and K. Matsumoto, "A durable, shock-resistant electromagnetic optical scanner with polyimide- based hinges", *Journal of Microelectromechanical Systems*, 10, pp. 418-424, 2001.

[24] J.J. Bernstein, W.P. Taylor, J.D. Brazzle, C.J. Corcoran, G. Kirkos, J.E. Odhner, A. Pareek, M. Waelti, and M. Zai, "Electromagnetically actuated mirror arrays for use in 3-D optical switching applications", *Journal of Microelectromechanical Systems*, 13, pp. 526-535, 2004.

[25] M. Ruan, J. Shen, and C.B. Wheeler, "Latching micromagnetic relays", *Journal of Microelectromechanical Systems*, 10, pp. 511-517, 2001.

[26] P.E. Tenzer and R.B. Mrad, "A systematic procedure for the design of piezo-electric inchworm precision positioners", *IEEE/ASME Transactions on Mechatronics*, 9, pp. 427-435, 2004.

[27] J.A. Palmer, B. Dessent, J.F. Muling, T. Usher, E. Grant, J.W. Eischen, A.I. Kingon, and P.D. Franzon, " The design and characterization of a novel piezoelectric transducer-based linear motor", *IEEE/ASME Transactions on Mechatronics*, 9, pp. 392-398, 2004.

[28] P. Muralt, M. Kohli, T. Maeder, A. Kholkin, K. Brooks, N. Setter, and R. Luthier, "Fabrication and characterization of PZT thin-film vibrators for micromotors", *Sensors and Actuators A*, 48, pp. 157-165, 1995.

[29] T. Morita, M. Kurosawa, and T. Higuchi, "An ultrasonic micromotor using a bending cylindrical transducer based on PZT thin film", *Sensors and Actuators A*, 50, pp. 75-80, 1995.

[30] P. Muralt, "Ferroelectric thin films for micro-sensors and actuators: a review", *Journal of Micromechanics and Microengineering*, 10, pp. 136-146, 2000.

[31] R.W. Hertzberg, *Deformation and fracture mechanics for engineering materials*, 4th ed. Wiley, New York, 1995.